

Université du Québec
Institut National de la Recherche Scientifique
Énergie Matériaux Télécommunications

A CMOS COMPATIBLE
FERROELECTRIC TUNNEL JUNCTION MEMORY DEVICE

par

Fabian Ambriz Vargas

Thèse présentée pour l'obtention du grade de
Philosophiae Doctor (Ph.D.)
en Sciences de l'énergie et des matériaux

Jury d'évaluation

Président du jury	Professeur Shuhui Sun, INRS - EMT, Canada
Examinatrice externe	Professeure Clara Santato, École Polytechnique de Montréal, Canada
Examinateur externe	Professeur Ashish Garg, Indian Institute of Technology Kanpur, India
Co-directeur de recherche	Professeur Marc André Gauthier, INRS – EMT, Canada
Directeur de recherche	Professeur Andreas Peter Ruediger, INRS – EMT, Canada

July 2018

Acknowledgements

In first instance, I would like to acknowledge Professor Andreas Ruediger and Professor Marc André Gauthier for gave me the opportunity to come to Canada and develop my Ph.D. project. Also, I acknowledge the time, that both of you invested in reviewing, discussing and guiding me during the last few years. Through the development of this project, I felt working at the frontiers of the semiconductor memory field; therefore, I would like to acknowledge both of you for empowering the students. Thanks for make us believe that our projects can create an impact on the scientific community.

I acknowledge the examiners, Professor Shuhui Sun, Professor Clara Santato and Professor Ashish Garg, for accepting to review and evaluate this work.

I want to acknowledge all the members (students and postdoctoral fellows) of the *Nanophotonics* and *Gauthier* groups. Specially, Julien Plathier and Thameur Hajlaoui for help me with the redaction and revision of the french section. Also, I would like to acknowledge professor Reji Thomas for guided me during the first half of my Ph.D. project as well as offered me his valuable friendship.

The film deposition process was assisted with the help of the employers of *Plasmionique inc.* Therefore, I acknowledge Dr. Sarkissian and Dr. Rafik Nouar for gave me their advisory. Also, I acknowledge Dr. Andranik Sarkissian for reviewed my manuscripts, and for invited me to several conferences related to physical vapor deposition techniques.

I want to acknowledge both agencies *Fonds de recherche du Québec - Nature et Technologies* (FRQNT-Canada) and *Consejo Nacional de Ciencia y Tecnología* (CONACyT-Mexico) for provided me the financial support.

Finally, I acknowledge my family (Mother, father, sisters and brother) for gave their support, love and patience. I want to acknowledge the driving force of my life; my beloved wife (Josefina Crespo Villegas), the righteousness person I have ever met and also, I acknowledge my daughter (Nina Pastelita). Both wife and daughter are my spiritual masters in this game called life. *With special dedication to my sweet angels; Maria Britany, Gatito Caballerito Muffin and Luna Margarita.*

Abstract

The semiconductor electronic industry has been searching for a universal memory that combines fast write/read access with non-volatility and excellent scalability. To realize such an ambitious task, the following is required: Non-volatility like FLASH memory, scalability to high density like dynamic random access memory (DRAM) and FLASH, high speed like static random access memory (SRAM) and high endurance like DRAM and SRAM. To date, none of the commercially available solutions responds to all of those requirements.

Among the different emerging semiconductor memories, ferroelectric tunnel junctions (FTJs) are the most promising candidates to become a universal memory. An FTJ device is a resistance-based memory that combines good scalability (simple cell size: 1 capacitor-1transistor) with low operating energy, non-volatility, high operation speed (write time, <10 ns) and high endurance (> 10^6 cycles).

In 2009, the fabrication of the first FTJ memory device based on a perovskite tunnel barrier (BaTiO_3) was reported. However, the integration of perovskite materials into the conventional silicon technology remains challenging due to their lack of compatibility with the complementary metal oxide semiconductor process (CMOS). In this context, the present thesis reports on; the fabrication and evaluation of the first FTJ memory device based on CMOS-compatible materials and deposition processes.

The deposition of ferroelectric ultrathin films with only a few unit cells thickness is a crucial challenge in the development of FTJ memory devices. As such, the effect of the layer thickness on the ferroelectric properties of BaTiO_3 was studied first. Chapter four presents a detailed study of the growth mechanism of BaTiO_3 on $\text{Nb}:\text{SrTiO}_3$ substrates for on-axis RF-magnetron sputtering. The optimization of the deposition parameters to prevent substrate re-sputtering in order to allow the transfer of the correct stoichiometry from the target to the $\text{Nb}:\text{SrTiO}_3$ substrate surface is reported.

In most cases, literature reports the use of atomic layer deposition (ALD) and pulsed laser deposition (PLD) to grow ultrathin BaTiO_3 films. In the case of ALD, the deposition process of BaTiO_3 occurred in two steps: First, a non-crystalline BaTiO_3 film is deposited at a substrate

Abstract

temperature of 280°C while the second step consists in the annealing of the as-deposited film (at a relative high temperatures 900°C) to allow its crystallization. In the case of PLD, it achieves the deposition of crystalline BaTiO₃ in a single step, at a substrate temperature of 900°C. Although PLD is well suited for maintaining the stoichiometry of crystalline BaTiO₃, this process is not scalable. On the other hand, sputtering is a widely used deposition technique for large-scale production. Thus, in this thesis, crystalline BaTiO₃ was deposited in a single step at a relative low substrate temperature (650°C). However, this substrate temperature is still too high to be compatible with the semiconductor industry process. Therefore, it was necessary to search for new material candidates.

The recent discovery of ferroelectricity in Si-doped HfO₂ and Hf_{0.5}Zr_{0.5}O₂ films has renewed the interest for realizing ferroelectric tunnel junction devices, since ZrO₂ and HfO₂ are familiar to the semiconductor industry. Thus, in chapter five, Hf_{0.5}Zr_{0.5}O₂ was evaluated as a possible candidate for an FTJ memory device. The fabrication of two types of FTJ memories (nominally symmetric-FTJ and asymmetric-FTJ) made of CMOS compatible materials (Hf_{0.5}Zr_{0.5}O₂ as ferroelectric tunnel barrier and TiN as an electrode) is reported. In both types of FTJ memories, the electronic charge transport across the semiconductor/ferroelectric interfaces was studied by current-voltage curves. X-ray photoelectron and UV-VIS spectroscopies established a quantitative model for the band diagram. The combination of experimental data obtained from conductive-atomic force microscopy with theoretical models described by Simmons (nominally symmetric-FTJs) and Brinkman (asymmetric-FTJs) attested to the presence of the “tunneling electroresistance effect (TER effect)” in both FTJ memory devices. Furthermore, an evaluation of our FTJ memory device was performed, demonstrating excellent semiconductor memory properties (good endurance, good data-retention, large TER ratio at low voltages combined with a reproducible deposition process).

KEYWORDS: Ferroelectric tunnel junction memory, Ferroelectrics; Thin films

The following chapters are based on and contain word-by-word excerpts of references [1-6]. My contribution to this work was critical regarding the conception of the experiments for both thin film deposition and characterization, the execution of the experiments, the data analysis and the participation in the scientific discussion as well as the redaction of the manuscripts.

Résumé

L'industrie des semi-conducteurs est à la recherche d'une mémoire universelle combinant la vitesse de lecture et d'écriture des mémoires statiques (SRAM – Static Random Access Memory) ; la non-volatilité des mémoires flash ; et la haute densité d'informations ainsi que l'endurance des mémoires statiques (DRAM – Dynamic Random Access Memory). À ce jour, aucune solution disponible commercialement remplis ces critères ambitieux.

Parmi les différentes solutions émergentes, les mémoires ferroélectriques à jonction tunnel (FTJ – Ferroelectric Tunnel Junction) sont les candidates les plus prometteuses au titre de mémoire universelle. La FTJ est une mémoire utilisant le changement de sa résistance électrique pour stocker l'information qui allie une grande vitesse d'opération (temps d'écriture : ~ 10 ns) avec une faible volatilité, une haute densité d'informations (1 bit est composé uniquement d'une capacité et d'un transistor) et une haute endurance (10^6 cycles) ; le tout ne nécessitant qu'une faible quantité d'énergie.

En 2009, la fabrication de la première mémoire ferroélectrique à jonction tunnel, basée sur une barrière tunnel composée d'un matériau de la famille des pérovskites, le titanate de baryum, a été annoncée. Cependant, intégrer les pérovskites dans les procédés conventionnels de la technologie du silicium reste un défi causé par la faible compatibilité des méthodes de croissance des pérovskites avec les procédés de fabrication des composants électroniques (CMOS – Complementary Metal-Oxide Semiconductor). Dans ce contexte, cette thèse présente la première fabrication et caractérisation d'un dispositif mémoire FTJ utilisant des matériaux compatibles avec le procédé CMOS.

La déposition de couches ferroélectrique ultramince est un défi majeur dans le développement des dispositifs mémoire FTJ. Ainsi, l'effet de l'épaisseur de la couche sur les propriétés du titanate de baryum, l'un des matériaux ferroélectriques les mieux connus, a été étudié en détail en premier lieu. Cette étude, présentée dans le chapitre 4, explore le mécanisme de croissance du titanate de baryum (BaTiO_3) sur un substrat de titanate de strontium dopé avec du niobium ($\text{Nb}:\text{SrTiO}_3$).

Abstract

Le titanate de baryum comme barrière ferroélectrique ultramince a déjà été utilisé dans d'autres dispositifs mémoire FTJ. Dans la plupart des cas, les méthodes utilisées pour la croissance du titanate de baryum sont le dépôt atomique de couches (ALD – Atomic layer deposition) et l'ablation par laser pulsée (PLD – Pulsed laser deposition). Dans le cas de l'ALD, le dépôt s'effectue en deux étapes. D'abord, une couche amorphe de titanate de baryum est déposée sur le substrat chauffé à 280°C. Ensuite, un recuit de la couche permet la cristallisation. Dans le cas de la PLD, la déposition du titanate de baryum cristallin est effectuée en une seule étape en chauffant le substrat à 900°C. Bien que la PLD permette d'obtenir titanate de baryum cristallin avec la même stoechiométrie que la cible de déposition, ce procédé ne peut pas être utilisé à l'échelle industrielle. Cependant, le dépôt par pulvérisation cathodique est une méthode répandue pour la production à grande échelle. Par conséquent, dans cette thèse le titanate de baryum cristallin est déposé en une étape avec un substrat à une température relativement faible (650°C) en utilisant le dépôt par pulvérisation cathodique magnétron. Néanmoins, cette température reste trop élevée pour les procédés de l'industrie des semi-conducteurs. Il a donc été nécessaire de chercher d'autres matériaux ferroélectrique et compatible avec procédés industriels.

La découverte récente de la ferroélectricité dans les couches minces d'oxyde d'hafnium (HfO_2) et d'oxyde d'hafnium-zirconium ($\text{Hf}_{0.5}\text{Zr}_{0.5}\text{O}_2$) a renouvelé l'intérêt dans la réalisation de dispositifs mémoire FTJ puisque cette famille de matériaux est déjà utilisée par l'industrie du silicium. Ainsi, l'oxyde d'hafnium-zirconium est étudié dans le chapitre 5 comme candidat possible pour les dispositifs mémoire FTJ. Deux types de dispositifs (le FTJ-symétrique et le FTJ-asymétrique), compatibles avec la technologie CMOS ont été fabriqués en utilisant l'oxyde d'hafnium-zirconium comme barrière tunnel ferroélectrique et le nitre de titane (TiN) comme électrodes. Pour chaque dispositif, le transport des charges à travers les interfaces ferroélectrique/semi-conducteur sont étudiées en utilisant la spectrométrie de photoélectrons induits par rayons X (XPS – X-ray photoelectron spectrometry) et spectroscopie UV-Visible. La combinaison des données expérimentales, obtenue par microscopie à force atomique en mode conduction de courant (C-AFM – Conductive-Atomic Force Microscopy), et des modèles théoriques décrits par Simmons (FTJ-symétrique) et par Brinkman (FTJ-asymétrique) démontre la présence d'électrorésistance à effet tunnel (TER – Tunneling ElectroResistance) dans les deux types de dispositifs mémoire FTJ. De plus, la caractérisation de nos dispositifs démontre

Abstract

d'excellentes propriétés de mémoire semi-conductrice (bonne endurance et rétention de l'information, grand ratio TER à faibles tensions et un procédé de fabrication reproductible).

MOTS-CLÉS : Mémoires ferroélectriques à jonction tunnel; matériaux ferroélectriques; couches minces

Les prochains chapitres sont basés et contiennent des extraits des références [1-6]. J'ai apporté une contribution majeure à ces travaux en ce qui concerne la conception et la réalisation des expériences de synthèse et de caractérisation, l'analyse de données, la discussion des résultats, et la rédaction des manuscrits.

Publications, presentations and awards

PUBLISHED REFEREEED ARTICLES

- [1] G. Kolhatkar, **F. Ambriz-Vargas**, B. Huber, R. Thomas and A. Ruediger; Thermionic Emission Based Resistive Memory with Ultra-Thin Ferroelectric $\text{BiFe}_{(1-x)}\text{Cr}_x\text{O}_3$ Films Deposited by Mineralizer-Free Microwave-Assisted Hydrothermal Synthesis; *ACS-Crystal Growth & Design*; 10.1021/acs.cgd.7b01745 (2018).
- [2] **F. Ambriz-Vargas**, G. Kolhatkar, M. Broyer, A. Hadj-Youssef, R. Nouar, A. Sarkissian, R. Thomas, C. Gomez-Yáñez, M. A. Gauthier and A. Ruediger; A Complementary Metal Oxide Semiconductor Process-Compatible Ferroelectric Tunnel Junction; *ACS Applied Materials & Interfaces*, 9 (15), 13262–13268 (2017).
- [3] **F. Ambriz-Vargas**, G. Kolhatkar, R. Thomas, R. Nouar, A. Sarkissian, C. Gomez-Yáñez, M. A. Gauthier, and A. Ruediger; Tunneling Electroresistance Effect in a Pt/Hf_{0.5}Zr_{0.5}O₂/Pt Structure; *Applied Physics Letters*, 110, 093106 (2017).
- [4] **F. Ambriz-Vargas**, R. Nouar, G. Kolhatkar, A. Sarkissian, R. Thomas, C. Gomez-Yáñez, M. A. Gauthier, A. Ruediger; RF-magnetron Sputtering Deposition of Ultra-thin Hf_{0.5}Zr_{0.5}O₂ Films for Non-volatile Memory Applications; *Materials today: Proceedings*; 4 (7), 7000-7010 (2017).
- [5] **F. Ambriz-Vargas**, R. Zamorano-Ulloa, A. Romero-Serrano, J. Ortiz-Landeros, J. Crespo-Villegas, D. Ramírez-Rosales and C. Gómez-Yáñez; Point-defect Chemistry on the Polarization Behavior of Niobium Doped Bismuth Titanate; *Journal of the Mexican Chemical Society*; 61, 317-325 (2017).
- [6] G. Kolhatkar, **F. Ambriz-Vargas**, R. Thomas and A. Ruediger; Microwave-assisted Hydrothermal Synthesis of $\text{BiFe}_x\text{Cr}_{1-x}\text{O}_3$ Ferroelectric Thin Films; *Crystal Growth & Design*, 17 (11), 5697-5703 (2017).
- [7] **F. Ambriz-Vargas**, I. Velasco-Davalos, R. Thomas and Andreas Ruediger; Nucleation and Growth of Ultrathin BaTiO₃ Films on Single Terminated Nb:SrTiO₃ (100) Substrates for Ferroelectric Tunnel Junction; *Journal of Vacuum Science & Technology B*, 34, 02M101 (2016).
- [8] I. Velasco-Davalos, **F. Ambriz-Vargas**, C. Gómez-Yáñez, R. Thomas and A. Ruediger; Polarization Reversal in BaTiO₃ Nanostructures Synthesized by Microwave-assisted Hydrothermal Method; *Journal of Alloys and Compounds*, 667, 268-274 (2016).
- [9] I. Velasco-Davalos, **F. Ambriz-Vargas**, G. Kolhatkar, R. Thomas and A. Ruediger; Synthesis of BiFeO₃ Thin Films on Single-terminated Nb:SrTiO₃ (111) Substrates by Intermittent Microwave Assisted Hydrothermal Method; *American Institute of Physics, Advances*, 6 (6), 10.1063 (2016).
-

Publications, presentations and awards

- [10] Y. Ayadi, L. Rahhal, B. Vilquin, C. Chevalier, **F. Ambriz-Vargas**, S. Ecoffey, A. Ruediger, A. Sarkissian, S. Monfray, J. Cloarec, D. Drouin and A. Souifi; Novel Concept of Gas Sensitivity Characterization of Materials Suited for Implementation in FET-Based Gas Sensors; *Nanoscale Research Letters*, 11(481), 1-7 (2016).
- [11] **F. Ambriz-Vargas**, R. Nouar, Z. Said Bacara, B. Higuera, R. Porter, A. Sarkissian, R. Thomas and A. Ruediger; On-axis radio Frequency Magnetron Sputtering of Stoichiometric BaTiO₃ Target: Localized Re-sputtering and Substrate Etching During Thin Film Growth; *Thin Solid Films*, 596, 77-82 (2015).
- [12] I. Velasco-Davalos, **F. Ambriz-Vargas**, R. Thomas, A. Ruediger; Surface Preparation of (110) Oriented Pure and Nb Doped SrTiO₃ Single Crystal Substrates by Microwave Assisted Hydrothermal Method; *Surface & Coatings Technology*, 283, 108-114 (2015).

PUBLISHED BOOK CHAPTERS

- [13] **F. Ambriz-Vargas**, R. Thomas and A. Ruediger; Ferroelectric (Hf,Zr)O₂ Thin Films for High Density Non-volatile Memories?; *Frontiers in Materials Processing, Applications, Research and Technology: FiMPART 2015*; ISBN 978-981-10-4819-7 (2018).

PATENTS

Title: Ferroelectric tunnel junction and a method of fabrication thereof. Patent location: United States of America and Canada

Patent reference number: US 2018 773/14448.113

Inventors: **Fabian Ambriz-Vargas**, Gitanjali Kolhatkar, Thomas Reji, Rafik Nouar, Azza Hadj Youssef, Andranik Sarkissian, Marc A. Gauthier, Andreas Ruediger

CONFERENCE CONTRIBUTIONS

- [1] **Fabian Ambriz-Vargas**, Gitanjali Kolhatkar, Rafik Nouar, Andranik Sarkissian, Marc A. Gauthier and Andreas Ruediger; *Fabrication of a CMOS Compatible, Ferroelectric Tunnel Junction Memory*; **International Conference on Metallurgical Coatings and Thin Films**; California-United stated of America (2018, oral presentation).
- [2] **Fabian Ambriz-Vargas**, Gitanjali Kolhatkar, Thomas Reji, Rafik Nouar, Andranik Sarkissian, Marc A. Gauthier and Andreas Ruediger; *A CMOS Compatible, Ferroelectric Tunnel Junction Memory*; **23rd International Symposium on Plasma Chemistry**; Montreal-Canada (2017, poster presentation).
- [3] **Fabian Ambriz-Vargas**, Gitanjali Kolhatkar, Thomas Reji, Rafik Nouar, Andranik Sarkissian, Marc A. Gauthier and Andreas Ruediger; *A CMOS compatible, Ferroelectric Tunnel Junction*
-

Memory; Functional Coating and Surface Engineering symposium; Montreal-Canada (**2017**, poster presentation).

[4] Fabian Ambriz-Vargas, Gitanjali Kolhatkar, Thomas Reji, Rafik Nouar, Andranik Sarkissian, Marc A. Gauthier and Andreas Ruediger; *A CMOS Compatible, Ferroelectric Tunnel Junction Memory; Surface Canada 2017*; Montreal-Canada (**2017**, poster presentation).

[5] Fabian Ambriz-Vargas, Gitanjali Kolhatkar, Thomas Reji, Rafik Nouar, Andranik Sarkissian, Marc A. Gauthier and Andreas Ruediger; *A CMOS Compatible, Ferroelectric Tunnel Junction Memory; Colloque Plasma-Québec 2017*; Montreal-Canada (**2017**, poster presentations).

[6] Fabian Ambriz-Vargas, Marc A. Gauthier, Rafik Nouar, Andranik Sarkissian and Andreas Ruediger. *Resistive Switching in Pt/Hf_{0.5}Zr_{0.5}O₂/Pt and TiN/ Hf_{0.5}Zr_{0.5}O₂/TiN Structures.* **14th International Conference on Nanosciences & Nanotechnologies**; Thessaloniki-Greece (**2016**, oral presentation).

[7] Fabian Ambriz-Vargas, Gitanjali Kolhatkar, Thomas Reji, Rafik Nouar, Andranik Sarkissian, Marc A. Gauthier and Andreas Ruediger; *RF Magnetron Sputtering of Hf_{0.5}Zr_{0.5}O₂ Thin Films; Colloque Plasma-Québec 2016*; Montreal-Canada (**2016**, poster presentation).

[8] Fabian Ambriz-Vargas, Thomas Reji, Rafik Nouar, Andranik Sarkissian, Marc A. Gauthier and Andreas Ruediger. *RF Magnetron Deposition of Ultrathin BaTiO₃ Films;* **17th Canadian Semiconductor Science and Technology Conference**; Sherbrook-Canada (**2015**, oral presentation).

[9] Fabian Ambriz-Vargas, Gitanjali Kolhatkar, Thomas Reji, Rafik Nouar, Andranik Sarkissian, Marc A. Gauthier and Andreas Ruediger; *Ferroelectric Hf_{0.5}Zr_{0.5}O₂ Ultrathin Films; Colloque Plasma-Québec 2015*; Montreal-Canada (**2015**, poster presentation).

AWARDS

[1] – *Merit doctoral research scholarship program for foreign students (PBEEE)* du **Fonds de recherche du Québec Nature et technologies (FRQNT)** from January 2015 to May 2018.

[2] – *Ph.D. scholarship for international students* provided by the **National Council of Science and Technology of Mexico (CONACyT)** from September 2015 to December 2017.

Contents

Acknowledgements	i
Abstract.....	iii
Publications, presentations and awards.....	ix
Contents	xiii
CHAPTER 1 Introduction	1
1.1 Research objectives.....	4
1.2 Specific objectives	4
CHAPTER 2 State of the art.....	5
2.1 Semiconductor memories.....	5
2.2 Emerging semiconductor memories	7
2.3 Thin film growth process	12
2.4 Polarization properties	15
2.5 Solid solution hafnium zirconium oxide.....	18
2.6 Electronic charge transport at the semiconductor interface	22
2.7 Charge transport in metal-insulator-metal devices	24
CHAPTER 3 Characterization tools	29
3.1 Deposition techniques.....	29
3.2 Structural characterization tools	32
3.3 Chemical characterization tools.....	35
3.4 Microstructural characterization tools	37
CHAPTER 4 Ferroelectric tunnel junction based on BaTiO₃.....	39
4.1 Barium titanate thin film	39

Contents

4.2 Experimental section.....	40
4.3 Localized re-sputtering and substrate etching during thin film growth	43
4.3.1 Stoichiometry of as-deposited $BaTiO_3$ films	46
4.3.2 Summary	48
4.4. Fabrication of a $Nb:SrTiO_3/BaTiO_3/Pt$ -tip heterostructure.....	49
4.4.1 Growth mechanism of a $BaTiO_3$ on a $Nb:SrTiO_3$ substrate	50
4.4.2 Ferroelectricity of $BaTiO_3$ in ultrathin film form	52
4.4.3 Summary	53
CHAPTER 5 Ferroelectric tunnel junction based on $Hf_{0.5}Zr_{0.5}O_2$.....	55
5.1 Hafnium-Zirconium oxide film.....	55
5.2 Experimental section.....	56
5.3 Optimization of the $Hf_{0.5}Zr_{0.5}O_2$ deposition parameters	58
5.3.1 Microstructural characterization.....	58
5.3.2 Chemical characterization.....	58
5.3.3 Ferroelectricity as a function of deposition temperature	59
5.3.4 Ferroelectricity as a function of film thickness.....	61
5.3.5 Summary	63
5.4 Nominally symmetric FTJ memory device ($Pt/Hf_{0.5}Zr_{0.5}O_2/Pt$)	64
5.4.1 Fabrication of the nominally symmetric FTJ memory device	64
5.4.2 Ferroelectric characterization of the nominally symmetric FTJ device.....	65

Contents

<i>5.4.3 Electronic properties of the nominally symmetric FTJ memory device</i>	66
<i>5.4.4 Tunneling electroresistance effect in the nominally symmetric FTJ memory device ..</i>	69
<i>5.4.5 Summary</i>	71
5.5 Asymmetric FTJ memory device (TiN/Hf_{0.5}Zr_{0.5}O₂/Pt)	72
<i>5.5.1. Fabrication of the asymmetric FTJ memory device</i>	72
<i>5.5.2 Ferroelectric characterization of the asymmetric FTJ memory device</i>	74
<i>5.5.3 Electronic properties of the asymmetric FTJ memory device</i>	75
<i>5.5.4 Tunneling electroresistance effect on the asymmetric FTJ memory device</i>	78
<i>5.5.5 Evaluation of the asymmetric FTJ memory device</i>	80
<i>5.5.6 Summary</i>	81
Summary and outlook	83
Appendix A (Thickness measurements and XPS calibration)	87
Appendix B (Platinum structural properties)	89
Appendix C (Ferroelectric retention measurements)	90
Appendix D (Band alignment determination)	91
Appendix E (Simmons and Brinkman models)	94
References	97
Abbreviations	107
Résumé en Français	111

Chapter 1 Introduction

Recent technology improvements in micro- and nano- fabrication techniques have brought a new generation of electronic devices to the market, such as computers, cellphones, cameras, tablets, etc.⁷⁻⁹ In addition to being slimmer and lighter, these devices possess more storage capacity, they are faster, and also have an improved camera resolution. As predicted by “Moore’s law”, customers have been experiencing the birth of new generations of electronic devices every couple of years, during the last four decades. This trend has led the customers to continually expect more powerful and cheaper devices. However, that may not be the case if the electronic industry continues working with the current semiconductor memory technology.¹⁰

The key issue of current electronic devices is that they rely on the performance of a set of different semiconductor memories that have already reached their physical limits. In general, the processor within the central processing unit (CPU) of any personal computer is serviced by a series of memory technologies (Memory hierarchy in [Table 1](#)). The closest memory to the CPU is called “*Cache memory*” and it is comprised of a static random access memory (SRAM),⁷ it is very fast (write/erase time: 0.3 ns/ 0.3 ns) but it is relative large in cell size (six transistors with a minimum cell size of $140F^2$, where “ F ” is the minimum feature size). Given their physical properties, SRAMs are used to provide fast access to instructions and data to the processor.⁷ In the next level of the hierarchy appears the “*Principal memory*”, which is comprised of a dynamic random access memory (DRAM). Contrary to SRAM, it is more compact (one-transistor and one-capacitor, with a cell size of $6F^2$) but it is slower (write/erase time: 10ns/10ns).⁷ The physical properties of DRAM allow it to reach high densities on a memory chip. The “*Principal memory*” is used to store and to process temporary information from the “*Secondary memory*” (hard disk).⁷ In both cases, the “*Cache*” and the “*Principal*” memories are volatile (stored information will not remain when the energy power supply is turned off). “*Secondary memory (solid state hard drive)*” is mostly a flash memory, it is an external memory with non-volatile nature (it holds the information when the power supply is turned off). In comparison to the “*Primary and Cache memories*” it is really slow (write/erase time: 1ms/10ms).^{7, 10}

As can be seen, the dominant memory types in modern electronics are dynamic-RAM (DRAM), static-RAM (SRAM), and FLASH memories.^{8-9, 11-12} These three types of memories

store data as a charge state. For many decades these memory technologies have been successfully scaled down to achieve higher speeds and increased density of memory chips at lower cost. However, they have gradually approached their physical limits of scalability.^{8, 11, 13} Therefore, for further advance in information processing/storage technologies, it is necessary to develop a universal memory than can replace the above conventional memories. To accomplish with this goal the universal memory should combine the best features of the current memories. For instance, it should combine the non-volatile nature of FLASH with the high scalability of DRAM, high speed of SRAM and high endurance of DRAM and SRAM (Table 1).^{7, 12}

Table 1. Memory hierarchy and memory properties. Data obtained from ref. [7]

MEMORY HIERARCHY	MEMORY PROPERTIES				
	Processor (CPU)	Speed (Write/erase time)	Scalability (Cell size)	Endurance (Cycles)	Energy efficiency
Cache memory		✓ HIGH (0.3ns/0.3ns)	✗ LOW (140F ²)	✓ HIGH (10 ¹⁶)	✗ VOLATILE
Primary memory		✓ HIGH (10ns/10ns)	✓ HIGH (6F ²)	✓ HIGH (10 ¹⁶)	✗ VOLATILE
Secondary memory		✗ LOW (1ms/10ms)	✓ HIGH (10F ²)	✗ LOW (10 ⁵)	✓ NON-VOLATILE
Universal memory		✓ HIGH	✓ HIGH	✓ HIGH	✓ NON-VOLATILE

Nowadays, there are emerging semiconductor memories based on different physical approaches that could satisfy the positive points of DRAM, SRAM, and FLASH.^{7, 12} Among the different noticeable types of emerging memories, the strongest candidate to become a universal memory is the ferroelectric tunnel junction memory (FTJ).

An FTJ memory device is composed of two metal electrodes separated by a nanometer-thick ferroelectric layer (1-3 nm in thickness).¹⁴⁻¹⁶ The physical concept of this memory is based on the tunneling electroresistance effect, (TER effect). This process consists in the reversible modulation of the electrical resistance state by using an electric field.¹⁴⁻¹⁶ This modulation gives place to the formation of two stable states (High resistance state, “HRS” and low resistance state, “LRS”), which can be codified as “1” and “0” in a binary code.¹⁴⁻¹⁶

The first experimental demonstration of the TER effect was reported in 2009 by M. Bibes (*Nature Letters*)¹⁷ and A. Gruverman (*Nanoletters*).⁹ In both cases, BaTiO₃ was used as an ultrathin ferroelectric layer. These results triggered an intense research on the study of the properties of the FTJs, where it was demonstrated that the physical concept of the FTJ memory can bring important advantages such as high fatigue resistance (endurance ~ 10⁶ cycles),¹⁸⁻¹⁹ high speed (“ON/OFF” states can be written with pulses down to 10 ns),²⁰ high scalability,¹⁵ and simple architecture.¹⁴

Despite the excellent memory properties of FTJ devices, their introduction into the semiconductor market has been restricted because integrating FTJs based on ferroelectric perovskite ultrathin films (such as BaTiO₃, BiFeO₃ or PbTiO₃) into the conventional semiconductor memory technology remains challenging for many reasons. For example, perovskites present poor interfacing with silicon, an elevated crystallization temperature (700-900°C) and undergo electrical degradation caused by a forming gas treatment.²¹⁻²⁴

In 2016, A. Chernikova et al.²⁵ discovered the presence of robust ferroelectricity in ultrathin Hf_{0.5}Zr_{0.5}O₂ films (layer thickness ~2.5 nm). This was a surprise since hafnia (HfO₂) and zirconia (ZrO₂) are oxides that have been studied in bulk form for more than a century.²⁶ This result leads to consider that the ferroelectricity of Hf_{0.5}Zr_{0.5}O₂ has the potential to solve the CMOS incompatibility issues of the FTJs. As this solid solution results from the combination of ZrO₂ and HfO₂. Both materials are familiar to the semiconductor industry.²⁷⁻²⁸ Indeed, they are used as dielectric materials in the current commercial dynamic random access memory.^{26, 29} Thus, an FTJ memory based on Hf_{0.5}Zr_{0.5}O₂ could overcome the CMOS incompatibility issues.

In order to introduce the FTJ memory into the semiconductor market; it is necessary first, to investigate the electronic charge transport mechanism in this new memory device.¹⁴ Being more specific, a deep study on the relationship between the ferroelectric/metal interface properties and the electronic charge transport current needs to be performed, to better optimize the performance of an FTJ memory device. Therefore, an investigation of the metal/ferroelectric interfaces with UV-vis and X-ray photoelectron spectroscopies combined with theoretical models³⁰⁻³¹ can bring further insights.¹⁴

1.1 RESEARCH OBJECTIVES

The main goal of this thesis is to investigate the feasibility of a CMOS-compatible ferroelectric tunnel junction based on $\text{Hf}_{0.5}\text{Zr}_{0.5}\text{O}_2$.

1.2 SPECIFIC OBJECTIVES

To accomplish the above objective, this work is divided into three specific objectives:

1. Optimization of the radio-frequency magnetron sputtering deposition parameters for the growth of the bottom electrode (TiN), the ferroelectric ultrathin film ($\text{Hf}_{0.5}\text{Zr}_{0.5}\text{O}_2$) and the top electrode (Pt). This optimization includes thickness, stoichiometry, and crystallinity as a function of deposition temperature.
2. Experimental demonstration of the tunneling electroresistance effect (TER) including a detailed study of the ferroelectric/metal interface properties of an FTJ memory device.
3. Quantitative assessment of the FTJ memory properties: ON/OFF ratio, endurance, retention of the information and reproducibility.

Chapter 2 State of the art

This chapter begins with the classification and definition of the different types of semiconductor memories. Also, it describes the nucleation growth mechanisms of a thin film on the substrate surface. It is followed by a description of the ferroelectric tunnel barrier properties (polarization, ferroelectricity and piezoelectricity). The core of this Ph.D. thesis relies on the material used as a tunnel barrier, therefore one section of this chapter is dedicated to describe the chemical and physical properties of hafnium-zirconium oxide ($\text{Hf}_{0.5}\text{Zr}_{0.5}\text{O}_2$). At the end, this chapter presents an overview of the Ph. D. thesis work of L. Esaky, who describes in detail the tunneling current mechanism at the interface of an n-type/p-type semiconductor junction.

2.1 SEMICONDUCTOR MEMORIES

Semiconductor memories are a key component of any data processing system. Historically, the combination of fast volatile solid state semiconductor memories with compact nonvolatile hard disk drives has enabled the introduction of the personal computer.⁷ As shown in Figure 1, semiconductor memories can be classified into random access memories and read-only memories. In RAMs, the information can be written or read from any cells for multiple times, while in ROMs the read/write cycles are limited. RAMs are divided into volatile memories and nonvolatile memories. Dynamic RAM (DRAM) and static RAM (SRAM) are examples of volatile memories.¹²

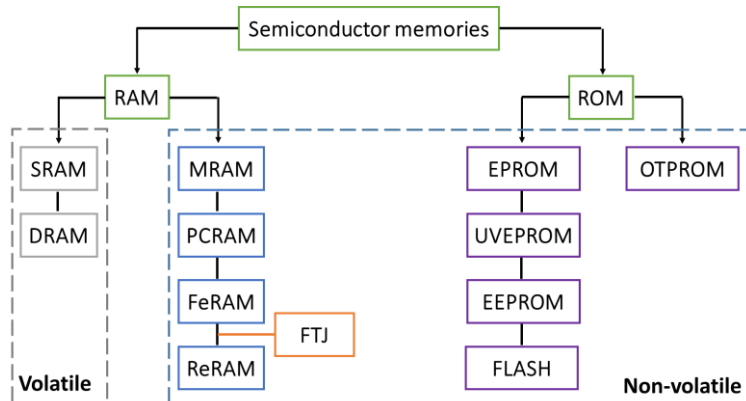


Figure 1. Semiconductor memories classification. Adapted from ref. [7]

ROMs are non-volatile memories, they are classified as one-time programmable ROM (OTPROM) and erasable programmable ROMs (EPROM). EPROM can be erased either by exposing the memory cell to ultraviolet radiation (UVEPROM) or by electrical means (EEPROM).¹²

Dynamic Random Access memory

DRAM has been the technology of choice for main memory systems for the past four decades. Nowadays, semiconductor memories represent approximately 21% of the total semiconductor market. Although a large variety of memory types is available, the market is dominated mainly by DRAM (which makes up 48% of the memory market), Figure 2.¹² The fundamental unit of storage in a DRAM system is a DRAM cell. It is composed of one capacitor and one transistor (1C1T). The data in a DRAM cell is represented as the amount of electrical charges stored in the capacitor. When the DRAM cell stays charged without any operation for a certain amount of time, the current leakage drains out the stored charges, leading to the loss of the data. To retain the information in the DRAM cell, the information has to be refreshed periodically, every 64ms.¹¹

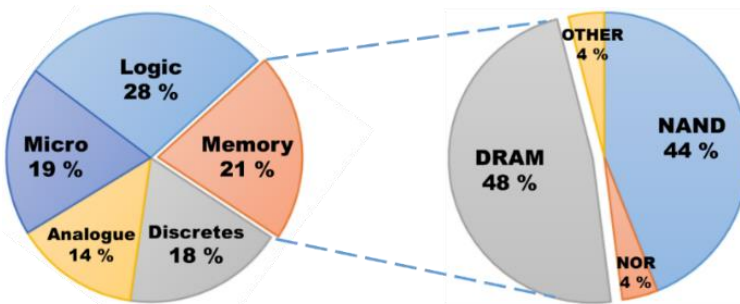


Figure 2. Semiconductor memory market. Adapted from ref. [12]

The memory system in combination with hard disk contribute as much as 40% of the overall power consumption. Therefore, energy efficiency becomes a critical aspect in electronic devices.⁷ Then, the replacement of DRAM and SRAM memories with non-volatile memory technology would considerably improves the energy efficiency.⁷

2.2 EMERGING SEMICONDUCTOR MEMORIES

There are many different noticeable types of memories, based on different physical concepts ([Figure 1](#)), such as ferroelectric RAM (FeRAM), resistive RAM (ReRAM), magnetic RAM (MRAM), phase-change RAM (PCRAM), molecular memories, DNA memories etc. Below is made a small description of the most common emerging memories.

Ferroelectric Random Access Memory (Fe-RAM)

The physical concept of this memory was introduced in the 1980's. It offers several advantages such as low-power consumption (non-volatile), fast read/write speed (10ns/10ns) and good cyclability (10^{14} cycles).^{7, 32-33} This memory is based on charge storage, its physical concept relies on sensing electrical charges. A Fe-RAM cell is composed of one ferroelectric capacitor and one transistor (1C-1T, cell size is 22F^2). The ferroelectric capacitor is made of a ferroelectric thin film (~100 nm thick) sandwiched between two electrodes. When the ferroelectric capacitor is subjected to a sufficiently strong electric field, polarization of the ferroelectric layer occurs. An ideal hysteretic *P-E* curve (*polarization vs electric field*) of a Fe-RAM cell has two distinguishable polarization states (negative and positive remnant polarization). These two stable states are the basis of Fe-RAMs. Nowadays, $\text{Pb}(\text{Zr}_x\text{Ti}_{1-x})\text{O}_3$ and $\text{SrBi}_2\text{Ta}_2\text{O}_9$ are used as ferroelectric layers in the current commercial capacitor of a Fe-RAM cell.^{7, 12, 34-35}

However, Fe-RAM faces some challenges such as destructive read-out (which makes it necessary to restore the information after the reading operation), a scaling limit as well as incompatibility with the back-end CMOS process, where the application of a forming gas annealing weakens the ferroelectric properties and introduces cross-contaminations at the ferroelectric/silicon interface.¹⁵

Phase-change Random Access Memory (PCRAM)

This type of memory exploits a reversible phase transition process of some materials such as chalcogenide glass. This materials modulate their phase (from amorphous to crystalline) upon the application of heat, which results in a change of either the electrical resistance or the optical reflectivity. Due to recent improvements in semiconductor manufacturing technology, the development of high-quality phase-change memories have become feasible. Given their promising semiconductor properties (moderate read/write speed: 20ns/50ns and good endurance: 10^8 cycles), they are available as commercial products. Indeed, they have been successfully employed as optical memories such as CDs and DVDs.^{7, 10, 13}

Magnetic Random Access Memory (MRAM)

MRAM is an electrical resistance based memory, it relies on the magnoteresistance effect. The magnetic memory cell is composed either of one or two transistors with one magnetic store element (1(2)T-1M, memory cell size $20F^2$). These elements are formed of an insulator layer placed between two ferromagnetic plates (one plate is a permanent magnet and the other can be magnetized). The orientation of the magnetic field of both ferromagnetic plates defines the ON and OFF states. Field-writing MRAMs were introduced almost three decades ago (1990's). Nowadays, they are used as a 16megabit MRAM. The primary issue with MRAMs is their high write current, which makes scaling difficult.^{7, 10}

Resistive Random Access memory (ReRAM)

This category includes all type of memories that use two or more distinct resistance states as the binary values “0” and “1”. A ReRAM is a non-charge storage based memory, its cell is composed of one transistor and one resistor (1T-1R, small cell size: $4F^2$). A ReRAM resistor consists of one insulating material sandwiched between two metal electrodes. The two stable electrical resistance states of this memory are modulated upon the application of an electric field. Both stable states can be used in a binary code.^{7, 15}

The change in the electrical resistance is originated either from an electrochemical metallization mechanism or due to a valence change mechanisms. The first mechanism creates conducting filaments inside of the insulating material. This filament behaves as a conducting bridge between the two metal electrodes which favors the low-electrical resistance state of the memory. By changing the direction of the polarization the conductive bridges can be broken leading to high resistance state of the memory. Valence change mechanism is characterized by the formation of a conductive bridge made of oxygen vacancies. The creation of this conductive filament inside of the insulating barrier is triggered by the migration of oxygen ions that results in the formation of localized oxygen vacancies. The conduction in the cell memory (low resistance state) is due to electron hopping between the oxygen vacancies.^{7, 36-38} A ReRAM combines excellent memory properties such as fast read/write access (5ns/5ns) with good endurance (10^{10} cycles).⁷

Ferroelectric Tunnel Junction memory (FTJ)

FTJ memory is a resistance based memory. It is composed of one ferroelectric ultrathin layer sandwiched by two metal electrodes (Metal-Ferroelectric-Metal).³⁹ FTJ memories rely on the tunneling electroresistance effect (TER effect)⁴⁰ which induces an electrical resistive switching. This in turn gives place to the presence of two distinct electrical resistance states (high- and low- resistance state).¹⁴ At the beginning, it was believed that the origin of the TER effect in an FTJ memory was attributed to a mechanisms related to “*Piezoelectric effects*”, where the application of an electric field produces strain on the ferroelectric barrier and therefore changes in the barrier width which modifies the electrical charge transport. However, FTJ memory devices are designed to operate at low voltages in order to avoid the desestabilization of the ferroelectric state; then the piezoelectric effects are clamped in ultrathin films. Recent studies on the effect of the ferroelectric polarization over the transport properties of an ultrathin ferroelectric layer sandwiched between two conductive electrodes suggests that the main mechanisms that causes the TER effect in an FTJ are related to: “*Microscopic interfacial effects*”, where the reversal of a ferroelectric polarization changes the position of the ions near the interfaces (metal/ferroelectric), affecting the chemical bonding between the atoms, leading to a change in electronic charge transport and/or “*depolarizing-field effects*”, where the reversal of the ferroelectric tunnel barrier induces changes in the barrier height of an electrostatic potential profile which results in a change of the electrical transport properties.

The tunneling current density in an FTJ depends exponentially on the thickness of the ultrathin ferroelectric barrier. Basically, the ferroelectric dipole orientation codes for high or low resistance state in the FTJ memory device.¹⁴ The difference between the high and low resistance state is known as the TER ratio. Its value is usually in the range of 10 to 100.⁴¹⁻⁴³ However, a giant TER ratio had been demonstrated in FTJ memories based on BiFeO₃,¹⁹ PbTiO₃⁴⁴ and BaTiO₃.¹⁷ A crucial condition to fabricate FTJ memory devices is to achieve ferroelectricity in ultrathin film form.¹⁵⁻¹⁶ Non-centrosymmetric perovskite materials in their thin film form such as BaTiO₃,^{5, 45-46} BiFeO₃⁴⁷⁻⁴⁸ and PbTiO₃⁴⁴ are well known for their outstanding ferroelectric properties. However, their ferroelectricity starts to disappear as their layer thickness decreases.¹⁵⁻¹⁶ For many years, it was believed that ferroelectricity exists only in films with a film thickness above a certain critical

thickness (around 10 nm).⁴⁹ Recently, strain engineering studies had proved that the ferroelectricity is compatible with ultrathin films.⁴⁹ This is possible, due to the strain forces generated between the film and substrate which distort the crystal structure lattice of the ultrathin film.⁴⁹ This in turn reduces the symmetry of the crystal structure, which enhances the ferroelectricity in the ultrathin films. In 2009, Vincent Garcia et. al.¹⁷ made the experimental demonstration of robust ferroelectricity in a 1-nm thick highly strained BaTiO₃ film. This discovery allowed the experimental demonstration of the tunneling electroresistance effect in a metal-ferroelectric-semiconductor structure. Up to know, perovskite materials such as BaTiO₃,^{17, 43} PbTiO₃,⁴⁴ BiFeO₃¹⁹ and Pb(Zr,Ti)O₃³¹ have been successfully used as ultrathin ferroelectric barriers in FTJ devices (Table 2).

Table 2. Survey of reported FTJs

Bottom (BE) and top (TE) electrode	Ferroelectric barrier	Deposition technique	Main remarks	Ref.
BE=La _{0.67} Sr _{0.33} MnO ₃ , TE= Cr/Pt	BaTiO ₃ (t _F =1nm) T _S = 775°C	PLD	Ferroelectricity in 1 nm highly strain BaTiO ₃	[17] 2009
BE= Nb:SrTiO ₃ BE= Au/ti	BaTiO ₃ (t _F =10u.c.) T _S = 775°C	PLD	TER effect demonstration	[43] 2009
BE=SrRuO ₃ TE=conductive tip	PbTiO ₃ (t _F =3.6nm) T _S = 700°C	PLD	Giant TER effect FE of Retention of 72 h	[44] 2010
BE=La _{0.67} Sr _{0.33} MnO ₃ TE=Co/Au	BaTiO ₃ (t _F =2nm) T _S = 700°C	PLD	TER ratio= 64 ON/OFF cycles=900	[20] 2012
BE=Au/Co, TE=La _{0.67} Sr _{0.33} MnO ₃	PZT* (t _F =1.6nm) T _S = 700°C	PLD	TER ratio= 300 at ±0.4V Brinkman model	[31] 2012
BE=Ca _{0.96} Ce _{0.04} MnO ₃ TE= Co	BiFeO ₃ , (t _F =4.6nm)	PLD	TER ratio = 10 ³ , ON/OFF cycles=10 ⁶	[18] 2014
BE=Ca _{0.96} Ce _{0.04} MnO ₃ TE= Co/Pt	BiFeO ₃ , (t _F =7u.c.) T _S = 750°C	PLD	TER ratio = 10 ⁴ , Retention= 68 h, ON/OFF cycles=10 ³	[19] 2013
BE=La _{0.67} Sr _{0.33} MnO ₃ , TE= Graphene	BaTiO ₃ , (t _F =6u.c.) T _S = 680°C	PLD	TER ratio= 6000 at ±0.2V	[50] 2014
BE=La _{0.67} Sr _{0.33} MnO ₃ TE= Cu	BaTiO ₃ , (t _F =3nm) T _S = 700°C	PLD	TER ratio of 1000 Brinkman model	[51] 2014

u.c.: Unit cell, PLD: Pulsed laser deposition, ALD: Atomic Layer deposition, TER: tunnelling electroresistance, *PZT: PbZr_{0.2}Ti_{0.8}O₃, T_F= Film thickness, FE=Ferroelectric and T_S= Substrate temperature

The top and bottom electrodes in an FTJ device also play an important role⁵² because in principle, they define the quality of the ultrathin film morphology, ferroelectric behavior of the tunnel barrier, TER ratio, and the electrical charge transport at the metal/ferroelectric interface.^{16, 30} In order to obtain a large TER ratio, the use of semiconductor materials as bottom electrodes is required. This is, because they allow to barrier width to experience modulation to a greater extent by realizing a depletion region in the semiconductor near the ferroelectric/semiconductor interface. Also, it is required that the structural properties (crystal structure and cell size) of the bottom electrodes should be similar to the structural properties of the ultrathin film. When the ferroelectric layer of an FTJ is made of an oxide layer such as $\text{Hf}_{0.5}\text{Zr}_{0.5}\text{O}_2$ the size of the TER ratio will be affected by the grade of crystallization of the film, when a large percentage of the grains that composed this oxide layer will results in a large TER ratio. Inversely, an oxide film composed mostly of non-crystalline grains will lead to issues in the TER ratio.⁵³ As shown in [Table 2](#), semiconductors such as $\text{La}_{0.67}\text{Sr}_{0.33}\text{MnO}_3$ (3.871 Å),¹⁷ SrRuO_3 (3.905 Å)⁴⁴ and $\text{Ca}_{0.96}\text{Ce}_{0.04}\text{MnO}_3$ (3.946 Å)¹⁸ are used as bottom electrodes in FTJ devices based on BaTiO_3 (3.992 Å).

Recently, it was believed that in order to obtain coherent-direct tunneling current across the ferroelectric layer it was mandatory to use electrodes made of different materials.⁴² As they create an electrostatic potential barrier profile with a trapezoidal shape. This kind of shape allows coherent-direct tunneling current in FTJ devices.³⁰ On the other hand, there should not be coherent-direct tunneling in an FTJ device which has same material in the top and bottom electrode. However this is not entirely true, as experimental evidence have shown that that the symmetry in an electrostatic potential profile can be broken. This loss in symmetric can come due to different reasons such as presence of different interface terminations, pinned interface dipoles or due to the formation of an ultrathin dielectric layer at one of the interfaces.¹⁴

2.3 THIN FILM GROWTH PROCESS

In the deposition process there are four steps involved: i) Production of the appropriate atomic, molecular or ionic species; ii) transport of these species from the source to the substrate; iii) condensation of the species on the substrate surface; and iv) nucleation, in which the adsorbed species interact among themselves to form clusters or nuclei. Once these nuclei reach a certain critical size, the clusters become thermodynamically stable.⁵⁴ The growth process consists of a statistical process of nucleation, surface-diffusion, controlled growth of the three dimensional nuclei and its subsequent filling to give a continuous film.⁵⁵ Depending on the thermodynamic parameters of the deposit and substrate surface, the initial nucleation and growth stage can be described with three different growth modes:

i) **Volmer-Weber or island growth** occurs when stable clusters nucleate on the substrate surface and grow into three-dimensional island features (Figure 3). In this growth mode, the bonds of the atoms or molecules to be deposited are stronger between them than to the substrate material. Volmer-Weber growth mode is usually presented when the structural properties and the chemical composition of the substrate and the film are different.^{54,55}

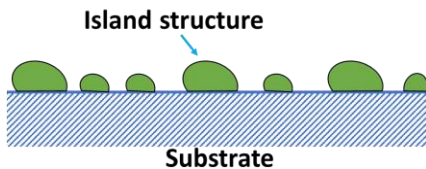


Figure 3. Volmer-Weber (island) growth. Adapted from ref. [55]

ii) **Frank-Van der Merwe or “layer by layer”** occurs when the atoms or molecules deposited have the tendency to expand into two dimensions, which results in the formation of planar layers (Figure 4). This growth mode is characterized by a weak bonding forces between the deposited species (either molecules or atoms) and the strong bonding force between substrate atoms. An example of this growth mode is the epitaxial growth of semiconductors.^{54,55}

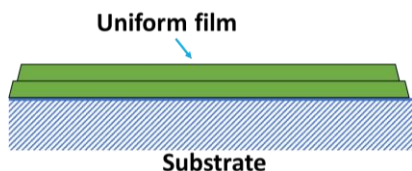


Figure 4. Frank-van der Merwe (layer-by-layer) growth. Adapted from ref. [55]

iii) **Stranski-Krastanov mode** is a combination of the layer-by-layer and island growth modes. This mechanism occurs in two steps. First is the formation of one or more monolayers in a layer-by-layer mode, and the subsequently formation of islands on the top of the monolayers (Figure 5).^{5,55}

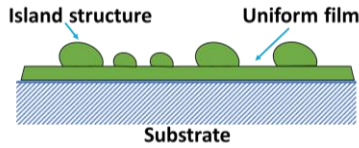


Figure 5. Stranski-Krastanov growth. Adapted from ref. [55]

There are thermodynamic models for nucleation and growth of thin films which describe the surface energies between the substrate and the film. One model that describes the process of atomic nucleation of a film on the substrate during vapor deposition is presented in Figure 6. In this model, the mechanical equilibrium between the components of interfacial tension and constitutive phases is described by Young's equation.⁵⁴⁻⁵⁵ It is used to understand better the three types of growth modes

$$\gamma_{sv} = \gamma_{fs} + \gamma_{fv} \cos\theta \quad (1)$$

Where γ is the interfacial energy while s , f and v stand for substrate, film and vapor, respectively and the contact angle (wetting angle) is represented by θ .⁵⁴⁻⁵⁵

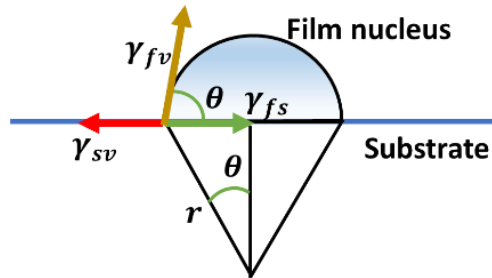


Figure 6. Atomistic nucleation process during the film growth. Adapted from ref. [55]

Island growth mode occurs when the wetting angle is much higher than zero ($\theta > 90^\circ$), in this growth mode the surface tension of the film exceeds the surface tension of the substrate. As the wetting angle gets closer to zero ($\theta \sim 0$) a layer by layer growth mode occurs. This type of growth mode is characterized for present small difference in surface energy between the film and

the substrate, in this conditions the film wets the substrate surface. In the case of the Stranski-Krastanov growth, first the wetting angle is close to zero ($\theta \sim 0$) which leads to a layer-by-layer growth mode and after the island growth mode ($\theta > 0$) occurs.⁵⁴⁻⁵⁵

There are two types of epitaxial growth. The first is known as homoepitaxy, it occurs when the material of the film to be deposited is the same as the material of the substrate (e.i. silicon film on a silicon substrate, [Figure 7 \(a\)](#)). The second epitaxial growth mode is known as heteroepitaxy, which occurs when the materials of the film and substrate are different. When the lattice parameters are slightly mismatched, strain-layer epitaxy growth mode occurs ([Figure 7 \(b\)](#)). The existence of large lattice mismatch between film/substrate (the crystal structure of the film and substrate are different) leads to the relaxation of the film material to its bulk structure through the formation of lineal defects such as dislocations ([Figure 7 \(c\)](#)).⁵⁴⁻⁵⁵

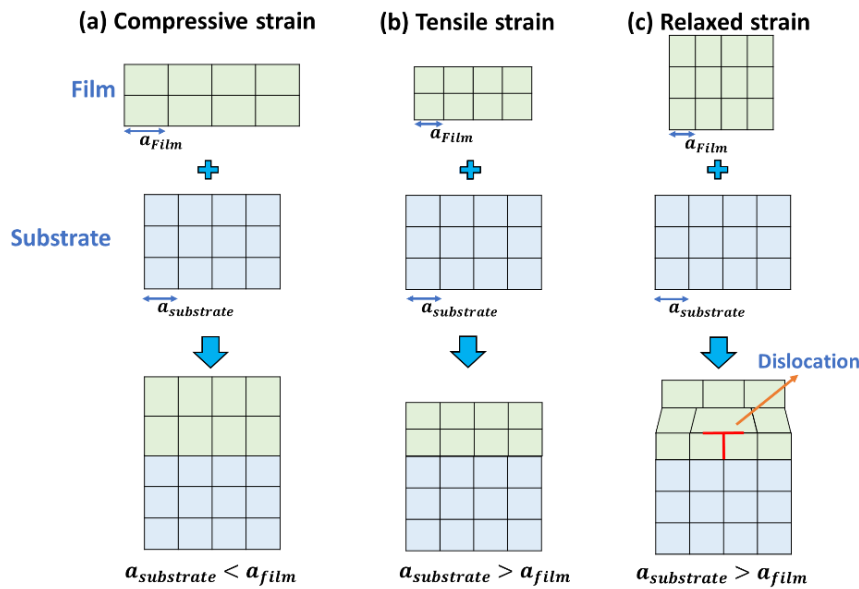


Figure 7. Schematic representation of (a) a nearly lattice matched, (b) a strained and (c) a relaxed heteroepitaxial film growth. from ref. [54]

2.4 POLARIZATION PROPERTIES

A dielectric material is essentially an electrical insulator. However, under the application of an electric field the electrical charges shift from their equilibrium position resulting in a dielectric polarization (Figure 8).

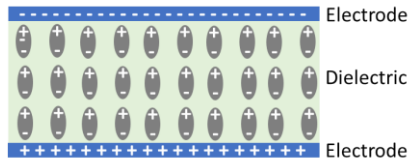


Figure 8. Polarization of a dielectric crystal.

Among the different dielectric materials, non-linear dielectrics possess special properties such as: piezoelectricity, pyroelectricity and ferroelectricity. Based on the lattice structure and crystal symmetry they can be classified into 32 crystal classes (Figure 9). The application of mechanical stresses on a piezoelectric crystal leads to changes in crystal shape and in the centers of gravity of the charges (electrical polarization of the crystal). Piezoelectricity only appears in crystals that lack a center of symmetry. Among the different crystal classes only twenty-one correspond to the non-centrosymmetric group, where just one of them cannot produce a dipole moment (cubic class 432). From the twenty remaining classes only ten are pyroelectric. This type of crystals are characterized for present spontaneous polarization when they are exposed to a certain temperature. Finally, among this ten crystal classes only a small fraction are ferroelectric. In this case, the spontaneous polarization occurs when the crystal is exposed to an electric field.

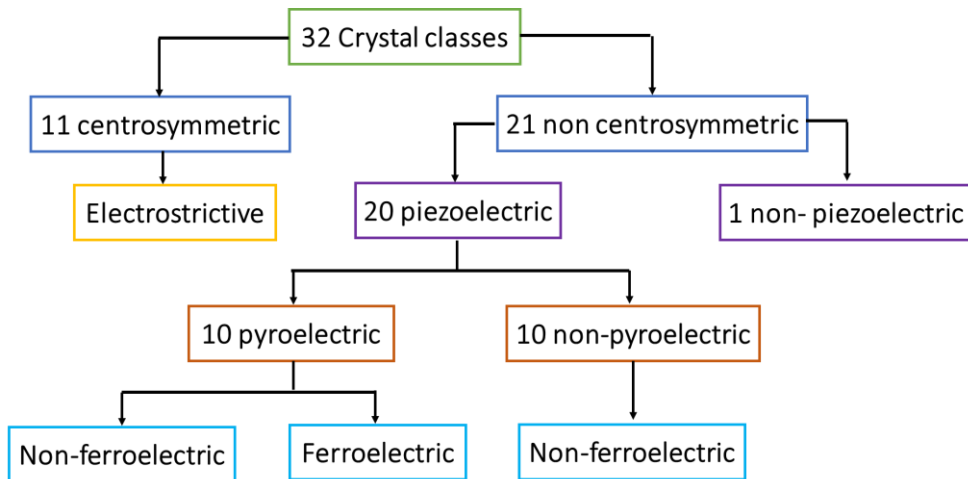


Figure 9. Crystal structures and ferroelectricity.

Ferroelectricity

Considering a crystal with several polarization domains aligned randomly, it will present an initial net polarization equal to zero in thermodynamic equilibrium (*Point A, no application of voltage, Figure 10*). However, the alignment of the polarization domains starts when a positive electric field is applied. In the small voltage regime, the polarization of the crystal increases linearly (*Path AC*). As the electric field increases (*Path CD*), the polarization domains will continue aligning until they reach a point of saturation (*Point D*). The value of *spontaneous polarization* (P_s) can be estimated by extrapolating the point of saturation limit to the “Y” axis. If the applied electric field is gradually removed, the net polarization will remain different of zero (*Path DE*), this value of polarization is known as *remnant polarization* (P_r). The polarization of the crystal can be removed if the direction of the electric field is changed (*Path EF*). The *coercive field* (E_c) value can be regarded as the required energy to bring the polarization to zero. The continue increase in the reverse field results in the complete reverse of the polarization (*Path FG*). A *negative remnant polarization* value ($-P_r$) is obtained when the reverse electric field is gradually removed. The formation of a complete polarization hysteresis loop occurs when a positive electric filed is applied again.⁵⁶

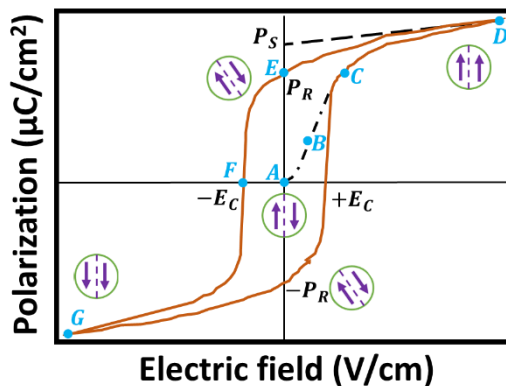


Figure 10. Ferroelectric Polarization-Electric field hysteresis loop. Adapted from ref. [56]

Piezoelectricity

The application of a mechanical force on a piezoelectric crystal leads to a generation of electrical charges (direct piezoelectric effect). Conversely, an electric field applied induces mechanical strain in a piezoelectric crystal (converse piezoelectric effect).^{57,56}

The relationship between mechanical strain and the resulting electrical polarization is known as the direct piezoelectric effect which is described by the following equation

$$P_i = d_{ijk}\sigma_{jk} \quad (2)$$

Where the electrical polarization is denoted by P_i ; the direct polarization coefficients and the stress are represented by d_{ijk} , and σ_{jk} , respectively. In the converse piezoelectric effect, the strain generated in a piezoelectric crystal is related to the applied electric field (E), where the transposed matrix is denoted by t .^{57,56}

$$s_{ij} = d_{ijk}^t E_k \quad (3)$$

In addition to the *polarization-electric field* hysteresis loop, the *strain-electric field* hysteresis loop is presented in Figure 11, which resembles the shape of a butterfly. When the electric field is equal to zero, the strain in the crystal will be zero (Point A). The crystal will expand upon the application of a positive electric field (piezoelectric effect (Eq. 2), path ABC). Point C can be seen as the maximum expansion of the crystal (under the application of an electric field). As the electric field is gradually removed, the strain will trace a line from point C to A (strain equal to zero). The reverse of the electric field (negative direction) leads to reach the point D, in this point the strain jumps from point D to E and then moves along the segment E-F upon an increase of the negative electric field. The remove of the reverse electric field leads to reach the point A. Finally, the strain-electric field hysteresis loop is completed when a positive electric field is applied again (point G).

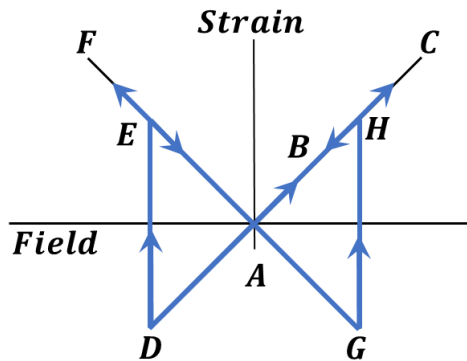


Figure 11. Strain-electric field hysteresis loop (butterfly loop). Adapted from ref. [58]

2.5 SOLID SOLUTION HAFNIUM ZIRCONIUM OXIDE

Hafnia (HfO_2) and zirconia (ZrO_2) are occasionally referred as twin materials since both have similar properties. Under standard temperature and pressure conditions they have the same color (white), similar dielectric permittivity ($\epsilon \sim 25$), similar optical band gap ($E_g \sim 5 \text{ eV}$) and also similar melting points ($T_M \sim 2600^\circ\text{C}$). The resemblance is attributable to the structural similarity between the both oxides.⁵⁹ Hafnium and zirconium elements belong to group four of the periodic table. Therefore, their ionic radii is almost similar (ionic radii for Hf^{4+} and Zr^{4+} are 0.78 \AA and 0.79 \AA , respectively).¹ This similarity allows them to be completely miscible in the solid state as shown in Figure 12. The monoclinic phase is the equilibrium phase for both structures at low temperatures, while the tetragonal and cubic phases predominate at higher temperatures. These two elements are difficult to separate and in some cases some residues of zirconium can be find in hafnia.⁶⁰⁻⁶²

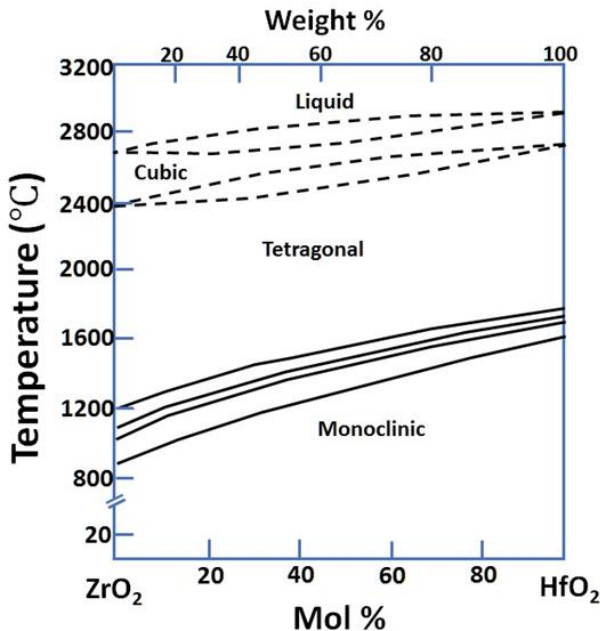


Figure 12. Phase diagram of the binary system HfO_2 - ZrO_2 . Adapted from ref. [62]

Structural properties of HfO_2 and ZrO_2

The schematic representation of the units cells for both different materials (ZrO_2 and HfO_2 systems) are presented in [Table 3](#). As stated above, both materials present three different phases. The stable alpha phases ($\alpha - HfO_2$ and $\alpha - ZrO_2$) are monoclinic at temperatures below $\sim 1800^\circ C$. As the temperature increases to higher temperatures both materials transform to beta phase ($\beta - HfO_2$ and $\beta - ZrO_2$), in this state they present a tetragonal crystal structure. At even higher temperatures both oxides ($\gamma - HfO_2$ and $\gamma - ZrO_2$) transform into a cubic crystal structure.^{[29, 62](#)}

Table 3. Structural properties of HfO_2 and ZrO_2 , from ref. [53]

Monoclinic (α -phase)	Tetragonal (β -phase)	Cubic (γ -phase)
ZrO_2: $a=5.15\text{\AA}$, $b=5.20\text{\AA}$, $c=5.32\text{\AA}$ and $\beta=80^\circ$ (below $1170^\circ C$) HfO_2: $a=5.15\text{\AA}$, $b=5.19\text{\AA}$, $c=5.33\text{\AA}$ and $\beta=99.6^\circ$ (below $1827^\circ C$)	ZrO_2: $a=5.09\text{\AA}$ and $c=5.18\text{\AA}$ ($1171^\circ C$ to $2369^\circ C$) HfO_2: $a=3.59\text{\AA}$ and $c=5.22\text{\AA}$ ($1828^\circ C$ to $2520^\circ C$)	ZrO_2: $a=5.12\text{\AA}$ (above $2370^\circ C$) HfO_2: $a=5.14\text{\AA}$ (above $2521^\circ C$)

Ferroelectric properties of hafnium zirconium oxide ($Hf_{0.5}Zr_{0.5}O_2$) film

Hafnia (HfO_2) and zirconia (ZrO_2) films combine excellent dielectric properties ($\varepsilon \sim 30$) with a relative low deposition temperature (typically $500^\circ C$).^{[1, 4](#)} These advantages makes them suitable for integration into the complementary metal oxide semiconductor (CMOS) process.^{[26, 63-64](#)} Indeed, the current generation of semiconductor memories uses high dielectric materials such as hafnia and/or zirconia films as dielectric layers for the fabrication of DRAM memory devices. Their implementation enables the increase of the gate capacitance without decreasing their physical thickness.^{[1, 4](#)}

Another interesting property of hafnia-based zirconium films is their ferroelectric property. Even though, hafnia and zirconia have been studied for more than a century, it was just recently that its ferroelectric behavior was discovered. Indeed, just six years ago (2011) Muller et al.^{[65-66](#)} reported robust ferroelectricity in an ultrathin $Hf_{0.5}Zr_{0.5}O_2$ film (~ 7.5 nm in thickness). The combination of ferroelectric properties (remnant polarization of about $15 \mu C/cm^2$ and a low

coercive field of about 0.8MV/cm) with deposition parameters compatible with the CMOS process make it an excellent candidate to be used as a ferroelectric layer in an FTJ memory.

The origin of the ferroelectricity in $\text{Hf}_{0.5}\text{Zr}_{0.5}\text{O}_2$ relies on the martensitic transformation from tetragonal phase to an orthorhombic phase. It occurs during the initial stages of $\text{Hf}_{0.5}\text{Zr}_{0.5}\text{O}_2$ film growth. First, it starts with the nucleation of small $\text{Hf}_{0.5}\text{Zr}_{0.5}\text{O}_2$ grains with a high surface-to-volume ratio, which results in the formation of a tetragonal phase ($\text{P}4_2/\text{nmc}$). However, the combination of small compressive stress (along a- and b- axis) and a large tensile strain along the c-axis induced by the coalescence of the nucleating grains leads to the formation of the ferroelectric orthorhombic phase ($\text{Pbc}2_1$). The lattice parameters of the $\text{Hf}_{0.5}\text{Zr}_{0.5}\text{O}_2$ orthorhombic phase ($\text{Pbc}2_1$) are $a=5.01\text{\AA}$, $b=5.05\text{\AA}$ and $c=5.25\text{\AA}$.^{22, 53, 66}

Hafnia and zirconia are completely miscible. However, ferroelectric behavior only appears when the molar percentages of zirconium and hafnium are around 50 % (Figure 13).^{21, 26, 67} Pure hafnia in thin film form presents a centrosymmetric monoclinic phase ($Fm\bar{3}m$). The high symmetry of the crystal structure prevents ferroelectricity, therefore it shows paraelectric behavior in a *polarization vs voltage curve* (Figure 13 (a)). On the other hand, pure zirconia in thin film form presents a non-centrosymmetric tetragonal phase ($\text{P}4_2/\text{nmc}$), which surprisingly has antiferroelectric nature (Figure 13 (e) and (f)). Hafnium-rich films exhibit predominantly monoclinic phase, which shows a certain degree of ferroelectricity (Figure 13 (b) and (c)), whereas Zirconium-rich films crystallize into a tetragonal phase (Figure 13 (e)). For films with a 50 molar percent of zirconia and 50 molar percent of hafnia, a non-centrosymmetric orthorhombic ($\text{Pbc}2_1$) phase is formed, it presents ferroelectric properties (Figure 13 (d)).²⁶

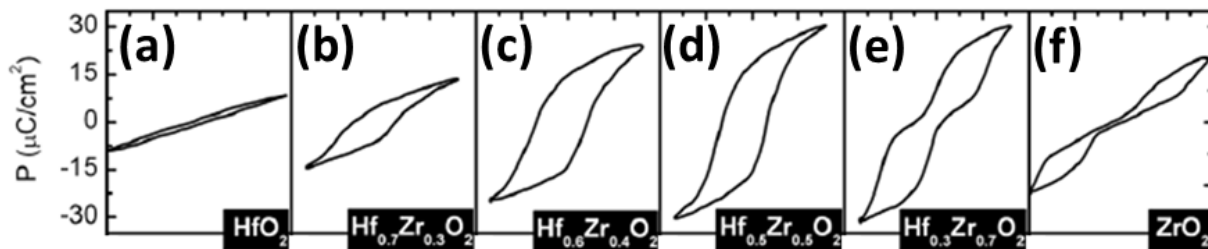


Figure 13. Evolution of the ferroelectric properties as a function of zirconium atomic concentration.
Adapted from ref. [26]

Contrary to conventional ferroelectric materials, where the ferroelectricity disappears below a certain thickness (~2 nm), in $\text{Hf}_{0.5}\text{Zr}_{0.5}\text{O}_2$ the ferroelectricity disappears above a critical thickness (~17 nm) and gets an improvement when the thickness is reduced.²² The effect of film thickness on the ferroelectricity of $\text{Hf}_{0.5}\text{Zr}_{0.5}\text{O}_2$ is presented in [Table 4](#).

Table 4. Thickness effect on the ferroelectricity of $\text{Hf}_{0.5}\text{Zr}_{0.5}\text{O}_2$. Data from Ref. [22]

Thickness	Remnant polarization ($\mu\text{C}/\text{cm}^2$)	Coercive field (MV/cm)
5.5 nm	~30	~0.8
10 nm	~20	~1.5
17 nm	~10	~2
25 nm	~0	~3

*Metal-Insulator-Metal structure= $\text{SiO}_2/\text{TiN}-\text{Hf}_{0.5}\text{Zr}_{0.5}\text{O}_2-\text{TiN}$

The solid solution $\text{Hf}_{0.5}\text{Zr}_{0.5}\text{O}_2$ can be produced via different deposition techniques ([Table 5](#)). Techniques such as atomic layer deposition, plasma-enhanced atomic layer and sol-gel enable the deposition of $\text{Hf}_{0.5}\text{Zr}_{0.5}\text{O}_2$ films at low substrate temperature (280°C). However, the as-deposited film is not crystalline, therefore it does not have ferroelectric properties.

Table 5. Survey of experimental reports on $\text{Hf}_{0.5}\text{Zr}_{0.5}\text{O}_2$.

Substrate	Deposited layer	Deposition technique	Main remarks	Ref
Silicon	Zr doped HfO_2 10- 90 at. %	MALD ($T_S=500^\circ\text{C}, T_A=600^\circ\text{C}$)	HZO dielectric properties	[68] 2009
Silicon	$\text{Hf}_{1-x}\text{Zr}_x\text{O}_2$ $X = 0-1$ at. %	PALD ($T_S=280^\circ\text{C}, T_A = 950^\circ\text{C}$)	HZO structural properties	[29] 2010
TiN	$\text{Hf}_{0.5}\text{Zr}_{0.5}\text{O}_2$	ALD ($T_S=280^\circ\text{C}, T_A = 550^\circ\text{C}$)	Thermal cycles on HZO films	[69] 2013
Pt	$\text{Hf}_{0.5}\text{Zr}_{0.5}\text{O}_2$	Sputtering ($T_S=500^\circ\text{C}, T_A = -^\circ\text{C}$)	Charge-trapping memory	[67] 2014
TiN	$\text{Hf}_{0.5}\text{Zr}_{0.5}\text{O}_2$ $t_F = 12-60 \text{ nm}$	Sol-gel method ($T_S=-^\circ\text{C}, T_A = 700^\circ\text{C}$)	Synthesis by a wet technique	[70] 2015

HZO stands for $\text{Hf}_{0.5}\text{Zr}_{0.5}\text{O}_2$, MALD (Metalorganic atomic layer deposition), PALD (Plasma-enhanced atomic-layer)

To crystallize the as-deposited film, it is necessary to apply a thermal treatment at relative high temperatures (450-950°C).^{29, 68-70} However, RF-magnetron sputtering can produce crystalline $\text{Hf}_{0.5}\text{Zr}_{0.5}\text{O}_2$ films in one single step. Indeed, Lu et al. reported in 2014, the crystallization of an ultrathin $\text{Hf}_{0.5}\text{Zr}_{0.5}\text{O}_2$ films by RF magnetron sputtering.⁶⁷ In the present work, the deposition of $\text{Hf}_{0.5}\text{Zr}_{0.5}\text{O}_2$ films is achieved by RF-Magnetron sputtering as it offers many advantages such as crystallization of materials at low temperatures, control of the deposition rate, uniform deposition over relative large areas ($1 \times 1 \text{ cm}$) as well as an easy scaled-up.

2.6 ELECTRONIC CHARGE TRANSPORT AT THE SEMICONDUCTOR INTERFACE

In FTJ devices, the electron current flow across the whole device is defined by the width and shape of the electrostatic potential profile.^{30,52} In semiconductor memory device technology, the charge transport at the interfaces is one of the most important properties and it has become an essential issue of modern electronic device design.¹⁴

Heterostructures

Semiconductors have an energy level diagram as shown in Figure 14. The distance between valence band (E_V) and the conduction band (E_C) is known as band gap (E_g). Fermi level (E_F) is placed inside of the band gap. The electron affinity (χ) is the energy difference between the vacuum level and the conduction band (E_C) while the work function (ϕ) is the distance between vacuum level and the Fermi level.⁷¹

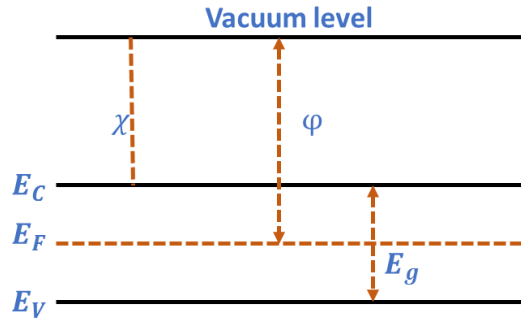


Figure 14. Typical energy band diagram for a semiconductor. Adapted from ref. [71]

The energy-band diagram of a semiconductor p-type and n-type in non-contact (neutral state) are presented in Figure 15. The junction of both semiconductors leads to a change at the interface. Band line up of their energy band will occur until the alignment of the Fermi levels energy of both semiconductors is reached. In this process, the electrons flow from the semiconductor with the higher Fermi level to the semiconductor with the lower Fermi level. This electron transfer is compensated by the built up of an electric field.⁷¹

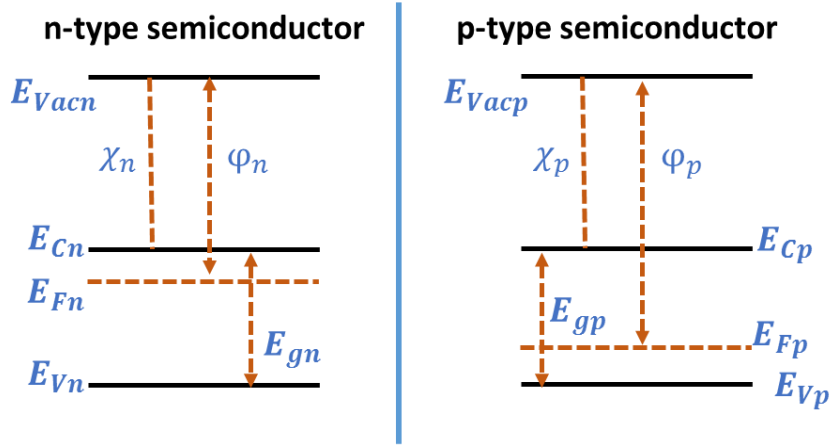


Figure 15. Energy band diagram for n- and p-type semiconductors in non-contact. Adapted from ref. [71]

These heterostructures can be classified into three categories (Figure 16): Type-I (straddling), where one of the semiconductors presents both lower conduction band energy (E_C) and higher valence band energy (E_V), as well as a smaller energy band gap (E_g). Type-II (staggered) occurs when the conduction (E_C) and the valence (E_V) band energies of one the semiconductors are lower respect to the conduction (E_C) and valence band (E_V) of the other semiconductor, respectively. Type-III (broken-gap) here the conduction band energy (E_C) of one of the semiconductors is lower than the valence band energy (E_V) of the other.⁷¹

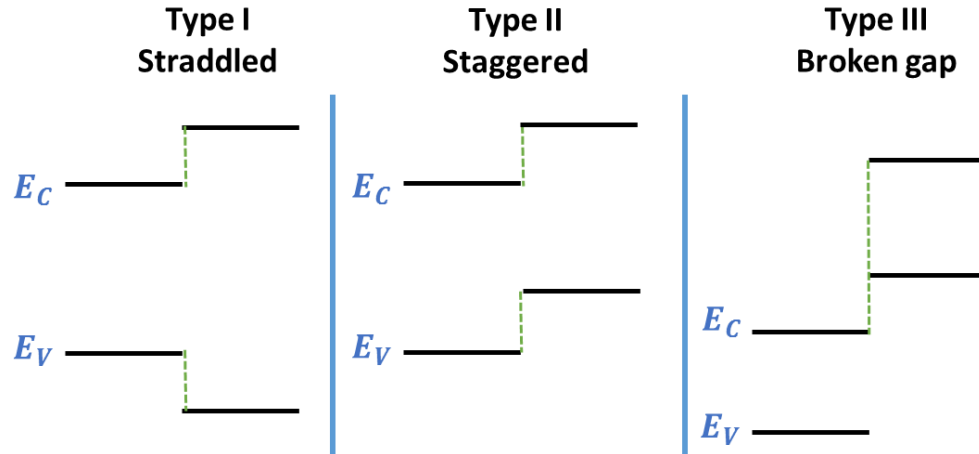


Figure 16. Classification of the heterostructures: Type I (Straddled), Type II (Staggered) and Type III (Broken gap). Adapted from ref. [71]

2.7 CHARGE TRANSPORT IN METAL-INSULATOR-METAL DEVICES

In metal (semiconductor)-insulator-metal structures, the conduction mechanism depend on the metal (semiconductor)/insulator interface. The most important parameters in this type of conduction mechanisms are the barrier height and barrier width. The conduction mechanisms at the interface are attributed to Fowler-Nordheim tunneling, thermionic emission and direct tunneling. The former conduction mechanism dominates at low-voltage regimes, as the barrier thickness increases direct tunneling is less predominant due to thermionic emission current becomes more dominant. At high-voltage regime Fowler-Nordheim tunneling is main current mechanism.^{30, 52}

Fowler-Nordheim Tunneling

Fowler-Nordheim is characterized by an electrostatic potential barrier with triangular shape (Figure 17). It is formed when the applied electric field is high enough to change the rectangular or trapezoidal shape of the electrostatic potential barrier. Fowler-Nordheim tunneling occurs at high-voltage regime. Here the electron wave function can penetrate through the triangular potential barrier.^{30, 52, 72}

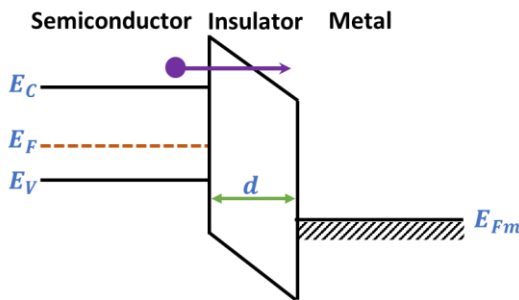


Figure 17. Fowler-Nordheim tunneling through a trapezoidal barrier. Adapted from ref. [72]

The Fowler-Nordheim tunneling obeys the following expression:

$$J = \frac{q^3 E^2}{8\pi h q \varphi} \exp\left[\frac{-8\pi(2qm)^{1/2}}{3hE}\varphi^{3/2}\right] \quad (4)$$

Where J is the Fowler-Nordheim tunneling current density, q is the electron charge, m is the free electron mass, φ is the electrostatic potential barrier height, E is the electric field across the barrier and h is the Plank's constant.^{30, 52, 72}

Thermionic emission

Thermionic emission is associated with thermal activation. In general, when the electrons from the metal or semiconductor obtain enough energy by thermal activation, they can overcome the energy barrier at the metal(semiconductor)/insulator interface ([Figure 18](#)). In this case, the diffusion current occurs due the injection of carriers over the barrier. The diffusion current in that region should not be a limiting factor. Therefore, the region behind the barrier has to be either n-type semiconductor, or a metal layer.^{[30, 52, 72](#)}

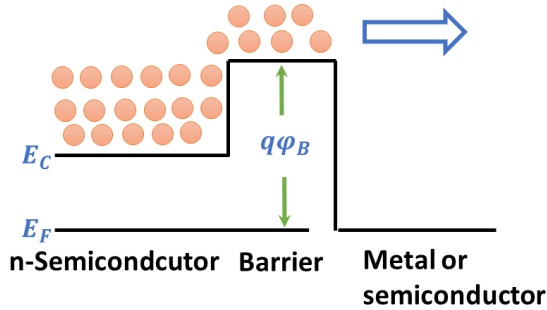


Figure 18. Thermionic emission of an electron over a barrier. Adapted from ref. [72]

The expression of [Eq.5](#) integrates the number of carriers above the barrier height. This portion of the thermally-generated carrier is no longer confined by the barrier so they can contribute to the thermionic-emission current.^{[30, 52, 72](#)} The total electron current over the barrier is given by

$$J = A^* T^2 \exp\left(\frac{-q(\varphi - \sqrt{qE/4\pi\varepsilon_r\varepsilon_0})}{kT}\right) \quad (5)$$

Where φ is the barrier height, and A^* is the effective Richardson constant

$$A^* \equiv \frac{4\pi q k^2 m}{h^3} \quad (6)$$

Where J is the thermionic current density, m is the free electron mass, T is the absolute temperature, q is the electron charge, E is the electron field across the barrier (voltage (V)/width (barrier thickness)), k is the Boltzmann's constant, h is the Planck's constant, ε_0 is the permittivity in vacuum and ε_r is the permittivity of the film.

Direct tunneling

In classical mechanics, an electron will remain confined by a potential barrier if it presents lower energy than the potential barrier height. However, quantum mechanics takes into consideration the dual character of an electron (wave nature). Thus, as a wave the electron does not terminate abruptly in the potential barrier. Therefore, there is a finite probability for the electron to exist inside of the barrier or outside in case it is thin enough.⁷² The leaking of an electron through a potential barrier is known as the tunneling effect.⁷²

In 1958, L. Esaki discovered the tunnel diode. It can be seen as a simple junction between two semiconductors (n-type and p-type, Figure 19 (a)).⁷² A *current-voltage* characteristic curve of a tunnel diode is presented in Figure 19 (b) (temperature equal to zero kelvin). The application of an electrical field (V) leads to a monotonically increase of the electrical current (I). This trend will continue until it reaches a maximum of electrical current value (I_p). The constant application of an electric field results in the decrease of electrical current (I_v). However, the electrical current will increase exponentially if a large electric field is applied.⁷²

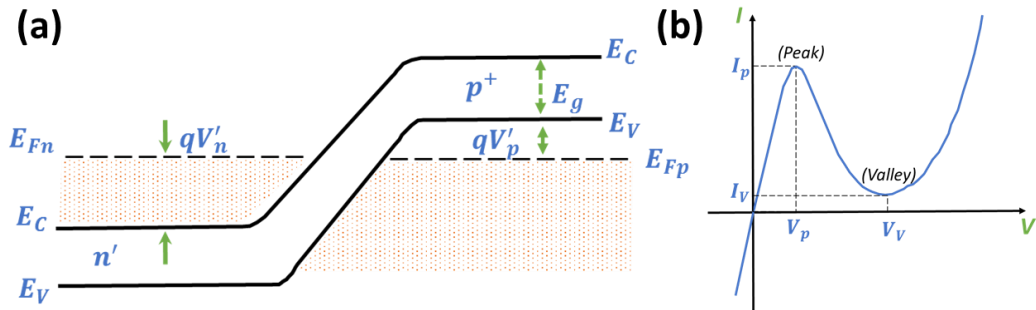


Figure 19. Tunnel diode (a) Energy-band diagram in thermal equilibrium and (b) A current-voltage characteristic curve (temperature equal to zero kelvin). Adapted from ref. [72]

During his Ph.D. studies, L. Esaki determined the following conditions necessary to present direct tunneling current from the conduction band of an n-type semiconductor to the valence band of a p-type semiconductor:

- The side from which the electron tunnels must be filled with occupied energy states
 - The side into which the electron must have unfilled energy states
 - The potential barrier height should be low, and the potential barrier width should be thin.
 - During the tunneling process, momentum is preserved
-

The tunneling process using a simplified band structure is presented in Figure 20 (at absolute zero temperature). In the same figure, below the band structure is presented a current-voltage curve where the tunneling current is depicted by one dot.⁷² At zero voltage the total tunneling current is equal to zero (Figure 20 (a)). Once an electric field is applied, the electrons that are inside the conduction band of an n-type semiconductor will tunnel to the p-type semiconductor side in order to fill the unoccupied energy states in the valence band (Figure 20 (b)). An increase of the electric field leads to a decrease of the number of common energy states (Figure 20 (c)). At this point the bottom edge of the conduction band of the n-type semiconductor is placed at the same energy level of the top valence band of the p-type semiconductor, when the bands are uncrossed the tunneling current no longer flow (*current-voltage* curve Figure 20 (c)). However, when a forward electric field is further applied, the tunneling current no longer dominates. Normal diffusion currents start to become the dominant current mechanism (Figure 20 (d)). When the direction of the electric field is reversed, the electrons will tunnel from valence band of a p-type semiconductor to the conduction band of n-type semiconductor (Figure 20 (e)).⁷²

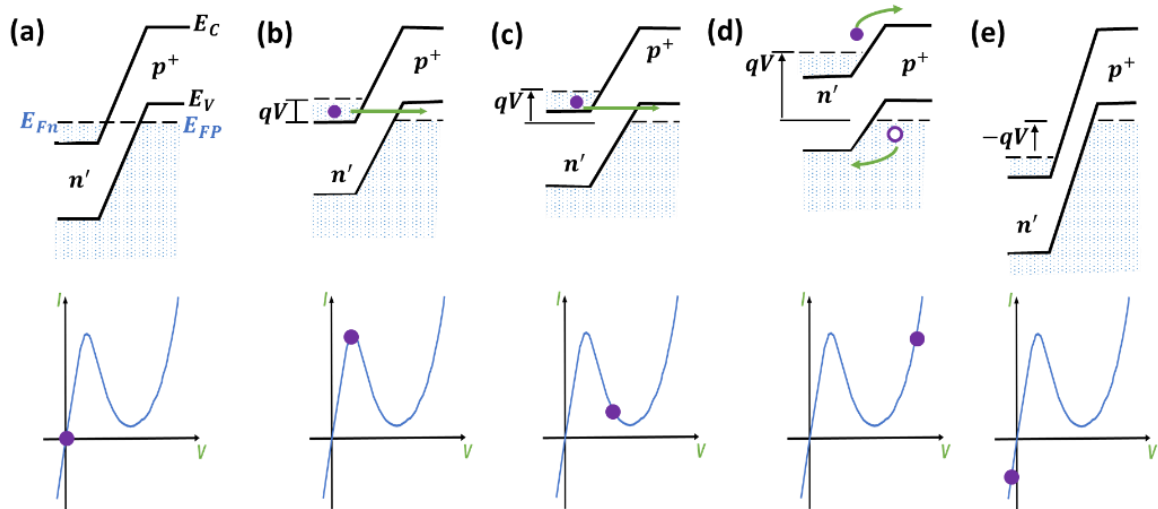


Figure 20. Simplified energy-band diagram of a tunnel diode at (a) thermal equilibrium (zero bias), under the application of (b) a small bias, (c) a medium bias, (d) a large bias, and (e) reverse of the bias.
Adapted from ref. [72]

Direct tunneling equation

The tunneling current density (J) can be determined by two different models: tunnelling current through a trapezoidal or through a rectangular barrier shape. In both cases the electrostatic potential barrier depends on polarization orientation.

For a potential barrier with a thickness d and dissimilar potential barrier heights ($\varphi_1 \neq \varphi_2$), the following analytical expression is obtained

$$J = -\left(\frac{4em}{9\pi^2\hbar^3}\right) \left(\frac{\exp(\alpha(V)[(\varphi_2 - \frac{eV}{2})^{\frac{3}{2}} - (\varphi_1 + \frac{eV}{2})^{\frac{3}{2}}])}{\alpha^2(V)[(\varphi_2 - \frac{eV}{2})^{\frac{1}{2}} - (\varphi_1 + \frac{eV}{2})^{\frac{1}{2}}]^2} \right) \times \sinh\left(\frac{3}{2}\alpha(V)[(\varphi_2 - \frac{eV}{2})^{\frac{1}{2}} - (\varphi_1 + \frac{eV}{2})^{\frac{1}{2}}]\frac{eV}{2}\right) \quad (7)$$

Where $\propto(v) = [4d(2m)^{1/2}]/[3\hbar(\varphi_1 + eV - \varphi_2)]$, V is bias voltage and \hbar is the reduced Planck constant.

On the other hand, for a potential barrier with a thickness s and similar potential barrier heights ($\varphi_1 = \varphi_2$), an analytical expression for the current density is obtained

$$J = \left[\frac{3(2m\varphi)^{\frac{1}{2}}}{2s}\right] \left(\frac{e}{h}\right)^2 V \times \exp\left[-\frac{(4\pi s)}{h}(2m\varphi)^{\frac{1}{2}}\right] \quad (8)$$

Chapter 3 Characterization tools

This chapter presents the experimental methodology to fabricate and evaluate our FTJ memory devices. In general our experimental set up is divided into three different sections: i) fabrication of the FTJ memory device, ii) characterization of the thin films and iii) evaluation of the semiconductor memory. Following this order, Chapter three starts by describing the fundamentals of sputtering deposition, including a detail description of the thin film deposition system. The second section presents a description of some analytical techniques such as X-ray diffraction and X-ray photoelectron spectroscopy and the third section concludes with the operation principle of different scanning probe techniques such as atomic force microscopy, piezoresponse force microscopy and conductive-atomic force microscopy.

3.1 DEPOSITION TECHNIQUES

In this work, the growth of our film started from a source material in solid state (ceramic target) that was vaporized in order to obtain neutral species (atoms) from the target surface, which were transported to the substrate surface. This vaporization process occurs by bombarding the source material surface (ceramic target) with positive ions under high vacuum conditions (chamber pressure~ 10^{-3} Torr), this process is known as sputtering.^{55, 73-74}

Sputtering

In sputtering, argon ions (electrical positive charges) are used to bombard the surface of a target. The argon bombardment results in the ejection of atoms from the target, which travel to the substrate surface.⁷⁵ If the target is made of different elements (such as Hf_{0.5}Zr_{0.5}O₂), the atoms will be ejected at different rates (sputtering yield of Hf~0.8 and Zr~0.7), this difference in deposition rate leads to changes in the film stoichiometry. In order to ensure the right transfer of the atomic species from the target to the substrate is necessary to perform a pre-sputtering process.⁷³ It consists in bombarding the target surface with argon ions prior film deposition. During this process the substrate surface is covered with a shutter ([Figure 21](#)), which prevents contamination and damage of the substrate.

Reactive radio-frequency magnetron sputtering

The term “reactive sputtering” is associated to the use of gases that reacts chemically with the as-deposited film during the deposition process. Since, some of the targets used in the present work are oxides ($\text{Hf}_{0.5}\text{Zr}_{0.5}\text{O}_2$ and BaTiO_3) and nitrides (TiN), it is necessary to maintain a certain concentration of gas inside of the vacuum chamber. Oxygen gas is required for depositions of oxide films while nitrogen gas is used for the deposition of nitride films.^{55, 73-74}

In sputtering the formation of plasma can be provided by either a *DC* (direct current) or an RF (radio frequency) source power. The choice of the source power is determined by the electrical nature of the target. For example, *DC* sputtering works well for conductive targets (metals) while radio-frequency sputtering is used for the deposition of non-conductive targets. This RF-source produces a capacitive environment around a non-conducting target that allows the stable formation of a plasma. The RF source used as a power supply is commonly used with a frequency of 13.56 MHz.^{55, 73-74}

In order to enhance the argon bombardment on the target surface it is required to place a magnetron at the backside of the target. This magnetron generates a toroidal magnetic field that confines electrons near the target surface. In consequence, the positive argon ions (provided by the plasma) will be accelerated towards the target surface.⁷⁵

The sputtering unit used in this study is a computer controlled table top deposition system (SPT310 Plasmionique Inc, [Figure 21](#)). The stainless steel chamber has a cylindrical shape with 20 cm in diameter and 31 cm height. The system has three magnetron guns (1-inch diameter) mounted at the top of the chamber. The substrate holder shown in [Figure 21](#) is a 5 cm diameter plate to which the samples can be mounted and its temperature is controlled by a thermo-couple

(Type K) and a proportional–integral–derivative controller. *DC* or *RF* power can be applied from any of the available power supplies to any of the three guns or substrate. Cooling of the magnetrons is done with a water system in order to prevent damage of the magnetron.

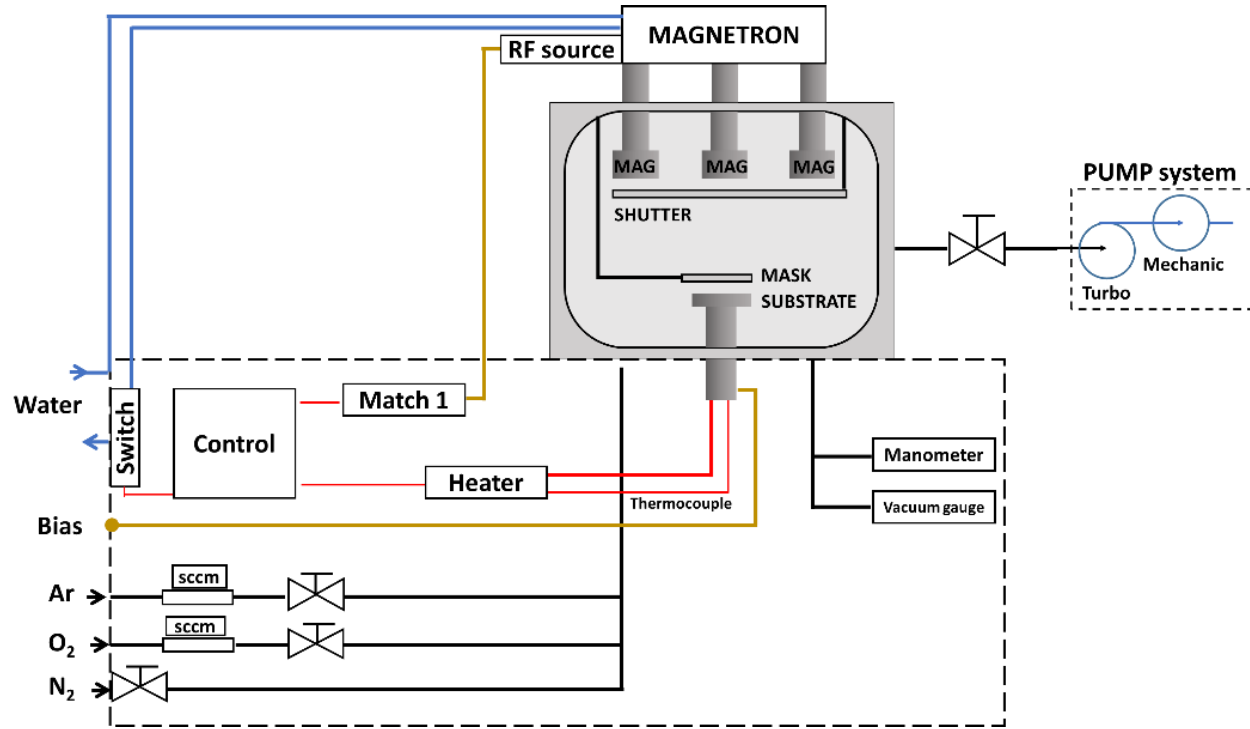


Figure 21. Schematic representation of the sputtering deposition system (one plasma source) used in the present thesis.

3.2 STRUCTURAL CHARACTERIZATION TOOLS

X-ray diffraction (XRD)

X-ray diffraction is a non-destructive technique for the characterization of the crystallographic structure of some materials. This technique consists in the generation of X-rays (electromagnetic waves with short wavelength) which interacts with the electrons of the atoms of the material under investigation. From this interaction is produced a characteristic diffraction pattern that reveals the crystal structure of the material.^{76,77}

The atoms in a crystalline material are arranged in a regular three-dimensional distribution in space (Figure 22). This arrangement leads to the formation of parallel planes that are separated by a distance “ d_{hkl} ” (it depends on the material). When a crystalline material is subjected to a monochromatic X-ray beam with a specific wavelength (λ) at an angle (Θ), diffraction will only occur if the distance traveled by the X-rays (reflected from the successive planes) differs by an integer multiple “ n^{th} diffraction order” of wavelengths (Bragg’s law,). The angular position and the intensities of the diffracted peaks produces a pattern, which is characteristic of the sample.^{76,77}

$$n\lambda = 2ds\sin\theta \quad (9)$$

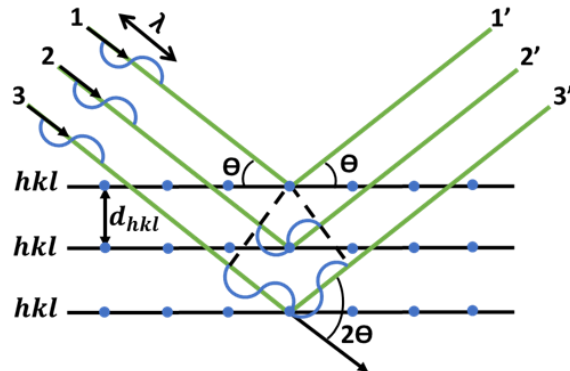


Figure 22. Bragg diffraction in a crystal. Adapted from ref. [77]

Glancing incident X-ray diffraction (GIXRD)

In a conventional X-ray diffraction technique, the penetration depth of the X-rays can be larger than the film thickness. As a consequence, the resulting diffraction pattern will be composed of undesired substrate peaks and a background noise. Therefore, for the X-ray diffraction analysis of thin films, it is important to reduce as much as possible the signal of the substrate. In *glancing incident X-ray diffraction*, the diffraction from the film layer is enhanced by reducing the angle of incidence to a small value (0.5° to 3°). Then, GIXRD is used for phase analysis of crystalline thin films (thickness below 100 nm).^{76,77}

X-ray specular reflectivity (XRR)

This technique is used to measure the thickness, rms surface roughness and the average density of thin films. The X-ray reflectivity data shows oscillations (Kiessig Fringes, Figure 23) for which the space between the maxima of these oscillations corresponds to the film thickness, the position of the critical angle is related to the film density and the signal of the background is associated to the film roughness.⁷⁶

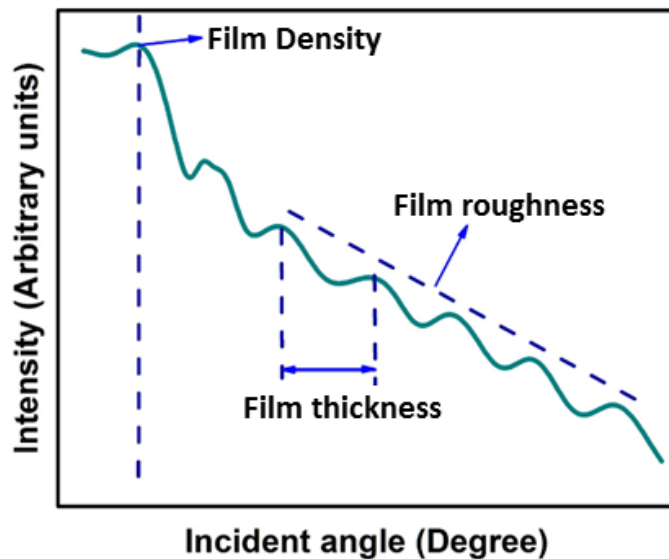


Figure 23. Interpretation of the X-ray reflectometry data. Adapted from ref. [76]

The density of a film is determined from the critical angle (θ_c). It is found where the intensity of the curve abruptly decreases (Figure 23). As shown in Eq. 10, the value of the critical angle leads to the determination of the film density

$$\theta_c = \sqrt{\frac{r_0 \lambda^2 N_A [\Sigma(f1+f2)]}{\pi A}} \rho \quad (10)$$

Where r_0 represents the Bohr electron radius ($r_0 = 2.813 \times 10^{-6} \text{ nm}$), $\Sigma(f1)$ is the atomic form factor (e^-/at), A is molar mass of the film material (g/mol), N_A is the Avogadro number ($6.02 \times 10^{23} \text{ at/mol}$) and λ is the wavelength of radiation source ($CuK\alpha = 1.5418 \text{ \AA}$).

The film thickness (t) was obtained from Eq. 11. It considers the direct maxima or minima values of a fringe as well as the critical angle of an X-ray reflectivity spectrum.

$$t = \frac{n\lambda}{2\sqrt{\cos^2 \theta_c - \cos^2 \theta_i}} \quad (11)$$

Where n is the number of the minima or maxima value taken into account after the critical angle (θ_c), θ_i represents the angle of the fringe, λ is the wavelength of radiation source ($CuK\alpha = 1.5418 \text{ \AA}$).

3.3 CHEMICAL CHARACTERIZATION TOOLS

X-ray Photoelectron Spectroscopy (XPS)

X-ray photoelectron spectroscopy (XPS) is a surface analysis technique used to study the band structure and binding energy of a sample. This technique consists in illuminating the surface of a sample with a monochromatic X-ray beam. In this process, a photon of a well-defined energy ($h\nu$) is absorbed by an electron (with a binding energy E_{BE}) of the material surface under investigation, which is subsequently ejected from the sample surface with a certain kinetic energy ($h\nu - E_{BE}$).⁵⁸ Due to energy conservation of the binding energy of an electron, it is possible to determine photoemission energy:

$$E_b = h\nu - E_{BE} - \varphi_s \quad (12)$$

Where E_b is the binding energy, $h\nu$ is the monochromatic light energy, E_{BE} is the measured kinetic energy of the electron and φ_s is a small correction due to the work function of the spectrometer. The spectrum obtained from XPS is defined as the numbers of detected electrons versus electron energy. From Eq. 12 can be seen that the peaks presented in a XPS spectrum are related to the core electronic level electrons and even to the electrons from the valence and conduction bands.⁵⁸

In this project, the surface analysis of the as-deposited was analyzed with X-ray photoelectron spectroscopy (VG Escalab 3 MKII). X-ray photoelectron spectra are collected using an X-ray anode that produces AlK α radiation ($E=1500$ eV), operated at 300W. Analyzer pass energies of 100 eV and 20eV were used for collection of survey and high resolution scans, respectively. All measurements were taken in ultrahigh vacuum (10^{-9} Torr). The hydrocarbon C1s peak (285.00 ± 0.05 eV) was used to reference all the reported binding energies, and the Au 4f line (84.00 ± 0.05 eV) to calibrate the spectrometer energy scale.

CASA XPS software was used to determine the chemical structure and composition of the thin films. The curve fitting in CASA XPS was performed using a line shape with Voigt functional form (a simple convolution of Gaussian and Lorentzian) while Shirley backgrounds were introduced to reduce the asymmetry of the peak and allow for the characterization of the intensity

under the peak. To quantify the percentage atomic concentration the CASA XPS software utilized the following formula

$$X_A = \frac{(I_A E^\alpha) / (R_A T(E))}{\sum (I_i E^\alpha) / (R_i T(E))} \quad (13)$$

Where R_i is the relative sensitivity factor for the measured intensity (I_A) and is the transmission function for the instrumental operation mode used to measure the intensity (I_i) at a kinetic energy (E).

3.4 MICROSTRUCTURAL CHARACTERIZATION TOOLS

Scanning probe microscopy comprises a set of techniques based on the use of a very fine probe (curvature radius ranges from 1 nm to 50 nm). This probe is used to generate an image of the surface topography of a sample as well as to measure certain properties of the sample (electrical, magnetic, optical, and mechanical properties).

Atomic Force Microscopy (AFM)

The AFM system (Figure 24) uses a sharp tip (mounted on a cantilever) to scan over the surface of a sample in order to generate images of the topography. The interaction between the tip and the sample surface causes deflections on the cantilever. These deflections are monitored by the displacement of a laser, which is reflected onto a four quadrant photodiode detector (photo detector). The sample under investigation is placed over a macro-positioner (piezoelectric scanner) which can be displaced in three dimension, (along the “Z” direction for maintaining a contact force, and “X-Y” for scanning).^{56, 58}

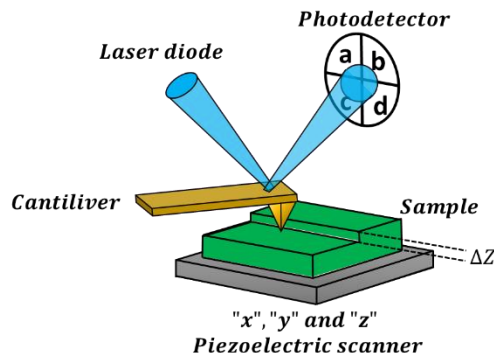


Figure 24. Setup of a basic AFM. Adapted from ref. [58]

The AFM has three operational modes called contact, non-contact and tapping modes (Figure 25). The selection of the AFM operation mode depends on the selection of tip-sample interaction forces regimes. For example in contact mode, the distance between the probe and the surface is small (a few angstroms). This mode is dominated mainly by repulsive forces (Figure 25, red line). In dynamic mode the probe/substrate surface distance increases to a few nanometers. In this mode Van der Waals interactions are the dominant force (Figure 25, blue line). In non-contact

mode, the probe-sample distance reaches tens of nanometers and is large enough that the probe-sample forces are too weak to be detected by the system (Figure 25, green line).^{56, 58}

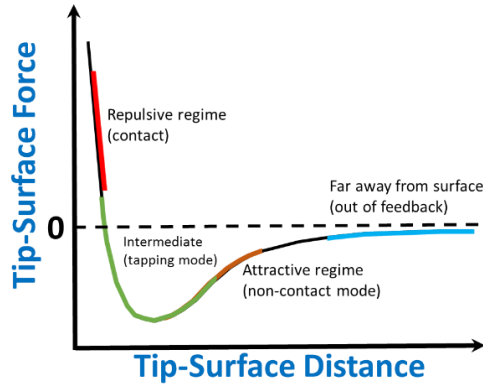


Figure 25. The repulsive and attractive force regimes as the AFM tip approaches the sample. Adapted from ref. [56]

Piezoresponse force Microscopy (PFM)

Piezoresponse force microscopy (PFM) is used to determine if one material is ferroelectric or not. The physical mechanism of PFM lies on the detection of local vibration of a sample through the converse piezoelectric effect. As shown in Figure 26 a conductive tip is brought into contact with the surface of a piezoelectric material. The tip is used to apply an AC bias across the sample. The generated electric field produces a mechanical deformation of the sample due to the converse piezoelectric effect. This mechanical deformation is detected by a four quadrant AFM photodiode detector via cantilever deflections. The AC deflection signal is analyzed with a lock-in amplifier. In this process, the AC signal is decomposed into PFM amplitude and phase signals.⁵⁷⁻⁵⁸

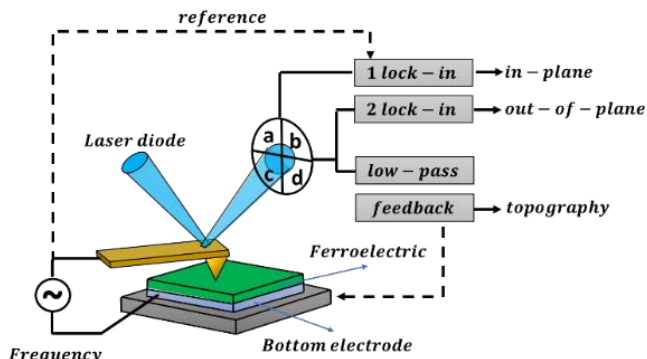


Figure 26. Schematic of a PFM set-up. Adapted from ref. [58]

Conductive Atomic Force Microscopy (C-AFM)

Conductive-AFM is used to create a current map image of the surface of a sample. It uses a conductive tip (in contact mode) to measure electrical current through the sample due the application of a *DC* bias. As shown in the schematic of [Figure 27](#), the AFM system is connected to a current amplifier to sense small current (sensitivity down to sub-picoampere range). A part of generate current maps, the C-AFM can be used in local current-voltage spectroscopy mode. In general, C-AFM is a technique that allows to study local electrical transport behavior such as polarization couple resistive switching behavior in an ferroelectric tunnel junction device.⁵⁶

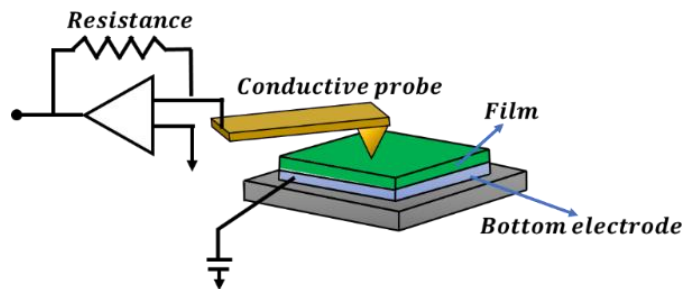


Figure 27. Schematic representation of a C-AFM set up. Adapted from ref. [58]

A commercial AFM system (AIST-NT, SmartSPM™ 1000), was used for characterization of the surface morphology, ferroelectric properties and electric switching of the films. The surface morphology of each film was analyzed by scanning a silicon probe in dynamic mode (cantilever length: 125 μm , force constant: 40 N/m and resonance frequency: 325 kHz). For PFM imaging, Pt-Ir coated silicon tips were used (cantilever length: 225 μm , width: 45 μm , thickness: 3 μm , force constant: 3 N/m and resonance frequency: 60 kHz) in off-PFM resonance mode (a contact resonance frequency of about 51 kHz). Regarding C-AFM measurements, local current-voltage (I-V) characteristics were measured by positioning a conductive Pt-Ir coated silicon tip at a selected point on the top electrode surface and by sweeping a *DC* voltage.

Chapter 4 Ferroelectric tunnel junction based on BaTiO₃

This chapter reports a process for the sputtering deposition of barium titanate (BaTiO₃) thin films on niobium doped strontium titanate (Nb:SrTiO₃ (100)) semiconducting substrates. We observe substrate etching and non-stoichiometry in the film composition at high RF-power and low processing pressure. However, films deposited at high deposition pressure (20 mTorr) and low RF power (10W) resulted in stoichiometric BaTiO₃. Layer-by-layer (2D) growth mode, prerequisite for epitaxial BaTiO₃ on Nb:SrTiO₃ (100) substrates, were realized at a substrate temperature of 600°C. Hysteresis loops (*PFM phase vs applied voltage*) in piezoresponse force microscopy (PFM) confirm ferroelectricity of the ultrathin BaTiO₃ films.

4.1 BARIUM TITANATE THIN FILM

Barium titanate (BaTiO₃), the first perovskite ferroelectric oxide discovered in the 1940s, is a prototypical displacement type ferroelectric for which the origin of ferroelectricity is derived from the displacement of ions relative to each other.⁷⁸ Even 70 years after that discovery, BaTiO₃ is still the most widely used material in multilayer capacitors. BaTiO₃, in single crystal, ceramic, and thin film forms has been studied extensively due to the superior electrical and optical properties, which are exploited in electro-optic switches, pyroelectric detectors, optical modulators, shutters, imagers, and displays to name a few.⁷⁹ However, the recent interest in BaTiO₃ is due to the existence of ferroelectric properties down to a thickness of about 2-3 nm. This offers the possibility of exploiting the polarization in controlling the tunneling current as predicted theoretically, the hysteretic current–voltage characteristics.⁸⁰ The control or dependence of tunneling current on the polarization direction resulted in the realization of ferroelectric tunnel junction devices that are attracting the attention due to the possibility of realizing ultra-fast, high density non-volatile memory, paving the way for “oxide electronics” into the standard semiconductor industry.⁸¹⁻⁸⁶

Thin films of BaTiO₃ can be realized with methods such as hydrothermal, pulsed laser deposition, metal organic chemical vapor deposition (MOCVD), various forms of sputtering,

molecular beam epitaxy, evaporation, sol-gel, etc. Among these methods, radio frequency (RF) magnetron sputtering is considered here due to the fact that it offers good control of the deposition rate, uniformity over a large area with potential interest for industrial mass production. Transferring the target stoichiometry to the growing films is challenging with on-axis RF-magnetron sputtering from BaTiO₃ targets due to the by-production of negative ions (O⁻) along with the production of neutral target atoms during the sputtering of the target with positively charged ions (Ar⁺). These negative ions get sufficient kinetic energy along the axis from the target RF-bias field to bombard the substrate, which significantly alters the stoichiometry of the deposit and in the worst case, even a substrate etching might occur.⁸⁷ Typical threshold energies for knocking out atoms from the surface are in the 20 - 50 eV range,⁸⁸ which is much higher than the surface binding energy (4 to 8 eV) of the atoms. The negative ions produced at the target surface are accelerated towards the substrate direction and bombard the film surface with energies that could be as high as the bias voltage on the target. At 100 V, these negative ions cause significant re-sputtering and etching of the substrate. To avoid this effect, in RF-magnetron sputter deposition of BaTiO₃, off- axis geometries are generally employed, where the substrate is kept away from the target axis. Hence, for on-axis sputter deposition, the processing parameters must be optimized, in order to minimize the energy of negative ions impinging the substrate and hence reduce their effect on the deposited film. In the present study, process optimization of BaTiO₃ is discussed to avoid this substrate etching and to obtain uniform stoichiometric BaTiO₃ film on Nb-SrTiO₃ (100) substrate.

4.2 EXPERIMENTAL SECTION

Substrate preparation: Conducting single crystalline and polycrystalline substrates were used for the BaTiO₃ deposition in the present study. In the case of conducting polycrystalline substrates, as bottom electrodes, a double-layer structure consisting of 100 nm -thick platinum films on a 5 nm-thick Al₂O₃ film was used ([appendix B](#)). The latter serves as an adhesion layer to improve the sticking of platinum on the SiO₂/Si substrates and the resulting structure was Pt/Al₂O₃/SiO₂/Si. In the case of conducting single crystalline substrates, Nb:SrTiO₃ (5 × 5 × 0.5 mm, miscut angle <0.5°, 0.5 wt. %Nb) with (100) orientation from Crystec GmbH

were used for growth epitaxial BaTiO₃ films. The surface morphology was investigated by atomic force microscopy (Smart SPM1000-AIST-NT Inc.) in tapping mode.

Prior to deposition, as-received Nb: SrTiO₃ substrate was etched hydrothermally in water and then annealed in oxygen atmosphere to ensure single termination (Figure 28 (a)).⁸⁹ The AFM characterization revealed an average rms terrace roughness around 0.15 nm. As can be seen in the inset of Figure 28 (a), the line scan showed an average step height of 0.4 nm, suggesting a single termination of SrO or TiO₂.⁸⁹ In Figure 28 (b), the AFM surface morphology showed polycrystalline granular features of the platinum surface (X-ray diffraction studies revealed Pt orientation along (111) direction, Appendix B) with an rms roughness of about 1.6 nm. As the actual surface morphology of the as-received Pt/Al₂O₃/SiO₂/Si substrate found to be depended on the deposition temperature, we used a standard pre-anneal, i.e., 30 min at 700°C, to stabilize the Pt microstructure before deposition.

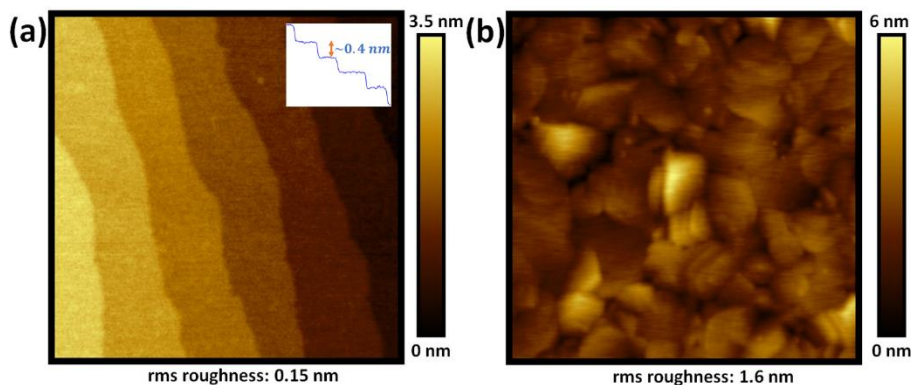


Figure 28. AFM topography of (a) a Nb:SrTiO₃(100) substrate water etched and then annealed at 1000 °C, inset shows the line scan with steps height around 0.4 nm, and (b) a Pt/Al₂O₃/SiO₂/Si substrate annealed at 700 °C.

Deposition procedure: The BaTiO₃ deposition was realized on these substrates by conventional on-axis RF magnetron sputtering at various temperatures (25°C to 800°C). A polycrystalline BaTiO₃ ceramic disc (2.54 cm diameter and 0.317cm thickness) was used as the sputtering target. Prior to the deposition, the chamber was evacuated to at least a base pressure of $\sim 10^{-5}$ Torr using a dry pumping station. The sputtering medium was a gas mixture of Ar and O₂ [oxygen partial pressure, $P_O = O_2/(Ar+O_2) = 0$ to 100%] and the operating pressure was in the range 5–30 mTorr. An upstream PID (proportional-integral-derivative) controller, maintained a constant pressure throughout the deposition. The target was pre-sputtered for 15 min, while keeping the

shutter on the substrate surface, in order maintain homogeneity of the target composition. The sputtering conditions are listed in [Table 6](#).

Table 6. Summary of sputtering conditions used for the deposition BaTiO₃ thin films

Substrate :	Pt/Al ₂ O ₃ /SiO ₂ /Si and Nb-SrTiO ₃
Target:	BaTiO ₃ ceramic disc*
RF-power:	10-65 W
Target-substrate spacing:	11 cm (sputtering chamber design)
Sputtering medium:	Ar and O ₂ mixture
Sputtering pressure:	5–30 mTorr
Substrate temperature:	25-800°C
Pre-sputtering duration:	15 min
Sputtering time:	180 min

*Target Dimension: 2.54cm diameter; 0.317cm thickness

Optical emission spectroscopy (OES) was used for understanding the plasma composition, and the substrate etching during BaTiO₃ deposition. Two compact spectrometers, provided with the deposition system, having different spectral resolution were used to monitor the BaTiO₃ sputtering process. The sensitivity of this process control was analyzed with the study of emission intensity of titanium, barium, oxygen, and argon spectral lines and their ratios. All the data were analyzed using “OES Capture” software developed by Plasmionique Inc.

Chemical characterization: Barium and titanium incorporation in the films was determined with X-ray photo-electron spectroscopy (VG Escalab 220i XL). Al K α (1486.6 eV) radiation from a monochromatic X-ray source operating at 400 W was used for the study. The XPS spectra was calibrated using carbon by assigning the binding energy of 284.6 eV to the carbon peak (C1s) position to compensate the shift in the peak position due to charging effects.

Ferroelectric characterization: Ferroelectric switching of the as-deposited films was studied by piezoresponse force microscopy (PFM, Smart SPM1000-AIST-NT Inc.) by *phase-voltage* characteristics at room temperature. Conductive Pt-Ir coated silicon cantilever tips (model HQ:NSC15/Pt from Mikro Masch) with a radius of ~30nm were used for the study.

Thickness measurements: The thickness of BaTiO₃ films was measured with X-ray reflectometry for various deposition time (1, 2, and 4 h, [Figure A1, appendix A](#)), and from the slope of this linear fitted curve, thickness of films deposited for shorter times were extrapolated.

4.3 LOCALIZED RE-SPUTTERING AND SUBSTRATE ETCHING DURING THIN FILM GROWTH

To understand the on-axis and off-axis effects and uniformity of BaTiO₃ deposition with the table top sputtering unit, a 5.08 cm diameter platinized silicon wafer was kept at the center of the substrate holder, without rotation and the deposition was performed at 700°C and 5 mTorr. Now, the RF-power was varied while keeping the oxygen partial pressure (P_O) at 50% and the photographs of the substrate after deposition for about 3 h are depicted in [Figure 29](#). At low RF-power (≤ 10 W or 2 W/cm^2) deposition was observed all over the surface with severe thickness non-uniformity over the whole substrate surface. However, films were uniform at the center over a small area (5 mm×5 mm, blue square). In order to increase the growth rate, the RF-power was increased up to 65W (13 W/cm²). However, due to excessive re-sputtering at the center of the substrate no BaTiO₃ deposition was observed, rather the silicon surface got exposed as the platinum coating was sputtered away. As can be seen from [Figure 29](#), this etching becomes severe with higher RF-power. Such a behavior was not observed in the same sputtering unit during the deposition of Al₂O₃ films with single stoichiometric Al₂O₃ targets, over the entire RF-power levels used for the BaTiO₃ deposition (will be discussed later in [Figure 31](#)).

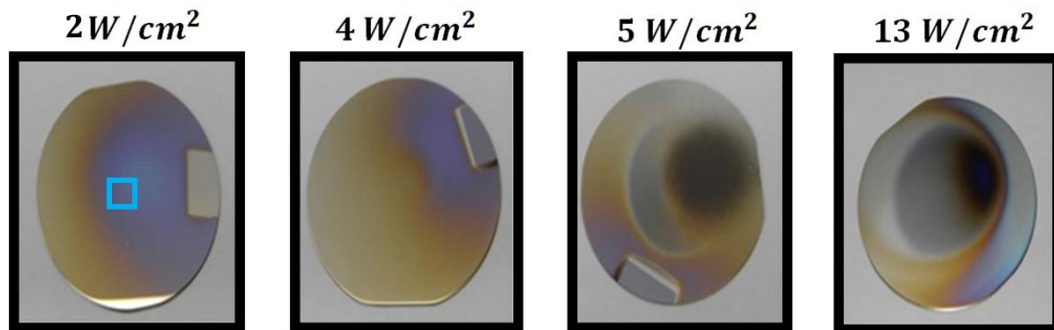


Figure 29. Photograph of the platinized silicon substrate after deposition at 700 °C with various RF power.

Optical emission spectroscopy and *RF-voltage vs. RF-power* characteristics were used to study BaTiO₃ specific substrate etching at the center ([Figure 30](#)). Intensities of the emission lines of barium at 553 nm, titanium at 481 nm, oxygen at 777 nm and argon at 772 nm were obtained

from a plasma used during a deposition process at small pressure (5 mTorr, oxygen partial pressure P_O=50%) and a relative high substrate temperature (700°C).

As can be seen from Figure 30 (a), the normalized intensity ratio of barium and titanium with argon as function of power, showed a slope change in the curve which exactly corresponds to the etching of films (20W, ~ 4W/cm²) discussed before in Figure 29.

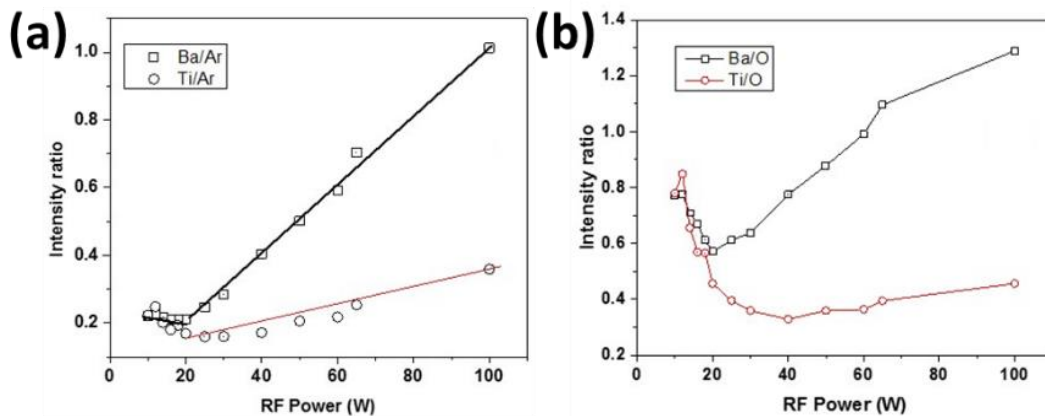


Figure 30. Optical emission spectroscopic results of (a) Variation of the intensity ratio (Ba/Ar) and Ti/Ar as a function of RF-power (b) Intensity ratios of barium and titanium to oxygen.

Similarly, the RF-voltage vs RF-power curve also showed a slope change (Figure 31) in the case of a BaTiO₃ target. In a separate experiment an Al₂O₃ target was used and sputtering was conducted in an identical operating conditions as BaTiO₃. As can be seen from Figure 31, in the case of Al₂O₃, the voltage monotonically increased with power, with little change in the slope. Also, no sputter etching of the substrate was observed in this case. The reason for this BaTiO₃ specific substrate etching has been attributed to the formation of negative oxygen (O⁻) ions.⁹⁰⁻⁹¹ The acceleration of these ions towards the cathode and their impinging on the substrate surface with sufficient energy (>80 to 100 eV) cause re-sputtering of the deposited film. It is well known that the production of negative ions are possible in various degrees in all plasmas processing that contain electronegative gases such as oxygen. However, negative oxygen ions can also be formed as a result of conversion of positive ions, when they interact with elements, like carbon and barium that offers high conversion efficiency. It is worth pointing out that in studies for the production of negative hydrogen ion beams, pure barium has been investigated as an effective source for surface conversion of positive hydrogen ions (H⁺) to negative ions (H⁻).⁹² The high negative ion yield of

barium, despite its high work function, has been attributed also to its high electron density, which could play an important role in this case also. Ohya *et al.*⁹³ explained the possibility of O⁻ ion formation in BaTiO₃ deposition process based on the clue provided by Cuomo *et al.*⁹⁴ According to the authors, for a compound ‘AB’; element B tends to form negative ions if I_A-E_{AB} ≤ 3.4 eV, where I_A is the ionization potential of atom A and E_{AB} is the electron affinity of atom B. The ionization potential of barium and titanium are 5.21 eV and 6.84 eV, respectively. The electron affinity of oxygen is 2.3 eV. In the BaO: TiO₂ system, BaO gives I_A-E_{AB}= 2.91 eV and TiO₂ gives I_A-E_{AB}=4.54eV, suggesting BaO is the prime source of negative oxygen ion production in BaTiO₃.

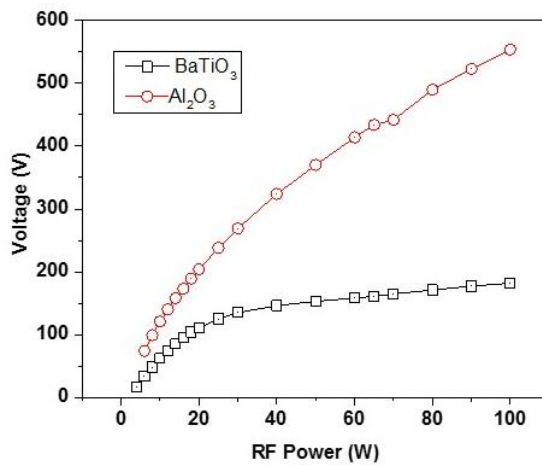


Figure 31. Power-Voltage characteristics during the deposition of thin films in the case of BaTiO₃ and Al₂O₃ targets at 5mTorr and oxygen partial pressure, P_{O₂} = 50 %.

Deposition of stoichiometric BaTiO₃ film requires a delicate balance between the flux of Ti and Ba atoms over the energy and density of negative oxygen ions onto the substrate. The total pressure, the oxygen partial pressure, and RF-power are process parameters that influence this delicate balance. This may be seen in the contrasting behavior of Ba/O and Ti/O intensity ratios with RF-power as illustrated in Figure 30 (b); significant increase in Ba/O intensities after 20W (~ 4W/cm²) where we observed substrate etching. Hence, in the on-axis sputtering of BaTiO₃ with the present system, a power density below 4W/cm² must be considered to realize deposition at the center of the substrate holder. In the following section we will discuss the details of realizing stoichiometric BaTiO₃ on small substrates (5 mm x 5 mm) of silicon platinized (Si/SiO₂/Al₂O₃/Pt(111)) and niobium-doped strontium titanate (Nb-SrTiO₃ (100)) substrates, which were kept at the center of the heater block along the axis with XPS studies.

4.3.1 Stoichiometry of as-deposited BaTiO₃ films

To be far from the substrate etching threshold, a power density around 2W/cm² (10W) was used to avoid or minimize re-sputtering. As can be seen from Figure 31, even at this power the voltage is around 50 V, which may impart a maximum of 50 eV to the O⁻ ion and is still within the limit to cause re-sputtering of the film. So an additional processing parameter, the pressure, was increased to reduce the energy of the O⁻ ion when it touches the substrate surface. The stoichiometry was analyzed with XPS for the films deposited at 10W with an oxygen partial pressure, P_O=50% as a function of processing pressures. General survey scans (Figure 32 (a)) from 1100 eV to 0 eV revealed the presence of titanium, barium, oxygen and carbon at the sample surface. Additional high resolution scans (Figure 32 (b), (c) and (d)) were performed in the selected binding energy ranges for oxygen (O1s), barium (Ba3d) and titanium (Ti2p) to determine the elemental composition.

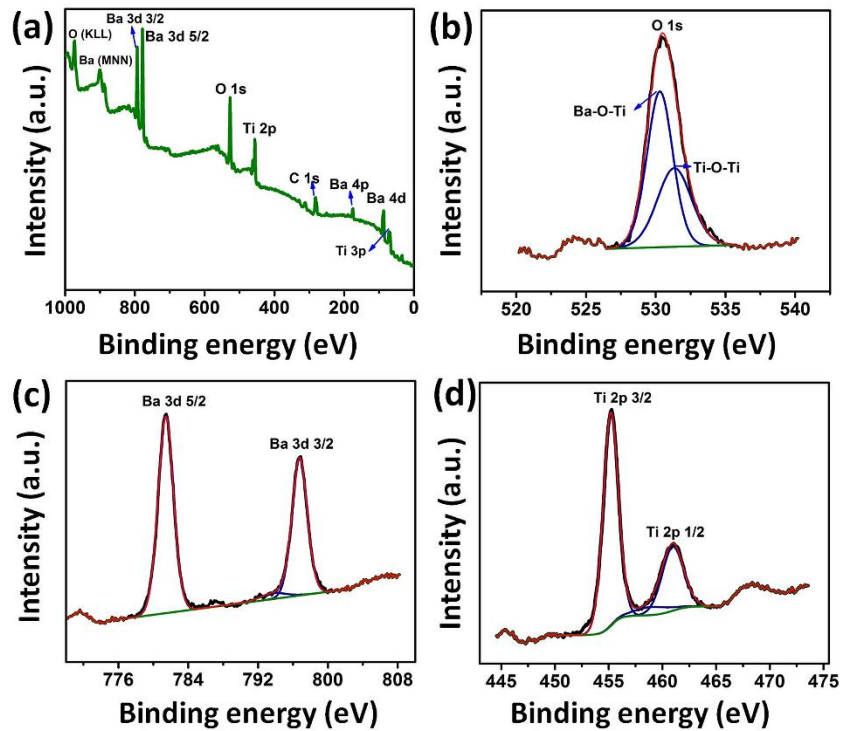


Figure 32. XPS spectra of BaTiO₃ thin film: (a) General survey, (b) O1s, (c) Ba3d, and (d) Ti2p signal

The concentrations determined are based on the peak areas and the relative sensitivity factors. As can be seen in Table 7, at low pressures (5 mTorr), films were non-stoichiometric with

severe barium deficiency and it is improved by increasing the pressure. At about 15 mTorr or more, stoichiometric films with Ba/Ti~1 were obtained on both Nb-SrTiO₃ (100) and Pt/Al₂O₃/SiO₂/Si substrates. This result is consistent with a previous report that discussed Ba/Ti dependence on the processing pressure and the realization of Ba/Ti=1 at high pressures.⁹⁵ This behavior might be due to the higher sputtering yield of barium compared to titanium atoms from the film surface. Sputtering yield, the ratio of number of sputtered atoms to the number of incident ions, mainly depends on the binding energy of the surface atoms, and the energy and angle of incidence of the incident ions. For 0° incidence of Ar⁺ and O⁻ ions having 500eV energy, the sputtering yield of metallic Ti target are 0.54 and 0.29, respectively.⁹⁶ Similarly, for Ba, the sputtering yield is 1.25 for 500eV Ar⁺ ions [<http://www.npl.co.uk/upload/pdf/arsputtertable.pdf>].

Table 7. Atomic concentrations of barium and titanium and the stoichiometry at different processing pressures for the BaTiO₃ films on Pt/Al₂O₃/SiO₂/Si and Nb-SrTiO₃ substrates.

Dep. pressure	Substrate	Barium	Titanium	Oxygen	Ba/Ti
5	Pt/Al ₂ O ₃ /SiO ₂ /Si	16.53 %	23.15 %	60.32	0.71
10	Nb-SrTiO ₃	16.06 %	21.65 %	62.28	0.74
20	Pt/Al ₂ O ₃ /SiO ₂ /Si	17.23 %	15.69 %	67.08	1.09
20	Nb-SrTiO ₃	18.93 %	19.15 %	61.93	0.99

These calculated values may be different for compound target like BaTiO₃ ceramic and films, but we assume that the same trend is maintained. Also, compared to a ceramic target, the sputtering yield of Ba and Ti from the film surface may be higher due to the fact of lower density and evolving material system. However, the sputtering rate of Ba and Ti from the target surface is much higher than that from the film surface, due to more Ar⁺ ions involved in the sputtering than O⁻ ions at low power density. Therefore, Ti-rich deposition at low pressures could be explained by the higher re-sputtering yield of Ba compared to Ti from the film surface. However, as the pressure is increased collisions between O⁻ and gaseous atoms in the chamber occurs more frequently. The energy loss between collisions will reduce the energy of the O⁻ ions that reach the film surface, significantly minimizing re-sputtering from the film/substrate surface. The optimized oxygen partial pressure (P_O=50 %, which corresponds to 10 mTorr) along with the deposition pressure (20 mTorr) and RF-power (10W) resulted the formation of a BaTiO₃ stoichiometric film at a substrate temperature around 700°C.

4.3.2 Summary

BaTiO₃ thin film deposition with an RF-magnetron sputtering technique has been discussed. At high RF-power density ($>4\text{W/cm}^2$), substrate etching has been observed at the center of the substrate and the diameter of this etched circle was around the diameter of the target. However, deposition was possible at regions outside this area. At low power densities, the effect of re-sputtering gradually disappeared at the center of substrate. However, it was observed with XPS measurement, that the film stoichiometry strongly depended on the total pressure, as well as the partial pressure of oxygen. Additional optimization of oxygen partial pressure, $P_o = 0$ to 100% and pressure (5 to 30 mTorr) were required to realize target stoichiometry in the deposited films. With optimization steps, films deposited at 20 mTorr resulted in stoichiometric BaTiO₃ on Nb-SrTiO₃(100) and Pt/Al₂O₃/SiO₂/Si substrates for oxygen partial pressure, $P_o = 50\%$ at 700°C and 2 W/cm² (10W) RF-power.

4.4. FABRICATION OF A Nb:SrTiO₃/BaTiO₃/Pt-TIP HETEROSTRUCTURE

In conventional FTJs the barrier height is modulated by the polarization reversal (to a very small extent, thickness is also modulated due to the piezoelectric effect) and hence the tunneling electroresistance effect (TER effect) allows the formation of two electrical stable states. Typical ON/OFF resistance ratios are around 10². However, with one of the electrodes replaced by a semiconducting material, the barrier width also experiences modulation (to a greater extent by realizing a depletion region in the semiconductor near the ferroelectric/semiconductor interface) along with the barrier height. As the tunneling current exponentially depends on the thickness, the ON/OFF resistance ratio improves further which significantly improves the error margin for highly down-scaled cell-sizes. For the present study, this idea was implemented in Pt/BaTiO₃/Nb:SrTiO₃ heterostructures, in which previous reports has reported an ON/OFF resistance ratio above 10⁴ at room temperature.⁹⁷ Also the readout current densities are very large compared to conventional Fe-RAM, making FTJ highly suitable for high density application by reducing the cell size to the nanometer regime (scalability). Due to these reasons, it was decided to deposit ultra-thin BaTiO₃ films on semiconducting Nb doped SrTiO₃ (Nb:SrTiO₃).

Another important aspect of FTJ is the realization of epitaxial films. The lattice parameter ($a=b=c$) and the thermal expansion of the SrTiO₃, respectively, are 3.905 Å and $11 \times 10^{-6} \text{ K}^{-1}$; close to those of BaTiO₃ ($a=3.993$ Å and $10.7 \times 10^{-6} \text{ K}^{-1}$) which allows for heteroepitaxial growth of the latter on the former up to a critical size far above the tunneling regime. The in-plane compressive stress due to lattice mismatch (~2.3%) enhances the tetragonality of BaTiO₃ and hence the ferroelectricity. However, there is a thickness limit after that epitaxial layer by layer growth significantly changes to island growth due to lattice stress relaxation and grain growth. It has also been reported that the ferroelectric properties are a cooperative phenomenon and also it is accepted that there is a fundamental thickness limit (BaTiO₃ critical thickness = 2.5 nm),⁹⁸ below this value ferroelectricity collapses due to the depolarization of the ferroelectric layer. However demonstrations of ferroelectricity in a nanometer thick films under the appropriate boundary condition has been published in many journals.^{80, 99} The critical thickness to ensure epitaxy of BaTiO₃ on Nb:SrTiO₃ and ferroelectricity in BaTiO₃ are within the tunneling thickness limit to realize an FTJ memory device.

The main challenge for this memory is to achieve a stable polarization state in an ultrathin BaTiO₃ ferroelectric layer and heteroepitaxial growth on Nb:SrTiO₃ substrates by an industry compatible deposition tool. As such, in the present study BaTiO₃ ultrathin films were deposited by RF on-axis magnetron sputtering (using the optimized deposition parameters described above) on Nb:SrTiO₃ (100) substrates and its ferroelectric properties are demonstrated along with the epitaxial growth aspects.

4.4.1 Growth mechanism of BaTiO₃ film on a Nb:SrTiO₃ substrate

The growth of BaTiO₃ thin films by RF-magnetron sputtering starts with the simultaneous impinging of atomic and/or molecular sputtered species from the target on a heated single crystalline, single terminated and atomically flat Nb:SrTiO₃ (100). However, crystallinity, epitaxy and smoothness of the deposited film rely on the nucleation and growth, which depends on the temperature of the substrate surface. To understand this process, BaTiO₃ thin films were deposited for 7 minutes on Nb:SrTiO₃ (100) substrates at different deposition temperatures 500-650°C at a constant pressure (20 mTorr) and a low RF-power (2W/cm²). This time of deposition results in a thickness of 4.3 nm on a Nb:SrTiO₃ substrate at 600°C, a thickness nine times bigger than the unit cell dimension of BaTiO₃, enough to ensure complete coverage on the substrate surface ([Appendix A](#)). The surface morphology of some of these BaTiO₃ films are shown in [Figure 33](#). At a deposition temperature as low as 500°C, a grainy layer uniformly covers the substrate ([Figure 33 \(a\)](#)), with the terrace steps still being visible as in the case of SrTiO₃ prior to deposition ([Figure 28 \(a\)](#)). The heights of the grains on one terrace are of few unit cell dimensions (0.8 to 1.2 nm) and are expected to be integer multiples of the unit cell until lattice relaxation occurs. This surface morphology resembles the pseudo-2D (two dimensional) growth as schematically shown in [Figure 34 \(a\)](#), for the layer by layer (Frank - van der Merwe) growth mode.¹⁰⁰ The average rms roughness of the film surface was very close to that of underlying Nb:SrTiO₃ substrate surface. At high substrate temperature ($\geq 650^{\circ}\text{C}$) the topography ([Figure 33 \(d\)](#)) reveals irregular grains and an rms roughness of around 1 nm, significantly higher than the rms roughness of the Nb:SrTiO₃ substrate. In this case, the roughness increased with thickness and step edges of the substrate were no more visible, suggestive of island (3D) growth (Volmer – Weber) mode or mixed growth (Stranski - Krastanov) mode, as schematically shown in [Figure 34 \(c\)](#) and [4\(d\)](#), respectively.

However, at an intermediate temperature range (550-600°C) the surface morphology showed a very thin, complete BaTiO₃ layer which uniformly covers the substrate surface revealing the step edge of the underlying Nb:SrTiO₃(100) surface and low rms roughness. Such features were more pronounced in the case of a film deposited at 600°C (Figure 33 (c)) and this was expected to be due to the layer by layer (2D) growth discussed before and the rms roughness remained constant as the thickness increased.

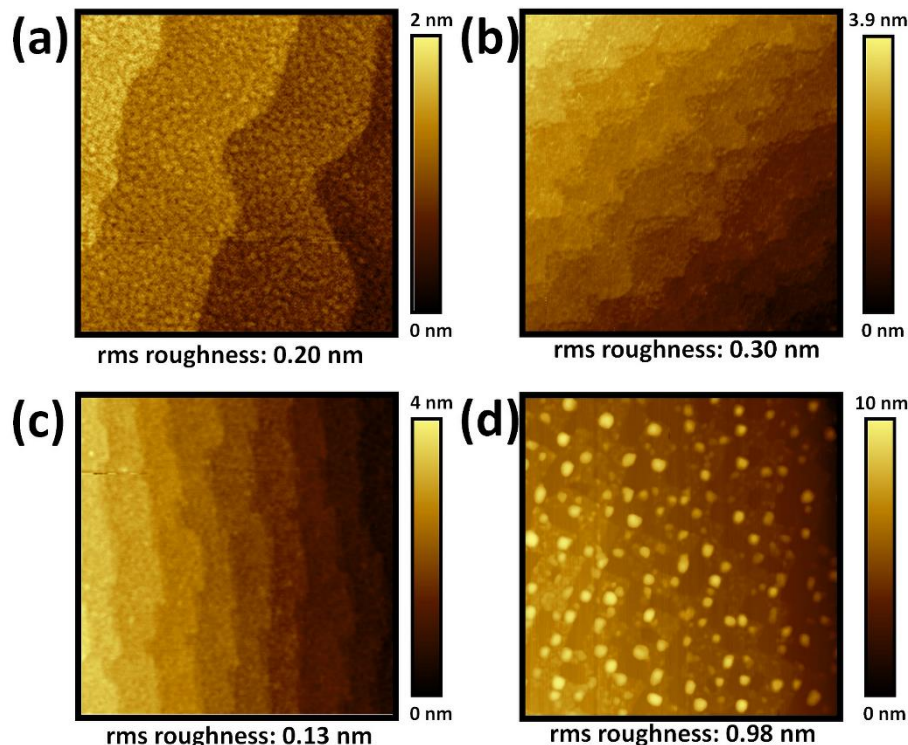


Figure 33. AFM topography images of BaTiO₃ films ($1 \times 1 \mu\text{m}^2$ area) deposited at different temperatures for 7 min on Nb:SrTiO₃ (100) substrates; (a) 500, (b) 550, (c) 600, (d) 650°C

This type of growth is most suitable for hetero-epitaxial growth of BaTiO₃ on Nb:SrTiO₃ (100) substrates with promotion of kinetics of the lateral grain growth i.e. lateral grain boundary motion and the eventual disappearance of grain boundaries (Figure 34 (e)). Comparing Figure 33 (a) and (c), we observe a grain-size difference, lower grain size and roughness for Figure 33 (c). The step density of the substrate surface influences the nucleation as in most cases nucleation generally starts at the step rather than on the terrace. Higher step density (large miscut angle) of the Figure 33 (c) substrate compared the Figure 33 (a) substrate ensures more nucleation sites for the growth and hence smaller and more grains. Therefore, it will be important to have

substrates with identical step-terrace density to reach any meaningful conclusion regarding the nucleation and growth of the deposit when compared for various processing parameters.

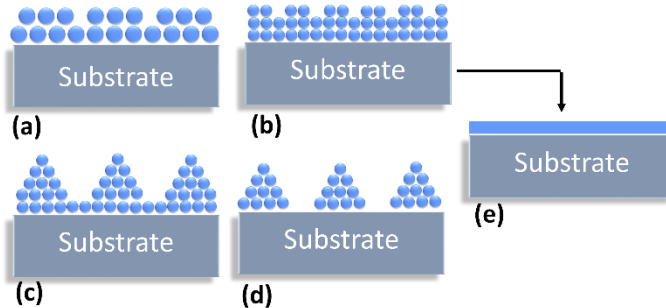


Figure 34. Schematic representation of various experimentally observed growth modes based on the surface morphological features in Figure 33; (a) and (b) incomplete Frank - van der Merwe growth mode, (c) Stranski - Krastanov growth mode, (d) Volmer – Weber growth mode and (e) complete Frank - van der Merwe growth mode.

4.4.2 Ferroelectricity of BaTiO₃ in ultrathin film form

The existence of ferroelectricity in ultra-thin ferroelectric thin films has been experimentally verified down to ultra-low thicknesses and is heavily depended on the quality of the films.¹⁰¹⁻¹⁰² As we obtained crystalline BaTiO₃ films ([appendix A](#)) with an atomically smooth surface due to the layer-by-layer growth, the polarization switching of ultrathin (4.3nm) BaTiO₃ film deposited on Nb:SrTiO₃ substrate at 600°C was investigated by piezoresponse force microscopy (PFM) to monitor the ferroelectric quality of the film. The piezoresponse was obtained by applying an AC voltage along with *DC* bias voltage to the Pt-Ir layer coated silicon cantilever tip with respect to the bottom Nb:SrTiO₃ substrate. The frequency of the applied field was 51 kHz. The amplitude and phase of the AC signal deflected from the cantilever were detected with a lock-in amplifier with various *DC* voltages, which were used to evaluate the piezoresponse and relative orientation of the polarization, respectively. *DC* voltages were applied in sequence (starting $-V_e$ maximum to $+V_e$ maximum and then back with a voltage interval between steps) while monitoring the piezoresponse. For the current case, the voltage started at -10 V ($-V_e$ maximum) increasing by 1V steps to +10V ($+V_e$ maximum) and then back to -10V and the resulting hysteresis loop is shown in [Figure 35](#). As it can be seen from the figure, a film deposited at temperature $\geq 600^\circ\text{C}$, showed a typical hysteresis curve of a ferroelectric material.

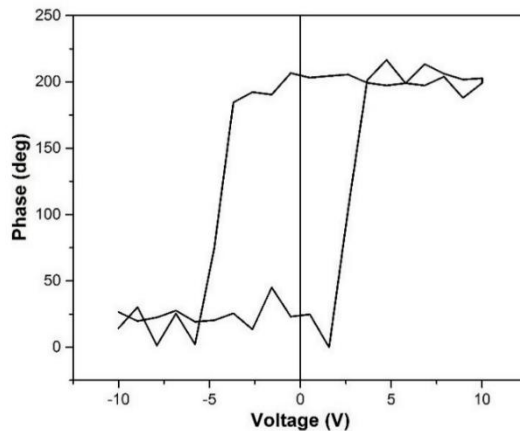


Figure 35. Local phase hysteresis of BaTiO₃ ultra-thin film on Nb:SrTiO₃ substrate showing 180° switching of reversible polarization.

4.4.3 Summary

RF-magnetron sputtering with a compact table top sputtering unit proved to be suitable for the deposition of ultrathin BaTiO₃ ferroelectric films. At high pressure and low RF-power, varying the substrate temperature, pseudo-2D, layer-by-layer and island growth modes were achieved for BaTiO₃ thin films on Nb:SrTiO₃ (100) substrates. Local phase hysteresis of BaTiO₃ ultra-thin film on Nb:SrTiO₃ substrate confirms ferroelectricity. This realization of ferroelectricity in ~4 nm thick BaTiO₃ film on a Nb:SrTiO₃ substrate is encouraging when considering the goal of a ferroelectric tunnel junction in near future where the thickness BaTiO₃ should be < 3nm to exploit tunneling current and ferroelectricity simultaneously.

In this communication, the deposition of crystalline BaTiO₃ was achieved in one single step at relative low substrate temperature (600°C) using a radio-frequency magnetron sputtering technique. However, this substrate temperature is still far to be compatible with the semiconductor industry process. Therefore, it is necessary to search for new ferroelectric and electrode materials.

Chapter 5 Ferroelectric tunnel junction based on Hf_{0.5}Zr_{0.5}O₂

This chapter reports on the on-axis sputtering deposition of Hf_{0.5}Zr_{0.5}O₂ thin films on platinized silicon substrates (Pt/Al₂O₃/SiO₂/Si) and TiN/p-Si substrates. Through the optimization of the deposition parameters, as revealed by X-ray photoelectron spectroscopy, stoichiometric Hf_{0.5}Zr_{0.5}O₂ films were obtained at low sputtering pressure (5 mTorr) and at relative low power density (~4W/cm²). The effect of deposition temperature and film thickness on the ferroelectric properties was investigated by piezoresponse force microscopy.

This chapter also reports the fabrication of two different FTJ memory devices based on CMOS compatible materials: i) nominally symmetric-FTJ (Pt/ Hf_{0.5}Zr_{0.5}O₂/Pt) and ii) asymmetric-FTJ (TiN/ Hf_{0.5}Zr_{0.5}O₂/Pt). Furthermore, two different scanning probe techniques (PFM and C-AFM) were used to demonstrate the ferroelectric behavior of the ultrathin Hf_{0.5}Zr_{0.5}O₂ layer as well as the typical current-voltage characteristics of the FTJ device. An analysis of the metal/ferroelectric interface properties were studied through X-ray photoelectron and UV-visible spectroscopies combined with theoretical models that describe direct tunneling across an electrostatic potential barrier profile with rectangular (Simmon model) and trapezoidal (Brinkman model) shape. Finally, this chapter shows an experimental demonstration of a tunneling electroresistance effect in both FTJ memory devices.

5.1 HAFNIUM-ZIRCONIUM OXIDE FILM

In 2009, Garcia et. al. reported the fabrication of the first FTJ device based on a highly strained BaTiO₃ ultrathin film (1-nm thick), where a giant tunneling electro resistance effect was demonstrated.¹⁷ Since then, a large TER effect has been reported in FTJ devices based on perovskite materials such as BaTiO₃,⁴³ PbTiO₃,⁴⁴ and BiFeO₃.¹⁹ Yet, integrating FTJs with ferroelectric ultrathin films with perovskite structure into the conventional Si-based memory technology remains challenging for many reasons, such as a poor interfacing with silicon (Si), an elevated crystallization temperature, and an electrical degradation caused by a forming gas treatment.⁶⁵

Hafnium zirconium oxide (Hf_{0.5}Zr_{0.5}O₂) is a very promising material for FTJ devices, and could present a solution to overcome the current limitations of the semiconductor memories. Just a few years ago (2011) its ferroelectric behavior in ultrathin film form (layer thickness below 10 nm) was discovered.⁶⁵ This was a surprise since hafnia and zirconia had been studied for more than a century without evidence of polar ordering. In contrast to traditional perovskite materials, Hf_{0.5}Zr_{0.5}O₂ presents several advantages such as a high compatibility with the CMOS process, a low crystallization temperature (~400°C) and an excellent compatibility with TiN electrodes, a favored material for mass production.^{21-22, 69} Owing to the importance of Hf_{0.5}Zr_{0.5}O₂ to the semiconductor industry, this work presents:

- Optimization of the deposition parameters to growth stoichiometric Hf_{0.5}Zr_{0.5}O₂ films.
- Experimental demonstration of the “tunneling electroresistance effect” in an FTJ memory device based on Hf_{0.5}Zr_{0.5}O₂.
- Study of the charge transport mechanisms at the metal/ferroelectric interface of the CMOS compatible FTJ memory.
- Evaluation of the CMOS compatible FTJ memory device.

5. 2 EXPERIMENTAL SECTION

Substrate and surface preparation: Conductive polycrystalline Pt/Al₂O₃/SiO₂/Si, p-Si and TiN/p-Si substrates were used for deposition of Hf_{0.5}Zr_{0.5}O₂. As the actual surface morphology of the as-received Pt/Al₂O₃/SiO₂/Si substrate was found to be depended on the deposition temperature, we used a standard pre-anneal, i.e., 30 min at 650 °C, to stabilize the platinum microstructure before deposition. Further, the as-deposited TiN/P-Si substrates were ultrasonically rinsed with acetone and methanol and dried with nitrogen gas.

Thin film deposition: To optimize the sputtering process, the Hf_{0.5}Zr_{0.5}O₂ thin films were deposited on Pt/Al₂O₃/SiO₂/Si substrates by on-axis RF magnetron sputtering. A polycrystalline Hf_{0.5}Zr_{0.5}O₂ ceramic disc (2.54 cm in diameter and 0.317 cm thickness) was used as a sputtering target. Prior to deposition, the chamber was evacuated at a base pressure of at least 10⁻⁵ Torr using a dry pumping station. The sputtering medium used was a mixture of Ar and O₂ (oxygen partial pressure, P_O=O₂/(Ar+O₂)= 50%) with an operating pressure in the range of 5 – 30 mTorr. The RF power was fixed to 20 Watts on 1” target and the substrate temperature varied from 400 to 650°C

(thermocouple was fixed to a heater block). The target surface was pre-sputtered for 15 minutes prior to all depositions while keeping the shutter on the substrate surface closed. In order to have a better control on the deposition rate, the target substrate distance was kept constant at 110 mm.

Chemical and microstructural: The surface morphology of each film was analyzed by atomic force microscopy, and the atomic percentage of Hf, Zr and O in the Hf_{0.5}Zr_{0.5}O₂ films was determined by X-ray photo-electron spectroscopy (VG Escalab 220i XL). The energies and intensities of the photoelectron peaks were analyzed using the “*CasaXPS*” processing software. Film thicknesses were determined by X-ray reflectivity (XRR) and the software Gen X. For films thicker than 5 nm, the structural properties were studied by high-resolution X-ray diffraction (XRD) in grazing incidence mode using a Philips X’Pert MRD four-circle diffractometer with a Cu $\text{K}\alpha$ source.

Electronic characterization: The indirect bandgap (E_g) of a thick Hf_{0.5}Zr_{0.5}O₂ layer grown on Si quartz (0001) was calculated with the Tauc plot method using the transmission spectra obtained from a Perkin-Elmer UV/VIS spectrometer. X-ray photoelectron spectroscopy was employed to determine the band alignment of the Hf_{0.5}Zr_{0.5}O₂ film with the TiN and Pt substrates, it recorded the shallow core level, the valence band spectra and the Fermi energies. All high resolution spectra were collected in the constant pass energy (20 eV) mode. The binding energy scale was calibrated using a pure gold standard sample, and setting Au 4f7/2 at a binding energy of 84.00eV ([Appendix A](#)).

Ferroelectric and electrical characterization: Ferroelectric switching of the films was studied by piezoresponse force microscopy (PFM). Conductive Pt-Ir coated silicon cantilever tips (radius of \sim 30nm) were used for PFM imaging and polarization studies. Local piezoelectric hysteresis loops were measured at a fixed location on the film surface as a function of DC switching bias. Nanoscale electrical measurements were performed in conductive AFM mode. For the electrical characterization, platinum top electrodes (thickness = 30 nm) were deposited using a DC sputtering, through a shadow mask having a hole diameter of 300 μm ([Appendix B](#)). After top electrode deposition, post annealing was performed for ten minutes at 450°C in an N₂ atmosphere in order to fully crystallize the film and to improve the adherence on surface of the ferroelectric layer.

5.3 OPTIMIZATION OF THE Hf_{0.5}Zr_{0.5}O₂ DEPOSITION PARAMETERS

5.3.1 Microstructural characterization

The surface morphology of Hf_{0.5}Zr_{0.5}O₂ films on platinum substrates films was analyzed by atomic force microscopy, as shown in Figure 36. Polycrystalline granular features were observed on the platinum surface with an rms of ~1.4 nm (Figure 36 (a)). Films deposited at 450°C and 500°C showed an rms roughness of ~1.3 and 1.5 nm (Figure 36 (b) and (c)), respectively, while the surface roughness increased to 1.6 and 1.8 nm (Figure 36 (d) and (e)), at higher deposition temperatures (600°C and 650°C, respectively). Homogenous deposition of fine grains of Hf_{0.5}Zr_{0.5}O₂ was observed over the entire platinum surface in the investigated temperature range 450–600°C. The deposited layers showed similar features as the underlying platinum layer. As the temperature increased to 650°C, substantial grain growth of Hf_{0.5}Zr_{0.5}O₂ was observed and the surface features of the platinum became masked.

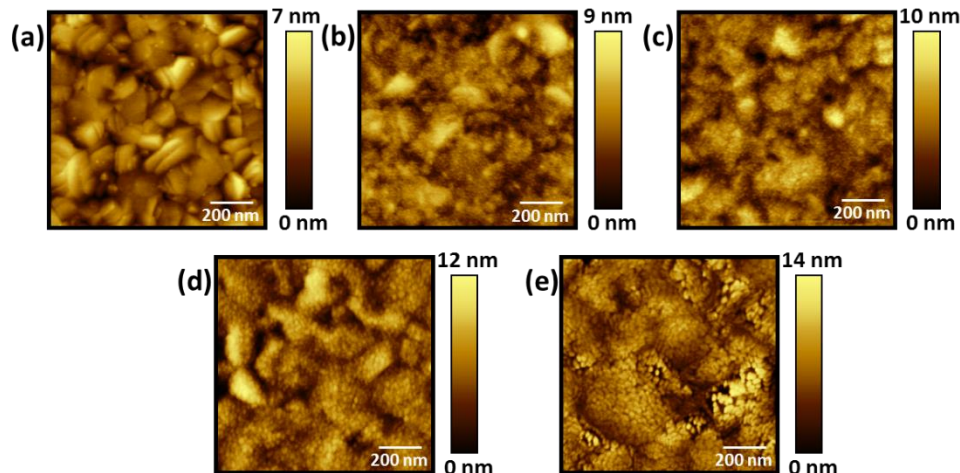


Figure 36. AFM topography images ($1 \times 1 \mu\text{m}^2$) of: (a) surface morphology of platinum substrate and surface morphology of as deposited Hf_{0.5}Zr_{0.5}O₂ film at different substrate temperatures (b) 450°C, (c) 500°C, (d) 600°C and (e) 650°C

5.3.2 Chemical characterization

The stoichiometry of the RF-magnetron sputtered Hf_{0.5}Zr_{0.5}O₂ thin films on platinized silicon substrates was studied as a function of deposition temperature and pressure by X-ray photoelectron spectroscopy. Survey scans (Figure 37 (a)) from 1200 eV to 0 eV revealed the presence of hafnium, zirconium, oxygen and carbon at the sample surface for the films deposited at 750°C and 5mTorr. Additional high resolution scans (Figure 37(b) and (c)) were performed in the selected binding energy ranges for oxygen (O1s), carbon (C1s), zirconium (Zr3d) and hafnium

(Hf4f) to determine the elemental composition. The atomic concentrations determined are based on the peak areas and the relative sensitivity factors. At small sputtering pressure (5 mTorr) with an oxygen argon mixing ratio of 50% (2 sccm O₂ and 2 sccm Ar) films deposited at substrate temperature in the range 400-750°C were stoichiometric (Hf/Zr~1). Also stoichiometry was almost independent of the deposition pressure in the deposition pressure range of 5 to 20 mTorr.

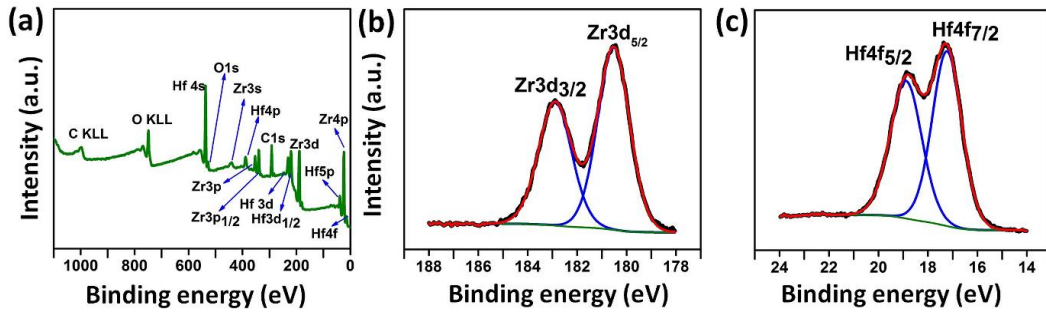


Figure 37. (a) XPS spectra survey of Hf_{0.5}Zr_{0.5}O₂ films on platinized silicon wafers, (b) zirconium (Zr_{3d}) and (c) hafnium (Hf_{4f}) XPS signals.

5.3.3 Ferroelectricity as a function of deposition temperature

In order to determine the optimal deposition temperature for stabilizing the ferroelectric phase of Hf_{0.5}Zr_{0.5}O₂ films, the substrate temperature was varied. Prior to ferroelectric characterization, thickness measurements were performed using X-ray reflectometry (Figure 38). The presence of multiple oscillations indicated a smooth surface (rms ~ 1.4 nm); the thickness was found to be independent of deposition temperature. An average thickness of ~8 nm was calculated for the films grown in the temperature range of 425-500°C.

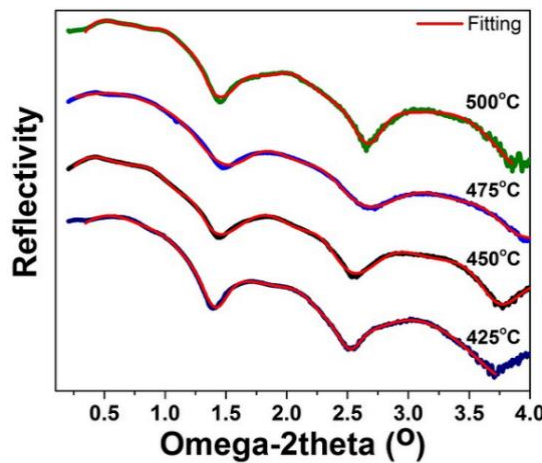


Figure 38. X-ray reflectivity data of the Hf_{0.5}Zr_{0.5}O₂ layer deposited on p-Si substrates at different temperatures.

The effect of the deposition temperature of $\text{Hf}_{0.5}\text{Zr}_{0.5}\text{O}_2$ on ferroelectricity is presented in [Figure 39](#). Polarization switching of 8 nm-thick films was investigated by PFM. In general, $\text{Hf}_{0.5}\text{Zr}_{0.5}\text{O}_2$ films grown at a temperature above 425°C showed typical hysteresis curves, which indicates the ferroelectric character of the material. However, films grown at 400°C did not show hysteresis loops suggesting non-ferroelectric character, due to their amorphous nature (not shown). An increment on the coercive field was observed as the deposition temperature decreased (from 500 to 425°C), this behavior was associated with a decrease of film crystallinity, which makes it harder for the ferroelectric domains to switch. [Figure 39](#) also shows out-of-plane PFM phase images to demonstrate polarization reversal (180° phase contrast). A square region ($1 \mu\text{m} \times 1 \mu\text{m}$) of films produced at 500°C and 475°C was switched downwards by scanning the film surface with a tip biased with a negative voltage ($V_{\text{Tip}} = -V$) exceeding the coercive voltage of the film. Then, polarization within an area of $0.5 \mu\text{m} \times 0.5 \mu\text{m}$ in the center was switched upwards by applying a negative bias ($V_{\text{Tip}} = +V$). For those films produced at 450°C and 425°C, the same procedure was used but using opposite polarity.

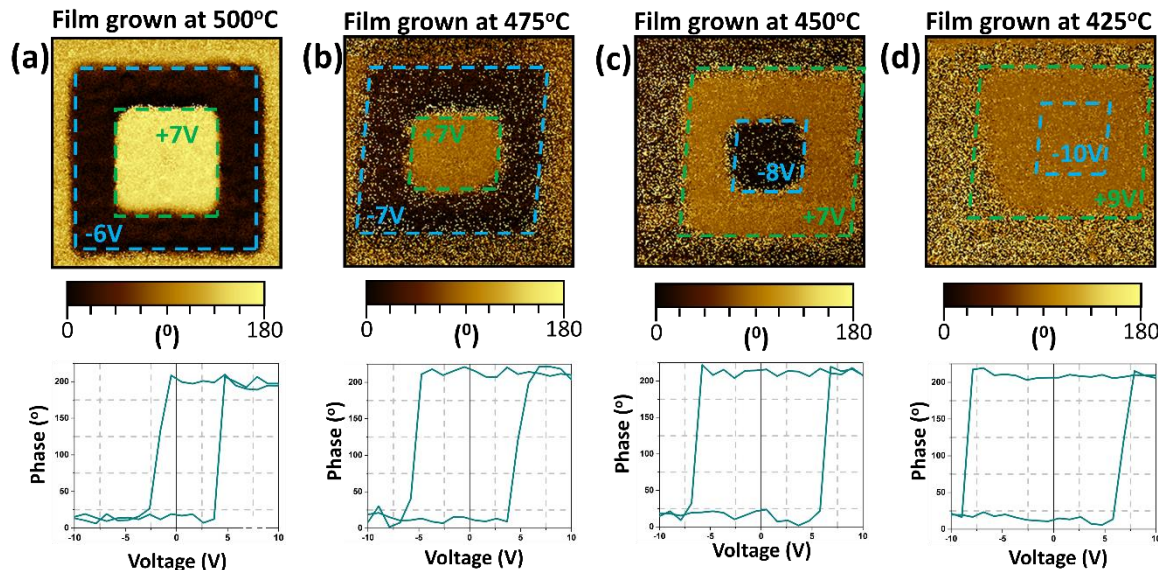


Figure 39. Piezo-response Force Microscopy phase images and local hysteresis curves of $\text{Hf}_{0.5}\text{Zr}_{0.5}\text{O}_2$ films grown on $\text{Pt}/\text{Al}_2\text{O}_3/\text{SiO}_2/\text{Si}$ substrates at different temperatures: (a) 500 °C, (b) 475 °C, (c) 450 °C and (d) 425°C.

Films grown at 500°C, 475°C, and 450°C were able to go through a full cycle of ferroelectric polarization switching ([Figure 39](#) (a), (b) and (c), respectively). Furthermore, films produced at temperatures around of 475°C and 450°C present small regions (Yellow spots, [Figure 39](#)) inside a

pre-poled area. These can be explained due to issues related to ferroelectric retention. At 425°C (Figure 39 (d)) switching back of the ferroelectric domains is hardly visible in the center of the PFM phase image, even after increasing the *DC* bias. Overall, the ferroelectric phase of $\text{Hf}_{0.5}\text{Zr}_{0.5}\text{O}_2$ occurred at a deposition temperature of 450°C, which is lower than that temperature employed for conventional perovskite materials (>600°C).^{6, 103} In terms of device application this is an advantage for CMOS compatibility because of the relative low thermal budget required for $\text{Hf}_{0.5}\text{Zr}_{0.5}\text{O}_2$ formation.²⁵

5.3.4 Ferroelectricity as a function of film thickness

By varying the deposition time (40–200 min) the thickness of the films could be adjusted. Prior to ferroelectric characterization of the sputtered films, the thickness was determined by X-ray reflectivity (Figure 40 (a)). The observed linear relationship between thickness and deposition time shows a deposition rate of ~4 nm of thickness per hour (Figure 40 (b)) at a substrate temperature of 450°C, a very low but not untypical deposition rate for long transport distances. This linear trend allows to predict the deposition time necessary to synthesize nanometer thick coatings.

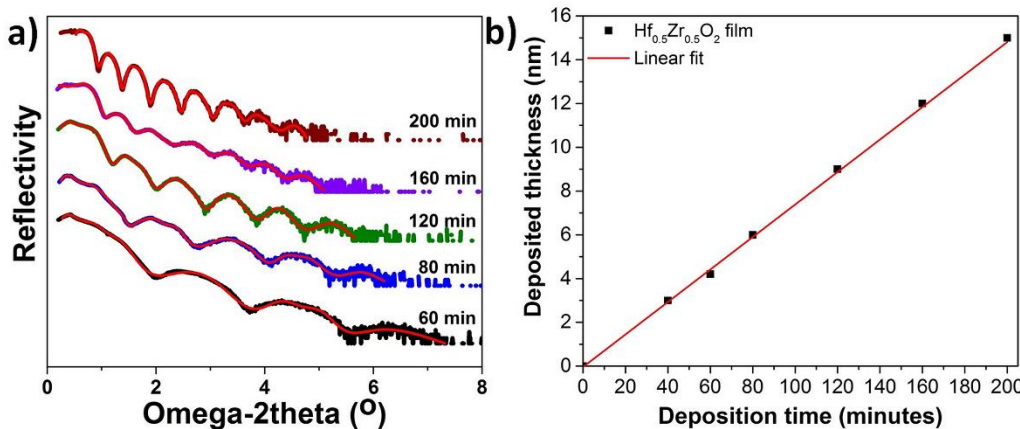


Figure 40. (a) X-ray reflectivity data of the $\text{Hf}_{0.5}\text{Zr}_{0.5}\text{O}_2$ layer grown on p-Si substrates as a function of deposition time, and (b) Converted thickness results.

The dependence of ferroelectricity on the thickness is presented in Figure 41. PFM reveals a local hysteresis curve with a large coercive field for a relatively thick $\text{Hf}_{0.5}\text{Zr}_{0.5}\text{O}_2$ film (16 nm, Figure 41(a)). This result indicates ferroelectricity degrading due to the increasing portion of the non-ferroelectric monoclinic phase (P21/c).^{21, 24} 16 nm-thick films showed a phase contrast PFM

image with some issues related to the switching back the ferroelectric domains, as the region at the center (small square) did not show changes. We would like to point out that, due to generally ill-defined tip-sample interface, it is impossible to translate the tip voltage into a local electric field. For those films with a lower thicknesses (6–3 nm) we clearly observe ferroelectricity (Figure 41(b) and (c)), which is attributed to the formation of the non-centrosymmetric orthorhombic phase ($\text{Pbc}21$). Below 10 nm, this ferroelectric phase is induced by tensile strain from the coalescence of the nucleating small grains.^{21-22, 24} A local hysteresis curve close to the detectable signal to noise ratio, as well as a PFM map in which is difficult to observe the PFM phase contrast, are presented in Figure 41 (d), it suggests that the ferroelectricity in $\text{Hf}_{0.5}\text{Zr}_{0.5}\text{O}_2$ disappeared for a film thickness equal to two unit cells (~1 nm), assuming that the ferroelectricity of any film is influenced by the crystallographic orientation of the substrate. We would like to point out that this is a negative evidence, so that the lack of observable polarization reversal does not necessarily imply a loss of ferroelectricity.

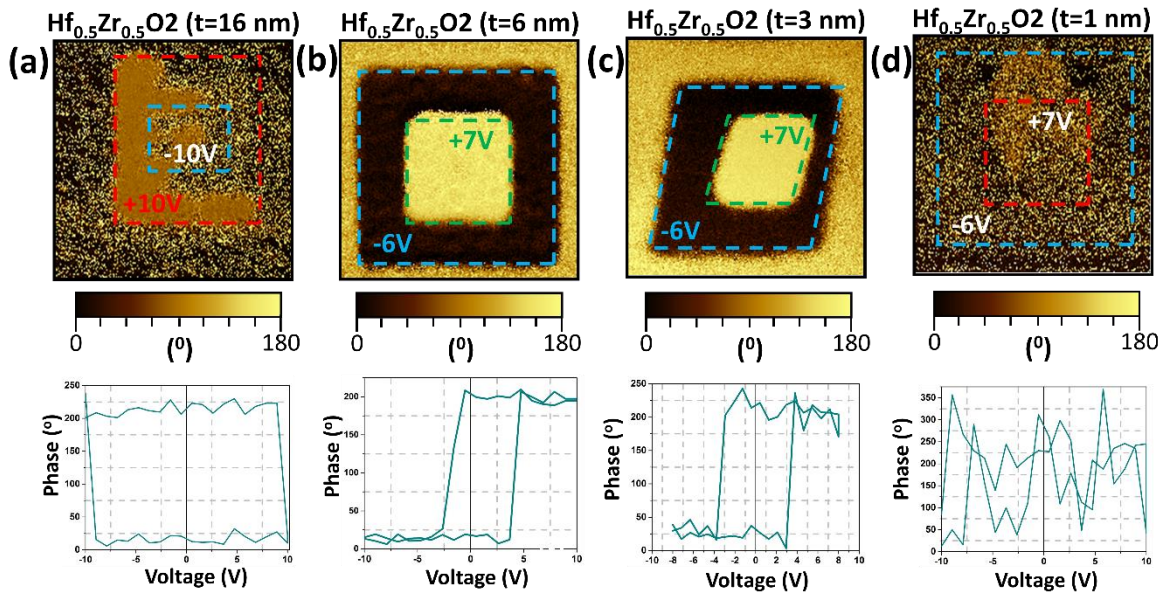


Figure 41. Piezo-response force microscopy phase images and local hysteresis curves of $\text{Hf}_{0.5}\text{Zr}_{0.5}\text{O}_2$ films at different thicknesses: (a) 16 nm, (b) 6 nm, (c) 3 nm and (d) ~1 nm (two unit cells).

To study the real effect of film thickness without taking into consideration (111) crystal orientation of the underlying platinum substrate, a two unit cell-thick $\text{Hf}_{0.5}\text{Zr}_{0.5}\text{O}_2$ film was deposited on a conductive TiN/(100)p-Si substrate. PFM images taken from the film are presented in Figure 42. The phase image consists of well-defined bright/dark contrast regions, which

correspond to domain patterns with 180° phase shifts between domains with opposite polarization, imprinted by applying an external bias through an AFM tip. The voltage-dependent square hysteresis PFM phase loops and the hysteresis amplitude loop exhibited the typical characteristics of ferroelectric polarization switching. The present results showed the feasibility of a stable polarization in an ultrathin $\text{Hf}_{0.5}\text{Zr}_{0.5}\text{O}_2$ layer, which is one of the crucial conditions for quantum-mechanical tunneling in a ferroelectric tunnel junction memory. This memory type offers the potential to overcome the limitations of conventional semiconductor memory devices that are based on charge storage.^{14-15, 20}

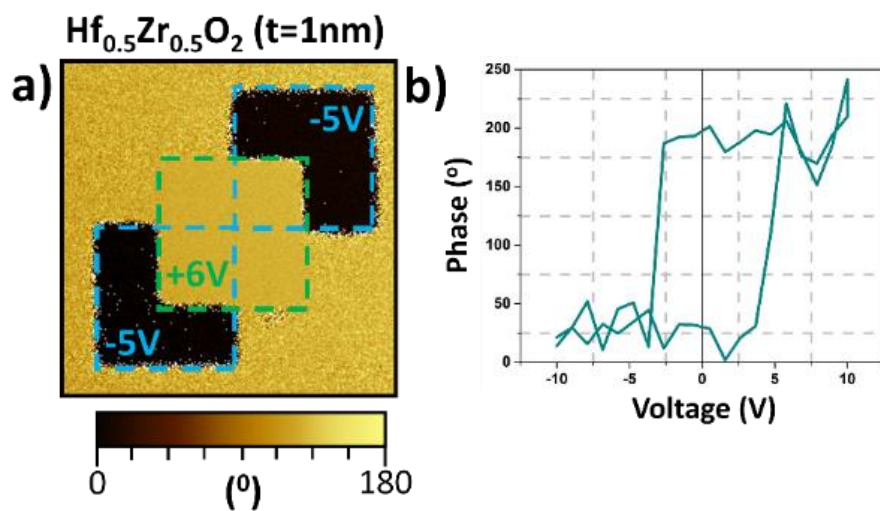


Figure 42. (a) Piezo-response force microscopy phase images and (b) Local hysteresis curves of two unit cells $\text{Hf}_{0.5}\text{Zr}_{0.5}\text{O}_2$ thick film grown on $\text{TiN}/p\text{-Si}$ substrate.

5.3.5 Summary

Ferroelectric $\text{Hf}_{0.5}\text{Zr}_{0.5}\text{O}_2$ films were deposited using a compact table-top RF magnetron sputtering system. Stabilization of the ferroelectric phase was best achieved at a deposition temperature of $\sim 450^\circ\text{C}$, which is relevant for CMOS compatibility. The presence of ferroelectricity was observed in $\text{Hf}_{0.5}\text{Zr}_{0.5}\text{O}_2$ in ultrathin film form. Therefore, the combination of a CMOS compatible deposition process with ferroelectric properties in ultrathin form makes of $\text{Hf}_{0.5}\text{Zr}_{0.5}\text{O}_2$ an ideal material for the fabrication of ultrafast and nonvolatile memory devices such as ferroelectric tunnel junction memory.

5.4 NOMINALLY SYMMETRIC FTJ MEMORY DEVICE (Pt/Hf_{0.5}Zr_{0.5}O₂/Pt)

This section reports on the fabrication of a nominally symmetric ferroelectric tunnel junction based on a CMOS compatible ultrathin Hf_{0.5}Zr_{0.5}O₂ tunnel barrier using the deposition parameters determined in [section 5.3](#).

5.4.1 Fabrication of the nominally symmetric FTJ memory device

An Hf_{0.5}Zr_{0.5}O₂ layer was deposited on a polycrystalline Pt substrate. The Pt/ Hf_{0.5}Zr_{0.5}O₂ heterostructure was grown via on-axis radio-frequency magnetron sputtering at 450°C, using a deposition pressure of 5 mTorr (2 sccm O₂ and 2 sccm Ar) for an RF power of 20 Watts on a 1-inch target. Pt top electrode was deposited using *DC* sputtering through a shadow mask consisting of an array of 300 μm diameter holes ([Appendix B](#)). The deposition parameters are listed in [Table 8](#).

Table 8. Summary of sputtering conditions used for the fabrication of the symmetric FTJ memory device.

Film:	Hf _{0.5} Zr _{0.5} O ₂	Pt
Target:	Hf _{0.5} Zr _{0.5} O ₂ ¹	Pt ²
Substrate:	Pt	Hf _{0.5} Zr _{0.5} O ₂ /Pt
Power density:	~4 W/cm ²	~5 W/cm ²
Target-substrate spacing:	11 cm	11 cm
Sputtering medium: ³	Ar and O ₂ mixture ⁴	Ar
Sputtering pressure:	5 mTorr	5 mTorr
Substrate temperature:	450°C (displayed)	25°C
Pre-sputtering duration:	15 min	15 min
Deposition time:	45 min	3 min

¹Target dimensions: Ceramic disc (2.54cm in diameter; 0.317cm in thickness)

²Target dimensions: Metallic disc (2.54cm in diameter; 0.158cm in thickness)

³Gass purity: Argon (99.998% pure) and Oxygen (99.993%)

⁴Oxygen partial pressure: $P_O = O_2/(Ar + O_2) = 50\%$

Targets: Hf_{0.5}Zr_{0.5}O₂ ceramic disc (99.9% pure) and Pt metallic disc (99.9% pure)

In an FTJ, the tunneling current that flows through the ferroelectric barrier depends highly on the barrier thickness.¹⁴ Therefore, it is crucial to precisely determine the layer thickness of our films. In the present work, the layer thicknesses were found to be 2.8 nm for the film used in fabrication of the FTJ ([Figure 43](#) (a)). The presence of multiple oscillation in the XRR curves indicates a smooth surface (roughness rms= 1.2 nm). A density of 8.40 g/cm³ was obtained for the 2.8nm thick film, this value is comparable with those reported in literature (8.34 g/cm³).¹⁰⁴

The present nominally symmetric FTJ cell memory is 300 μm in diameter, the platinum bottom electrode has a layer thickness of 100 nm, the ultrathin $\text{Hf}_{0.5}\text{Zr}_{0.5}\text{O}_2$ layer has a thickness of 2.8 nm, and the top electrode has a layer thickness of 30 nm (Figure 43 (b), appendix B).

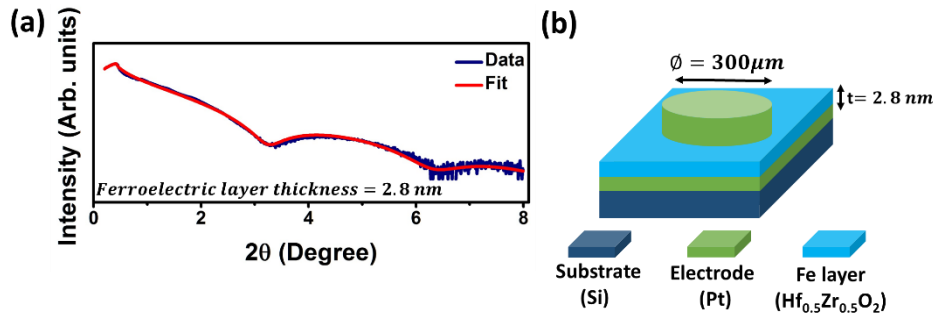


Figure 43. (a) X-ray reflectivity curve recorded on a $\text{Hf}_{0.5}\text{Zr}_{0.5}\text{O}_2$ film (blue curve) and (b) Schematic representation of the nominally symmetric FTJ memory prototype.

5.4.2 Ferroelectric characterization of the nominally symmetric FTJ device

Contrary to conventional ferroelectric memories (Fe-RAM), the scalability of the FTJs is not limited by its readout process, since the tunneling current in an FTJ does not depend on the amount of the stored charges and can be probed in a non-destructive way, allowing the fabrication of denser semiconductor memories.¹⁵ However, one of the main challenges is to achieve a stable polarization in the ultrathin barrier layer.¹⁵ In that sense, ferroelectric characterization is crucial for these ultrathin films. In this work, the ferroelectric properties of $\text{Hf}_{0.5}\text{Zr}_{0.5}\text{O}_2$ films were investigated by PFM. The local piezoresponse of $\text{Hf}_{0.5}\text{Zr}_{0.5}\text{O}_2$ ultrathin film was measured at room temperature as a function of the direct voltage between the top and bottom electrodes. A clear hysteresis was observed in both phase and amplitude signals (Figure 44 (a) and (b)). Both signals were acquired away from the contact resonance frequency of the cantilever ($f_{\text{PFM}}=51\text{kHz}$, $f_{\text{Cantiliver}}=600\text{kHz}$) as a function of voltage, which was applied to the conductive tip while the bottom electrode remained grounded. The ferroelectric behavior presented in Figure 44 is attributed to the formation of the non-centrosymmetric orthorhombic phase ($\text{Pbc}21$).²⁴ The values of the coercive voltages creating the downward and upward polarizations are +1.9 V and -1.9V, respectively. Different regions of the bare surface of $\text{Hf}_{0.5}\text{Zr}_{0.5}\text{O}_2$ film were poled by a constant voltage to the tip while scanning the film's surface. The resulting PFM phase image, presented in Figure 44 (c), shows a phase contrast of $\sim 180^\circ$ between the square domains written at -3V and

+3V, qualitatively, this demonstrates the appearance of the upward and downward polarization states, respectively. The unpoled region outside the larger domains correspond to the sample virgin state, which exhibits a spontaneous downward polarization. The amplitude image ([Figure 44\(d\)](#)) reveals narrow dark lines that are attributed to domain walls.¹⁰⁵ The PFM measurements presented here attest to the stable polarization in the ultrathin Hf_{0.5}Zr_{0.5}O₂ layer, and therefore fulfill a crucial requirement for quantum-mechanical tunneling in an FTJ memory.

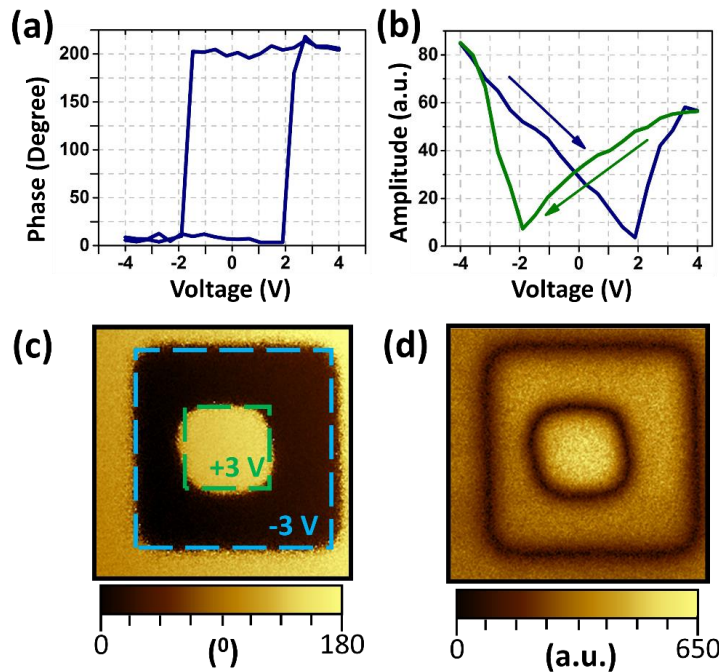


Figure 44. PFM measurements obtained on the 2.8 nm thick Hf_{0.5}Zr_{0.5}O₂ film showing (a) the phase signal of the local hysteresis loop, (b) the corresponding amplitude signal, (c) a PFM phase image (1.5 μ m \times 1.5 μ m) and (d) the corresponding amplitude image.

5.4.3 Electronic properties of the nominally symmetric FTJ memory device

To verify if Hf_{0.5}Zr_{0.5}O₂ films are suitable for FTJ devices, the optimized potential barrier profile has to be studied. For this purpose, optical characterization by UV/visible transmission spectroscopy and XPS band structure analysis were found complementary in identifying a suitable ferroelectric material.

The indirect band gap (E_g) was estimated from the Tauc plot method, using $(ahv)^2$ versus (hv) plots, by extrapolating the linear portion of the absorption curve to the x-axis, where the

absorption coefficient becomes zero (Figure 45). The calculated band gap value was 5.06 eV for an Hf_{0.5}Zr_{0.5}O₂ film grown on Si-quartz substrate (film thickness equal to 47 nm).

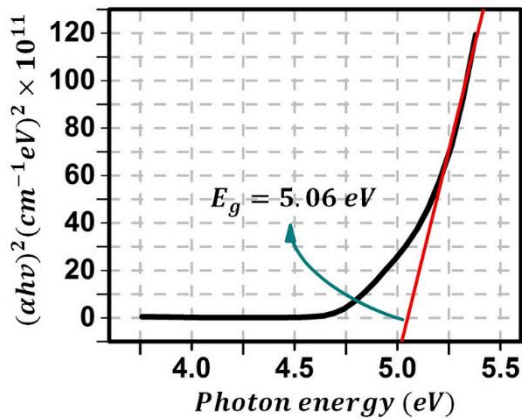


Figure 45. Energy band gap of an Hf_{0.5}Zr_{0.5}O₂ sample.

To gain quantitative information on the material's electronic properties, the band line-up was characterized at the Pt/ Hf_{0.5}Zr_{0.5}O₂ interface using a Kraut procedure.¹⁰⁶⁻¹⁰⁷ In this method, XPS spectra of both (core levels and valence bands) were simultaneously recorded and used to determine the valence band offset first. The valence band maximum (VBM) of Hf_{0.5}Zr_{0.5}O₂ as well as the Fermi level (E_F) of Pt were determined by extrapolating the leading edge to the baseline and finding the intersection point. The binding energy difference between the shallow core peaks (Pt4f and Hf4f), E_F and the VBM were measured and referenced with core level binding energies of ultrathin heterostructures in order to calculate the valence band offset (VBO), according to

$$VBO = (E_{Pt4f} - E_F)_{pt} - (E_{Hf4f} - VBM)_{HZO} - (E_{Pt4f} - E_{Hf4f})_{HZO/Pt} \quad (14)$$

The energy separation between Pt4f centroid and the leading E_F was estimated to 70.5 ± 0.05 eV for a clean, thick Pt layer, as shown in Figure 46 (a). Similarly, the energy difference between the Hf4f centroid and the VBM for Hf_{0.5}Zr_{0.5}O₂ thick film was estimated to 14.3 ± 0.05 eV (Figure 46 (b)). The binding energy difference between Pt4f and Hf4f core levels was calculated to be 53.5 ± 0.05 eV (Figure 46 (c)) for an XPS spectrum measured on the Hf_{0.5}Zr_{0.5}O₂ (2.8nm)/Pt heterostructure. Substituting these values in Eq. 14, a VBO of 2.70 ± 0.05 eV was obtained.

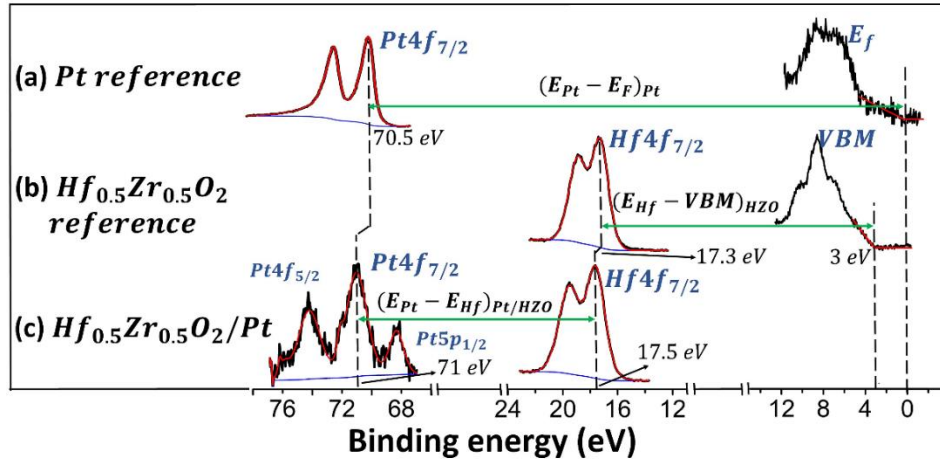


Figure 46. XPS spectra of a (a) bulk Pt, (b) thick Hf_{0.5}Zr_{0.5}O₂ layer, and (c) Hf_{0.5}Zr_{0.5}O₂/Pt interface.

Knowing E_g values from the UV/visible measurements (5.06 eV) and the VBO from the XPS analysis (2.70 eV), the conduction band offset or potential step height (φ) can be estimated using.

$$\varphi_{1(2)} = E_g - VBO_{Pt/HZO} \quad (15)$$

A value of 2.36 ± 0.07 eV was obtained. The electronic band diagram of the Figure 47 corresponds to the Pt/Hf_{0.5}Zr_{0.5}O₂/Pt heterostructure for a voltage equal to zero (rectangular shape). From the above PFM analysis it is known that obtained potential step height correspond to a ferroelectric film with a spontaneous downward polarization.

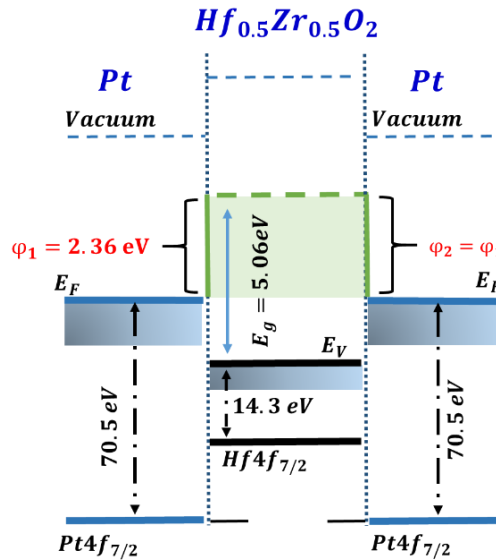


Figure 47. Schematic diagram of the potential energy profile for the Pt/Hf_{0.5}Zr_{0.5}O₂/Pt heterostructure.

5.4.4 Tunneling electroresistance effect in the nominally symmetric FTJ memory device

While it is commonly accepted that in order to have a sizable TER effect, it is mandatory to have asymmetric FTJs (Junction that involves different electrodes),¹⁶ recent theoretical⁴² and experimental⁴¹ results showed a large TER effect in nominally symmetric FTJs (Junction that involves similar electrodes). Moreover, some drawbacks concerning retention time, switching and polarization imprint in asymmetric FTJs have been reported.⁴² Thus we focused this work on an FTJ fabricated by covering with a Pt top electrode the 2.8 nm-thick $\text{Hf}_{0.5}\text{Zr}_{0.5}\text{O}_2$ film deposited on a Pt layer. The resulting nominally symmetric-FTJ was characterized by measuring its hysteretic I - V curve. Voltage sweeps were applied to the top electrode via a conductive AFM tip. The bottom electrode was grounded and a compliance current of 100 nA was set during the measurements to avoid soft dielectric breakdown of the junctions (Figure 48 (b) inset). A typical I - V curve is shown in Figure 48 (a). It displays a hysteretic behavior characterized by two different resistance states: an initial high-resistance state (HRS) and a low-resistance state (LRS). The existence of two clearly defined resistance states suggests a TER effect.¹⁰⁵

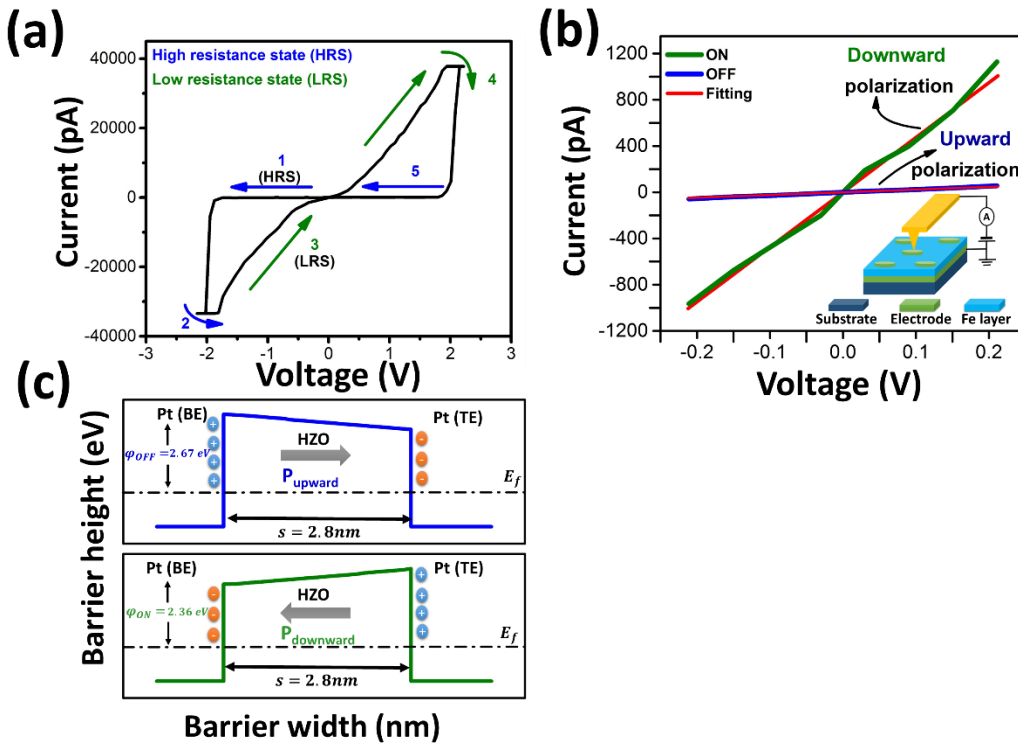


Figure 48. (a) A typical current-voltage curve for a Pt/ $\text{Hf}_{0.5}\text{Zr}_{0.5}\text{O}_2$ /Pt FTJ, (b) Zoom in at low voltages of the current-voltage curves for two opposite polarization directions in the 2.8 nm-thick $\text{Hf}_{0.5}\text{Zr}_{0.5}\text{O}_2$ film. Red lines, fitting of the experimental data; the inset is a schematic of the C-AFM geometry. (c) Electronic potential profile ($V \neq 0$).

To confirm that the electric switching observed by C-AFM is due to the TER effect rather than another resistive switching mechanism, the electronic structure depicted in [Figure 47](#) was correlated to the transport properties of the Pt/ Hf_{0.5}Zr_{0.5}O₂/Pt tunnel junction,⁴¹ assuming direct tunneling across a rectangular shape electronic profile.¹⁰⁸ This model, known as the Simmons model,¹⁰⁸ is based on Fermi-Dirac statistics and WKB approximation, assuming a low voltage (V) and a barrier width (s). The tunneling current density (J) through a barrier at low voltage range, is given by

$$J = \left[\frac{3(2m\varphi)^{\frac{1}{2}}}{2s} \right] \left(\frac{e}{h} \right)^2 V \times \exp \left[-\frac{(4\pi s)}{h} (2m\varphi)^{\frac{1}{2}} \right] \quad (16)$$

Where “ m ” is the effective electron mass, “ φ ” is the electronic potential barrier height, “ h ” is the Plank constant and “ e ” is the electron charge. The experimental I - V curve for the “ON” state (downward polarization, [Figure 48](#) (b)) was fitted using the experimentally-determined parameters such as electronic potential barrier height ($\varphi=2.36$ eV), the barrier width ($s = 2.8$ nm) and adding only the scaling factor, which was assumed to be the same for both states, following the method described in the literature.^{43, 105} Then, using the same scaling factor, the same barrier width (s) and [Eq.16](#), the I - V curve for the “OFF” state ([Figure 48](#) (b)) was fitted to obtain the potential step barrier height for that state ($\varphi=2.67$ eV). The change in barrier height is ($\Delta\varphi$) ~13 %. The TER effect in our FTJ was quantified by the TER ratio [$(J_> - J_<)/J_<$], resulting in a ratio of 20; this value is in the typical range of TER ratios (10>TER ratio>100).¹⁴

In the Pt/Hf_{0.5}Zr_{0.5}O₂/Pt configuration, the nominally symmetry is in fact incompatible with the TER effect observed and the effects invoked by Bilc et al.⁴² for an FTJ with symmetric electrodes cannot account for the values we observe. The *de facto* asymmetry was attributed to the presence of different interface states since experimental procedure required the breaking of the vacuum for the top electrode deposition through a contact mask. Owing to the TER effect, an FTJ’s electrical resistance depends on the polarization orientation.¹⁵ The low resistance state of our FTJ occurs when the ferroelectric polarization of Hf_{0.5}Zr_{0.5}O₂ points to the Pt bottom electrode (BE), it bends down the conduction band and lowers the potential barrier height ([Figure 48](#) (c)), due to the build-up of negative screening charges near the Hf_{0.5}Zr_{0.5}O₂/Pt (BE) interface.^{14-15, 18} Inversely,

when the ferroelectric polarization of Hf_{0.5}Zr_{0.5}O₂ points to the Pt top electrode, positive screening charges will build up at the Hf_{0.5}Zr_{0.5}O₂/Pt (BE) interface bending upward the conduction band, and creating an insulating region at the bottom interface resulting in a high-resistance state of the device.^{14-15, 18}

5.4.5 Summary

In summary, an FTJ memory device was fabricated, consisting of platinum top and bottom electrodes, and a 2.8 nm-thick Hf_{0.5}Zr_{0.5}O₂ tunnel barrier. The combination of piezoresponse force microscopy with conductive-AFM demonstrate the ferroelectric behavior of the ultrathin Hf_{0.5}Zr_{0.5}O₂ layer as well as the typical current-voltage characteristic of a ferroelectric tunnel junction device, respectively. Also, a direct tunneling model for an electrostatic potential profile with rectangular shape was used to correlate electronic and electrical transport properties of the Pt/Hf_{0.5}Zr_{0.5}O₂/Pt heterojunction, demonstrating a large change in electrical resistance (TER ratio close to 20), this change in electrical resistance is comparable to those reported for other FTJs.¹⁰⁵ Then, this study attests to the potential of Hf_{0.5}Zr_{0.5}O₂ as an FTJ CMOS compatible material to replace the current semiconductor memory technologies.

5.5 ASYMMETRIC FTJ MEMORY DEVICE (TiN/Hf_{0.5}Zr_{0.5}O₂/Pt)

5.5.1. Fabrication of the asymmetric FTJ memory device

Hf_{0.5}Zr_{0.5}O₂/TiN bilayers were grown by radio frequency magnetron sputtering on (100) *p*- type Si substrates. The TiN bottom electrode was deposited at 400°C in a N₂ and Ar atmosphere ($P_N = N_2/(Ar + N_2) = 70\%$) using a sputtering pressure of 10 mTorr. The subsequent growth of Hf_{0.5}Zr_{0.5}O₂ was performed at 450°C. During this step, the sputtering medium consisted of a mixture of Ar and O₂ ($P_o = O_2/(Ar + O_2) = 50\%$) and the RF power on the one inch in diameter polycrystalline Hf_{0.5}Zr_{0.5}O₂ target was fixed to 20 W. A 30 nm thick polycrystalline Pt top electrode was deposited using *DC* sputtering through a shadow mask consisting of an array of 300 μm diameter holes (Appendix B). Deposition parameters are listed in Table 9.

Table 9. Summary of sputtering conditions used for the fabrication of the asymmetric FTJ

Film:	TiN	Hf _{0.5} Zr _{0.5} O ₂	Pt
Target:	TiN ¹	Hf _{0.5} Zr _{0.5} O ₂ ¹	Pt ²
Substrate:	(100) p-type Si	TiN/(100) p-Si	HZO/TiN/(100)p-Si
Power density:	~4 W/cm ²	~4 W/cm ²	~5 W/cm ²
Target-substrate spacing:	11 cm	11 cm	11 cm
Sputtering medium: ³	Ar and N ₂ ⁴	Ar and O ₂ ⁵	Ar
Sputtering pressure:	10 mTorr	5 mTorr	5 mTorr
Substrate temperature:	400°C	450°C	25°C
Pre-sputtering time:	120 min	45 min	3 min
Deposition time:	15 min	15 min	15 min

¹Target dimensions: Ceramic disc (2.54cm in diameter; 0.317cm in thickness)

²Target dimensions: Metallic disc (2.54cm in diameter; 0.158cm in thickness)

³Gass purity: Argon (99.998% pure), Nitrogen (99.998%) and Oxygen (99.993%)

⁴Nitrogen partial pressure: $P_N = N_2/(Ar + N_2) = 70\%$

⁵Oxygen partial pressure: $P_o = O_2/(Ar + O_2) = 50\%$

Targets: TiN ceramic disc (99.9% pure), Hf_{0.5}Zr_{0.5}O₂ ceramic disc (99.9% pure) and Pt metallic disc (99.9% pure)

The surface morphology of the as-grown Hf_{0.5}Zr_{0.5}O₂ sample is shown in Figure 49 (a). It depicts a grainy layer uniformly covering the TiN substrate surface. The layer is thin enough that some atomic steps/terraces are still visible. The small grains characteristic of Hf_{0.5}Zr_{0.5}O₂ are also visible, and a root-mean-square (rms) roughness of ~0.25 nm is obtained over an 1x1 μm² area, attesting the atomic flatness of the Hf_{0.5}Zr_{0.5}O₂/TiN heterostructure's surface.

As the TER effect is highly dependent on the barrier width,¹⁶ it is crucial to determine the layer thickness of our films. Using XRR measurements (Figure 49 (b)), the layer thickness was estimated to ~2.8 nm (6 unit cells of Hf_{0.5}Zr_{0.5}O₂) for the films used in the fabrication of the FTJ and ~5.2 nm for those used in the structural analysis.

To gain insight into the structural properties of the ultrathin Hf_{0.5}Zr_{0.5}O₂ film on the TiN substrate, a phase identification was performed using grazing incidence angle X-ray diffraction (Figure 49 (c)). The diffraction peaks from the (111), (200), and (220) planes belong to the non-centrosymmetric orthorhombic phase, which presents ferroelectric properties. The ferroelectric phase is obtained during the initial stages of film growth. It starts with the nucleation of small grains with a high surface and volume ratio, which results in the formation of a tetragonal phase ($P4_2/nmc$). However, the large tensile strain along the c-axis induced by the coalescence of the nucleating grains allows the formation of the ferroelectric orthorhombic phase ($Pbc2_1$).²⁴ The XRD presented in Figure 49 (c) confirms the film composition, as a change in the Hf/Zr ratio would result in the appearance of other peaks in 2Θ .²⁶

The present asymmetric FTJ cell memory is 300 μm in diameter, the TiN bottom electrode has a layer thickness of 30 nm, the ferroelectric Hf_{0.5}Zr_{0.5}O₂ layer has a thickness of 2.8 nm and the top electrode has a layer thickness of 30 nm (Figure 49 (d)).

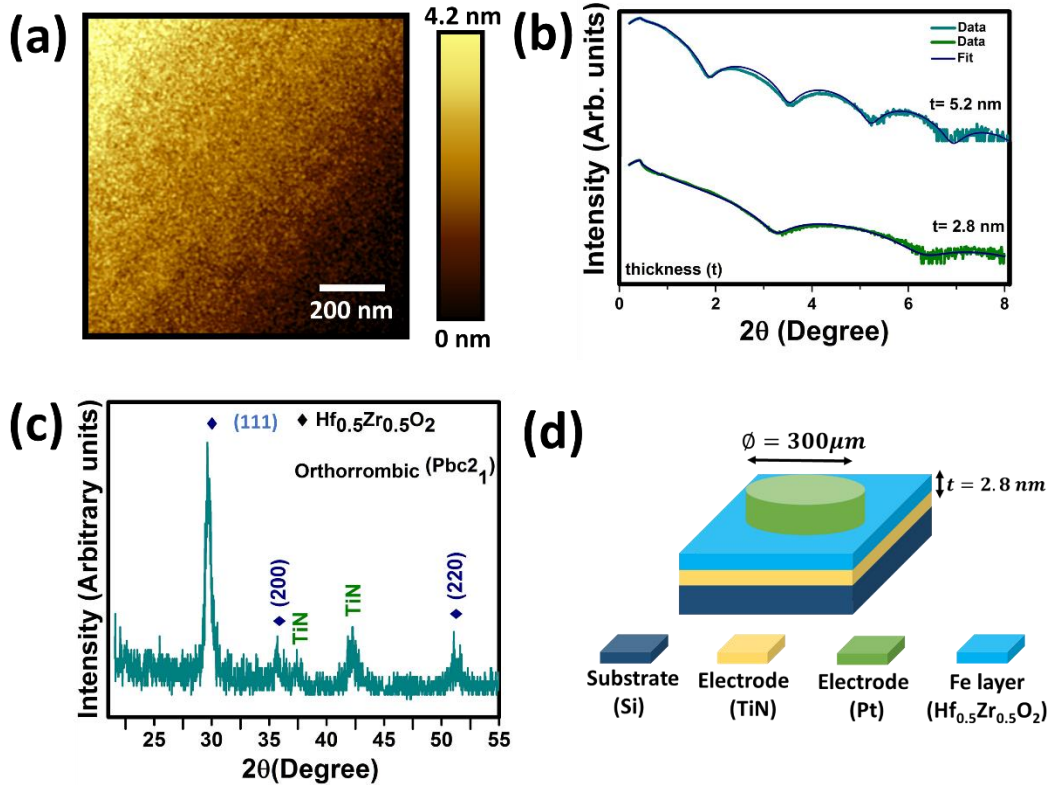


Figure 49. (a) $1 \times 1 \mu\text{m}^2$ AFM topography image of an $\text{Hf}_{0.5}\text{Zr}_{0.5}\text{O}_2$ film on a TiN substrate, (b) XRR spectra measured on $\text{Hf}_{0.5}\text{Zr}_{0.5}\text{O}_2$ films, (c) glancing X-ray diffraction spectrum of an $\text{Hf}_{0.5}\text{Zr}_{0.5}\text{O}_2$ film deposited on a TiN bottom electrode and (d) Schematic representation of one asymmetric FTJ cell memory; TE, HZO, FE and BE stands for “Top Electrode”, “ $\text{Hf}_{0.5}\text{Zr}_{0.5}\text{O}_2$ ”, “Ferroelectric” and “Bottom Electrode”, respectively.

5.5.2 Ferroelectric characterization of the asymmetric FTJ memory device

The first requirement to realize a ferroelectric tunnel junction device is for the nanometer-thick film to present ferroelectric properties.¹⁶ For this reason, the ferroelectric properties of the 6-unit-cell-thick $\text{Hf}_{0.5}\text{Zr}_{0.5}\text{O}_2$ film were investigated at room temperature on an FTJ device. The Figure 50 (a) revealed a clear hysteretic behavior in both phase, as shown by the $\sim 180^\circ$ difference, and the amplitude signals, acquired out of the resonance frequency of the cantilever, as a function of voltage. The ferroelectric switching voltages that create the downward and upward polarization were found to be $+1.9 \text{ V}$ and -1.9 V , respectively. These results confirm the ferroelectric behavior of the ultrathin $\text{Hf}_{0.5}\text{Zr}_{0.5}\text{O}_2$ film. Figure 50 (b) shows a PFM phase-contrast image depicting intentionally-written ferroelectric patterns. Three intersecting squares located from the bottom left to the top right were poled with voltages of -3 V , $+3 \text{ V}$, and -3 V ,

demonstrating upward, downward and upward polarizations, respectively. The remaining area corresponds to the virgin state, which exhibits a preferential downward-polarization. This spontaneous polarization was caused by the presence of substrate-induced strains in the Hf_{0.5}Zr_{0.5}O₂ film,⁵¹ while the intersecting squares show the capability of the material to go through a full cycle of ferroelectric polarization switching. The presented ferroelectric patterns are stable for over 60 hours, which suggests a stable and robust ferroelectric polarization of the Hf_{0.5}Zr_{0.5}O₂ layer (Appendix C). This PFM analysis is in agreement with the XRD results, confirming the formation of the non-centrosymmetric orthorhombic ferroelectric phase.

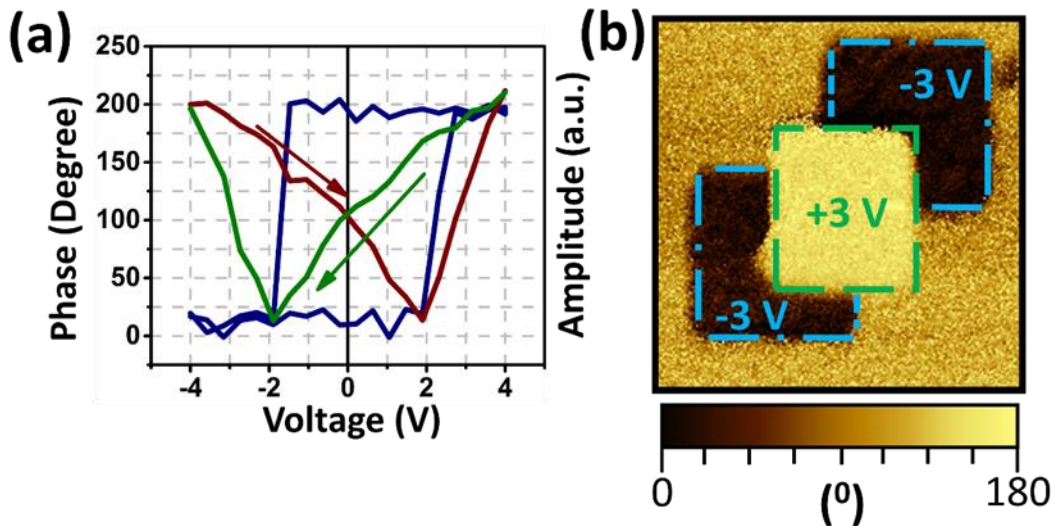


Figure 50. (a) Local PFM hysteresis loops of the phase (blue curve) and the amplitude signal (green-red curve) and (b) 2.5 μm × 2.5 μm PFM phase-contrast image.

5.5.3 Electronic properties of the asymmetric FTJ memory device

Optical constants such as the bandgap (E_g) can be estimated from UV-visible transmission spectroscopy measurements, while the carrier transport properties at the ferroelectric /metal interface can be well understood by determining the valence band offset as well as the potential step barrier.¹⁰⁹⁻¹¹⁰ So, accurate knowledge of these optical and electronic parameters is essential for identifying a suitable ferroelectric layer for FTJ.²⁵

To gain quantitative information on the electronic properties at both interfaces of the FTJ system (TiN/Hf_{0.5}Zr_{0.5}O₂ and Hf_{0.5}Zr_{0.5}O₂/Pt), we used the Kraut procedure.¹⁰⁶⁻¹⁰⁷ This method consists in measuring the valence band offset (VBO) by finding the core level signals provided by

the film and the substrate, the Fermi energy level (E_F) of the metallic bulk material as well as the valence band maximum (VBM) of the ferroelectric layer. Starting with the first interface (TiN/Hf_{0.5}Zr_{0.5}O₂), the VBO was calculated using the following equation,

$$VBO = (BE_{Ti2p} - E_F)_{TiN} - (BE_{Hf4f} - VBM)_{HZO} - (BE_{Ti2p} - BE_{Hf4f})_{HZO/TiN} \quad (17)$$

The energy separation between the Ti2p centroid with respect to the leading edge of the Fermi level for the bulk TiN sample, was found to be 455.4 ± 0.05 eV. The energy difference between the Hf4f centroid and the VBM for the bulk Hf_{0.5}Zr_{0.5}O₂ was estimated to be $14.1 \text{ eV} \pm 0.05$. The binding energy difference between Ti2p and Hf4f core levels in the ultrathin film, was calculated to be 438.1 ± 0.05 eV. Substituting these values in Eq. 17, the VBO was determined to be 3.2 ± 0.05 eV at the TiN/ Hf_{0.5}Zr_{0.5}O₂ interface. This analysis and the obtained values are schematically described in Figure 51.

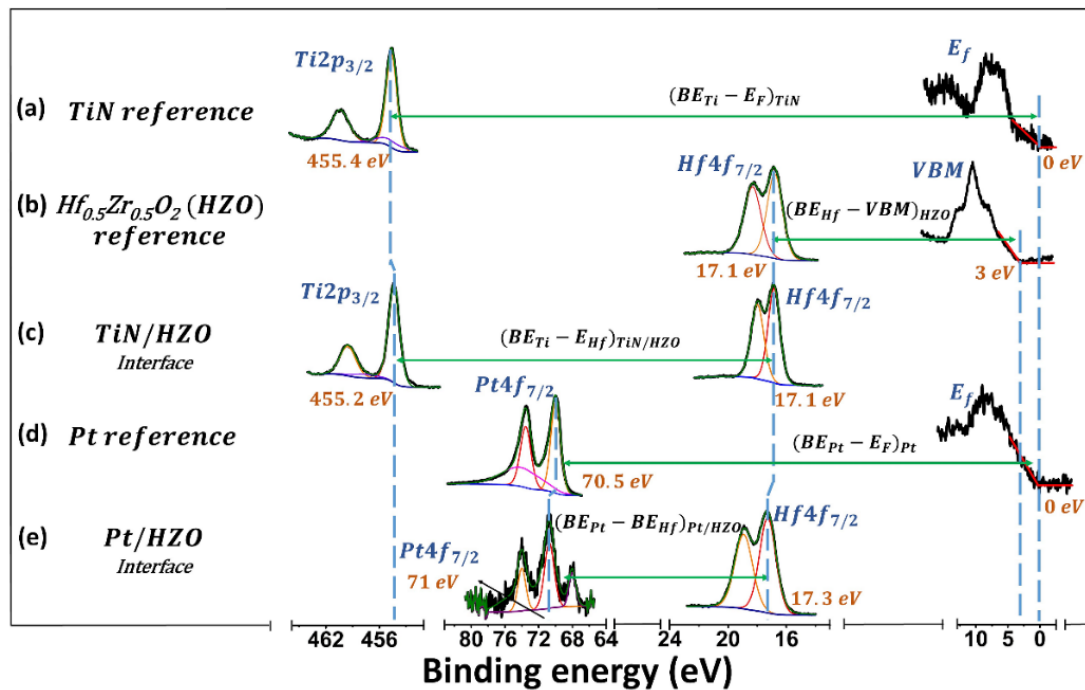


Figure 51. XPS spectra taken on the (a) thick TiN film, (b) thick Hf_{0.5}Zr_{0.5}O₂ layer, (c) TiN/ Hf_{0.5}Zr_{0.5}O₂ interface, (d) bulk Pt film and (e) Hf_{0.5}Zr_{0.5}O₂/Pt interface.

The same procedure was employed to measure the VBO at the second interface (Hf_{0.5}Zr_{0.5}O₂/Pt, Figure 51). For the reference bulk metallic Pt sample, an energy difference equal to 70.5 ± 0.05 eV was obtained, while the core level line separation on the Pt/ Hf_{0.5}Zr_{0.5}O₂ ultrathin

sample was found to be 53.7 ± 0.05 eV. From these values we found the second VBO to be equal to 2.70 ± 0.05 eV ([Appendix D](#)).

The conduction band offset (or potential step barrier, φ) is given by

$$\varphi = E_g - VBO \quad (18)$$

Therefore, the potential step barriers at the TiN/ $\text{Hf}_{0.5}\text{Zr}_{0.5}\text{O}_2$ (φ_1) and at the $\text{Hf}_{0.5}\text{Zr}_{0.5}\text{O}_2/\text{Pt}$ (φ_2) interfaces were calculated to be 1.86 ± 0.07 eV and 2.36 ± 0.07 eV, respectively. The reconstructed electronic band diagram for the TiN/ $\text{Hf}_{0.5}\text{Zr}_{0.5}\text{O}_2/\text{Pt}$ heterostructure with spontaneous downward polarization is shown in [Figure 52](#).

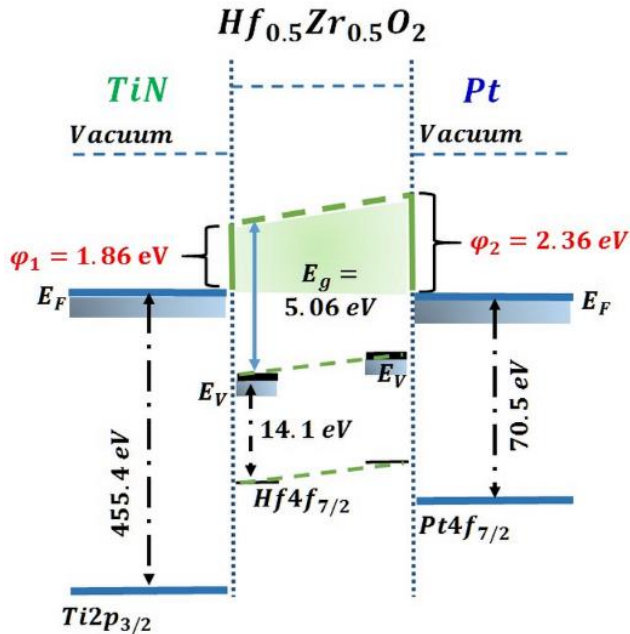


Figure 52. Schematic representation of the electronic band diagram for the TiN/ $\text{Hf}_{0.5}\text{Zr}_{0.5}\text{O}_2/\text{Pt}$ heterostructure.

5.5.4 Tunneling electroresistance effect on the asymmetric FTJ memory device

The TER effect in our system was investigated using nanoscale electrical measurements. A representative I - V curve measured on the $\text{TiN}/\text{Hf}_{0.5}\text{Zr}_{0.5}\text{O}_2/\text{Pt}$ devices is presented in Figure 53 (a). It depicts a hysteretic I - V behavior characterized by an initial high resistance state (“OFF” state, green line), which switched to a low resistance state (“ON” state, blue line). The hysteretic electrical behavior as well as the large change in electrical resistance between the two states suggest a TER effect.^{43, 51, 105}

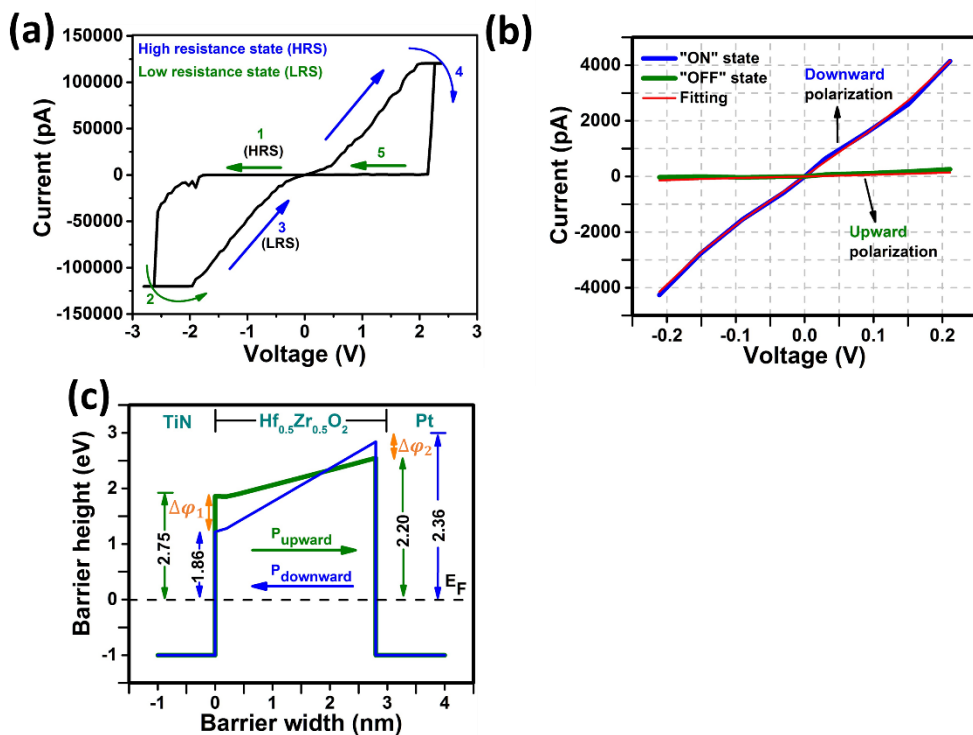


Figure 53. (a) Typical I - V characteristic measured on a $300 \mu\text{m}$ diameter the $\text{TiN}/\text{Hf}_{0.5}\text{Zr}_{0.5}\text{O}_2/\text{Pt}$ heterostructure displaying low and high resistance states, (b) Electrostatic potential barrier as a function of the polarization direction and (c) Electronic potential profile for two different states.

In order to confirm that the resistive switching observed in Figure 53 (a) is due to the TER effect rather than another resistive switching mechanism, a method proposed by Zenkevich et. al.¹⁰⁵ was used. It correlates the interfacial electronic properties with the electrical transport properties of the $\text{TiN}/\text{Hf}_{0.5}\text{Zr}_{0.5}\text{O}_2/\text{Pt}$ heterostructure by employing a direct tunneling current model across a trapezoidal barrier.¹¹¹ This model consists in calculating the tunneling current density (J) as a function of voltage (V), using the potential barrier steps at both ferroelectric-electrode

interfaces (φ_1 and φ_2), layer thickness (d), electron charge (e) and the effective electron mass (m) as described by the Brinkman model.^{43, 111}

$$J = - \left(\frac{4em}{9\pi^2\hbar^3} \right) \left(\frac{\exp(\alpha(V)[(\varphi_2 - \frac{eV}{2})^{\frac{3}{2}} - (\varphi_1 + \frac{eV}{2})^{\frac{3}{2}}])}{\alpha^2(V)[(\varphi_2 - \frac{eV}{2})^{\frac{1}{2}} - (\varphi_1 + \frac{eV}{2})^{\frac{1}{2}}]^2} \right) \times \sinh\left(\frac{3}{2}\alpha(V)[(\varphi_2 - \frac{eV}{2})^{\frac{1}{2}} - (\varphi_1 + \frac{eV}{2})^{\frac{1}{2}}]\frac{eV}{2}\right) \quad (19)$$

where $\propto(v) = [4d(2m)^{1/2}]/[3\hbar(\varphi_1 + eV - \varphi_2)]$ and \hbar is the reduced Planck constant (Appendix E). The theoretical I - V curve for the “ON” state (downward polarization) was plotted using the potential barrier values obtained by XPS ($\varphi_1=1.86$ eV and $\varphi_2=2.36$ eV), and adding only the scaling factor, which was assumed to be the same for both states, following the method described in the literature.^{43, 105} Then, using the same scaling factor and Eq. 19, the I - V curve for the “OFF” state was fitted to obtain the potential barriers for that state. As shown in Figure 53 (b), a good agreement was obtained during the fitting of the I - V curve with the theoretical model described in Eq. 19 for both the “OFF” and “ON” states. From this model, we obtained two potential barriers ($\varphi_1 = 2.75$ eV and $\varphi_2 = 2.20$ eV), which produce the “OFF” state in the I - V curve (upward polarization). Hence, the polarization reversal changes at the TiN/Hf_{0.5}Zr_{0.5}O₂ and the Hf_{0.5}Zr_{0.5}O₂/Pt interfaces are $\Delta\varphi_1 = 0.89$ eV and $\Delta\varphi_2 = 0.16$ eV, respectively. The derived changes in the potential barrier profile are shown in Figure 53 (c). Indeed, the electrostatic potential profile was modulated by the polarization reversal of the ultrathin layer. When the polarization vector of Hf_{0.5}Zr_{0.5}O₂ points to the TiN bottom electrode, the conduction band will bend downward due to the build-up of negative screening charges in the TiN electrode.

This will be followed by the lowering of the potential barrier height at Hf_{0.5}Zr_{0.5}O₂/TiN interface, resulting in a low-resistance state (Figure 53 (c), downward state). On the other hand, when the polarization vector of Hf_{0.5}Zr_{0.5}O₂ points to the Pt top electrode, positive screening charges will build up at the Hf_{0.5}Zr_{0.5}O₂/TiN interface, bending the conduction band upward and resulting in a high-resistance state (Figure 53 (c), upward state). The TER effect in our FTJ was quantified by the TER ratio [$(J_> - J_<)/J_<$], resulting in a $TER \sim 15 \pm 3$ at -0.2 V.

5.5.5 Evaluation of the asymmetric FTJ memory device

The endurance of the TiN/Hf_{0.5}Zr_{0.5}O₂/Pt heterostructures was evaluated by recording 500 *I-V* cycles under quasi-static conditions on the same FTJ memory cell. Given that contacting by the AFM was required, the acquisition speed was limited by the AFM specifications and a 500 cycle quasi-static measurement already took a day. For each *I-V* curve, we obtained the “ON” and “OFF” resistances at a read voltage of -0.2 V (Figure 54 (a)). They remain stable over five hundred switches, indicating a good endurance of the FTJs.

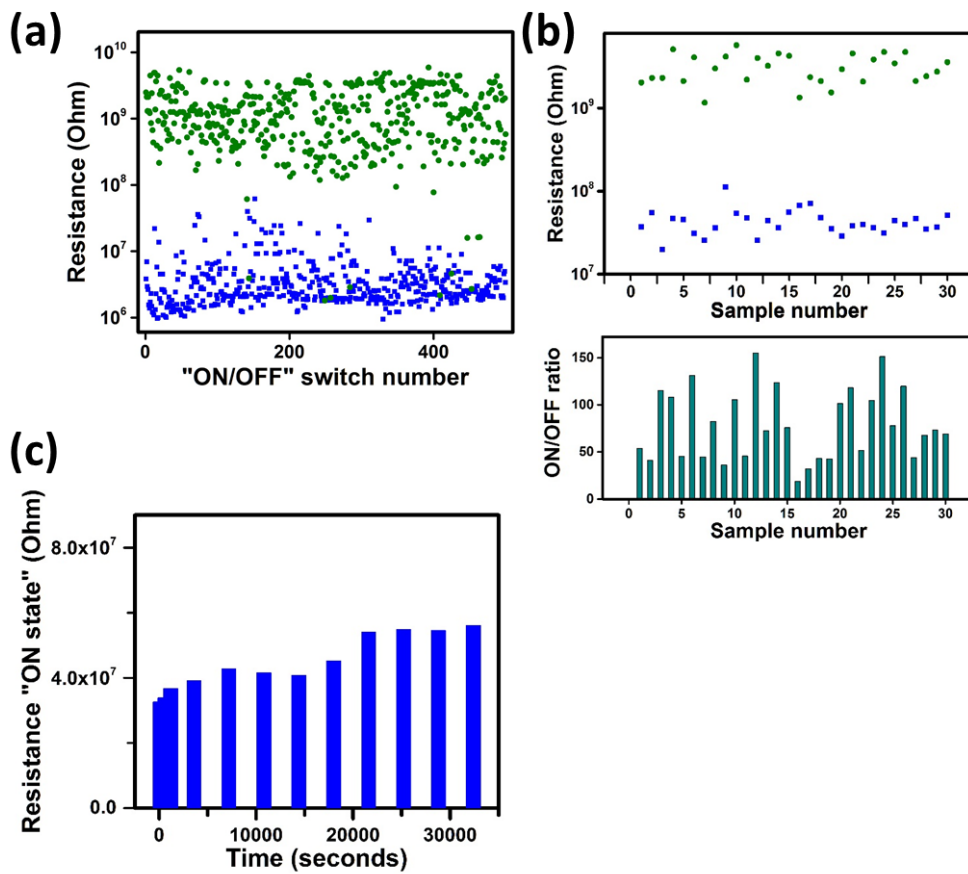


Figure 54. Memory performances of the FTJ devices: (a) Fatigue measurements on a TiN/ Hf_{0.5}Zr_{0.5}O₂/Pt (diameter of 300 μm) heterostructure displaying the ‘OFF’ (green) and ‘ON’ (blue) resistance values over 500 write/read cycles, (b) ‘ON’ and ‘OFF’ resistances state (upper panel) and ON/OFF ratios (bottom panel) of 30 different FTJ memory cells, and (c) Retention properties, where the “ON” resistance state was measured as a function of time at a read voltage of -0.2 V.

The reproducibility of the TER effect in the FTJs under study was investigated by recording *I-V* cycles from 30 different FTJ devices. For each memory cell, the resistance values for both the “ON” and “OFF” states were recorded at -0.2 V. The 30 memories cells presented an ON/OFF ratio, or TER ratio, of 43±16 on average ([Figure 54 \(b\)](#)). This result attests to the high reproducibility of the TER effect in the TiN/ Hf_{0.5}Zr_{0.5}O₂/Pt FTJ memory devices.

The retention properties of the present FTJ were evaluated on a single memory cell, by recording the “ON” resistance state value over time at a read voltage of -0.2 V. As shown in [Figure 54 \(c\)](#) the “ON” resistance state can still be read after eight hours, demonstrating that our FTJ devices present good retention.

5.5.6 Summary

In summary, the successful fabrication of an FTJ device based on a CMOS compatible tunnel barrier (Hf_{0.5}Zr_{0.5}O₂) and a TiN bottom electrode is reported. The formation of the metastable ferroelectric orthorhombic phase was confirmed by correlating the results of grazing angle incidence XRD with those acquired by PFM. By combining XPS and UV-Visible spectroscopies, the potential step barriers were determined to be 1.86 eV and 2.32 eV at the bottom and top interfaces of the TiN/Hf_{0.5}Zr_{0.5}O₂/Pt heterostructure, respectively. The Brinkman model confirmed the presence of a large electroresistance effect, with a TER ratio equal to ~15 (at -0.2 V). The semiconductor memory evaluation that revealed that the present FTJ can operate at low voltages (-0.2 V) over a relative large number of cycles (500 cycles), non-volatile nature as well as deposition parameters compatible with semiconductor industry. Then our results hold the promise for novel semiconductor memory devices, since FTJs have the potential to overcome the limitation of conventional semiconductor memory devices.

Summary and outlook

SUMMARY

This thesis has addressed a fabrication method of two different types of FTJ memory prototypes “asymmetric-FTJ” and “nominally symmetric-FTJ”. The semiconductor memory evaluation has shown that the asymmetric FTJ memory presents well-defined stable states over a relative large number of cycles (good endurance), good retention due to its non-volatile nature as well as a process which apart of being reproducible, it is compatible with the silicon semiconductor industry. Therefore, the tunneling electroresistance effect (physical concept) of the FTJ memory represents a leap towards the universal memory.

Ultrathin ferroelectric barriers

The present work has evaluated the ferroelectricity in ultrathin film form of two different oxides:

i) *Barium titanate ($BaTiO_3$)* was grown on a (100)-oriented Nb:SrTiO₃ substrate. Transferring the stoichiometry of barium titanate target to the substrate surface for on-axis conditions was challenging, due substrate etching observed for common power densities. To control the re-sputtering effects, an optimization of the sputtering parameters was performed, it resulted in the deposition of stoichiometric barium titanate (Ba/Ti ratio~1). A short deposition time (7 minutes) resulted in epitaxial growth of an ultrathin barium titanate on niobium-doped strontium titanate substrates. Piezoresponse force microscopy analysis revealed the ferroelectric character of this barium titanate ultrathin film (4nm-thick). The demonstration of ferroelectric tunnel junction devices based on this material has already been accomplished. However, integrating FTJs based on perovskite materials remains challenging, mainly due to the incompatibility of the thermal process budget with the CMOS process.

ii) *Hafnium zirconium oxide ($Hf_{0.5}Zr_{0.5}O_2$)* was grown on a (100)-oriented TiN/p-Si and on a (111)-oriented Pt substrates. Stoichiometric Hf_{0.5}Zr_{0.5}O₂ resulted at a small sputtering pressure (5mTorr), a low RF-power (4W/cm²) and a relative low substrate temperature (425°C). Piezoresponse Force Microscopy revealed robust ferroelectricity in Hf_{0.5}Zr_{0.5}O₂ in ultrathin film form (layer thickness from 2 nm to 14 nm), however the ferroelectricity of Hf_{0.5}Zr_{0.5}O₂ disappeared

as its layer thickness was increased (larger than 14 nm). In general, the combination of a CMOS compatible deposition process with excellent ferroelectric properties makes $\text{Hf}_{0.5}\text{Zr}_{0.5}\text{O}_2$ an excellent candidate for future memory technologies.

Fabrication and evaluation of the FTJ memory device

Two types of ferroelectric tunnel junction devices were fabricated: *nominally symmetric-FTJ* and *Asymmetric-FTJ*. In both cases the electronic charge transport across the metal/ferroelectric interfaces was studied by X-ray photoelectron and UV-visible spectroscopies combined with conductive-AFM measurements and piezoresponse force microscopy.

The nominally symmetric FTJ was fabricated by capping a 2.8 nm-thick $\text{Hf}_{0.5}\text{Zr}_{0.5}\text{O}_2$ film deposited on platinized substrate with a platinum top electrode. In this configuration, the use of electrodes made of same materials should in principle result in an electrostatic potential profile with square shape, incompatible with the tunneling electroresistance effect. However, coherent direct tunneling was observed across the nominally symmetric-FTJ memory device, with a TER ratio of 20 (comparable with those FTJs reported in literature). The *de facto* asymmetry is attributed to the presence of different interface states. More specifically, the breakdown of the electrostatic symmetry originates from different oxidation histories for both platinum electrodes.

The asymmetric FTJ is based on a CMOS compatible tunnel barrier ($\text{Hf}_{0.5}\text{Zr}_{0.5}\text{O}_2$) sandwiched between an equally CMOS compatible titanium nitride bottom electrode and a platinum top electrode. The combination of different experimental techniques (Conductive-AFM, Piezoresponse Force Microscopy, X-ray Phototelson Spectroscopy, UV-Vis and X-ray difraction) with a theoretical model (direct tunneling equation across a trapezoidal electrostatic potential profile barrier) confirmed the observation of tunneling electroresistance effect in the present FTJ memory device. Furthermore, the semiconductor memory evaluation of this asymmetric-FTJ revealed excellent properties such as large TER ratio (TER ratio~15) measured at low electric field (-0.2 V), good endurance (its two stable states remained stable over 500 cycles), good retention (up to nine hours), non-volatile nature and excellent reproducibility.

OUTLOOK

The experimental demonstration of tunneling electroresistance effect in an FTJ memory was reported in 2009,^{9,17} while the method to characterize tunneling current mechanism in a FTJ were first published in 2013.¹⁰⁵ Then, the original contribution of the present thesis is the successful fabrication of the first FTJ memory device made of CMOS compatible materials. However, through the development of this work, some question has been raised. The address of these questions will allow to better understand a CMOS compatible FTJ memory:

- 1) The origin of the unexpected ferroelectricity of the HfO₂-ZrO₂ films is due to the formation of the non-centrosymmetric orthorhombic phase. However, the formation of this phase in this solid solution has not yet been clearly described. Therefore, it is important to examine the evolution of the local structure of this binary system using a phase diagram as a function of inhomogeneous and biaxial strain as well as temperature. This phase diagram can be used as a research tool to control the structure and the composition of the critical phases of the binary system (HfO₂-ZrO₂).
- 2) In an FTJ memory device different types of electronic current mechanisms may contribute to the effective carrier conduction across the ultrathin ferroelectric layer. These mechanisms are known as direct tunneling, thermionic emission and Fowler-Nordheim tunneling. In the literature, the thermionic injection and the Fowler-Nordheim tunneling are usually ignored for simplicity. However, recent theoretical work reported by Pantel et al.³⁰ demonstrates that the three types of electronic current mechanism play an important role in the electronic transport of the FTJ memory device. Therefore, it will be of importance to study the role of each one of these electronic current transport on an FTJ memory device
- 3) For the sake of a better device stability and to prevent parasitic resistive switching through oxygen-diffusion, the device should be encapsulated under an oxygen-diffusion-barrier. This will further enhance the lifetime of the memory device under operation.
- 4) In terms of memory performance, the material components and the semiconductor properties of the FTJ need to be optimized. This includes the replacement of the platinum top electrode by a CMOS compatible electrode such as iridium/iridium oxide.

- 5) Replacing quasi-static I-V measurements by pulse electric measurements, they will provide a far more realistic estimation for reliability and endurance and will ultimately determine the read/write access time of our FTJ memory
- 6) Ferroelectric tunnel junction memory device store the data in binary form (“1” and “0” logic states). However, the continued demand for miniaturization and integration is pushing forward to the development of FTJ memory devices that can operate in the field of multi-stage storage field. Therefore, an investigation of multilevel data storage has to be performed. These studies will include ultrafast and thus only partial polarization reversal of the FTJ.¹¹²⁻¹¹⁵
- 7) The final version of an FTJ will be inevitably affected by polarization-independent leakage currents as well as incomplete crystallization. Both contributions will add a polarization independent current contribution that will ultimately reduce the TER ratio. A quantitative assessment on how the device performance will be affected will certainly help to evaluate the potential in memory applications.
- 8) At present, the device exhibits a relatively large ON resistance due to the fact that a tunnel junction remains a relatively poor conductor. Decreasing the thickness will exponentially decrease the direct tunneling resistance thus improving the RC time constants of the memory device.

Appendix A

THICKNESS MEASUREMENT OF BARIUM TITANATE

The thickness of our BaTiO_3 films was measured by X-ray reflectometry for various deposition times (1, 2, and 3.5h) and from the slope of this linear fitted curve the thickness of films deposited for shorter times were extrapolated. The fit is forced through the origin ([Figure A1](#)), taking zero thickness without deposition into account.

The epitaxial growth of BaTiO_3 film on a $\text{Nb}: \text{SrTiO}_3$ substrate was confirmed by x-ray diffraction studies which reveals an overlapping between the diffracted planes of the substrate and film ([Figure A1\(c\)](#)). It suggests that the film had grown in the same crystallographic orientation of the substrate.

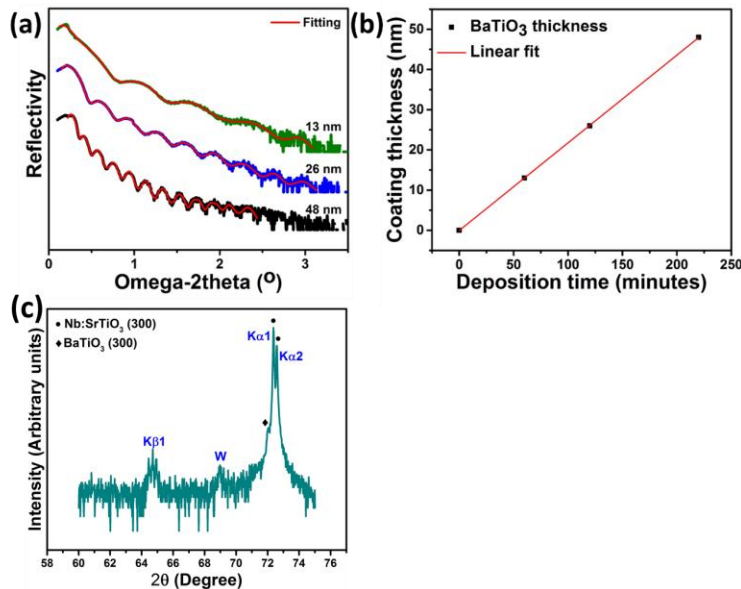


Figure A1. (a) Thickness measurement of BaTiO_3 thin films where the red solid lines represent numerical fits to extract the thickness, (b) A linear fit (red curve) for the thickness as a function of deposition time and (c) X-ray diffraction pattern of the BaTiO_3 film epitaxial growth on a $\text{Nb}: \text{SrTiO}_3$ substrate.

X-RAY PHOTOELECTRON SPECTROSCOPY ANALYSIS

The binding energy scale was calibrated based on the spectra of a gold standard sample by setting the Au4f_{7/2} at a binding energy of 84.00 eV, as illustrated in [Figure A2](#).

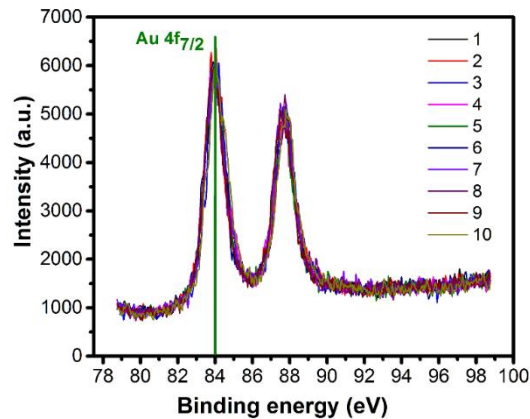


Figure A2. XPS spectra of a gold standard sample.

The measurement was repeated ten times, and the gold binding energies values obtained, are listed in [Table A1](#). Those values were used to calculate the repeatability standard deviation, and a value of 0.05 eV was obtained. The present result is accepted by the ASTM standard E 2108-00.¹¹⁶

Table A1. Reference binding energies for a gold peak used in the calibration procedure.

Measurement number	Assignment signal	Source: Monochromatic Al K _a
1		84.00
2		84.00
3		83.90
4		84.00
5	Au 4f _{7/2}	84.00
6		84.00
7		84.00
8		84.00
9		84.00
10		84.10

Standard deviation= 0.047 eV (~0.05 eV)

Appendix B

STRUCTURAL PROPERTIES OF THE PLATINUM TOP ELECTRODE

The structural properties of the Pt top electrode were studied using a grazing incidence angle XRD (Philips X’Pert Materials Research Diffractometer). The XRD pattern of Figure B1(a) show the characteristic diffraction peaks of the cubic platinum phase (Swanson, Tatge., *Natl. Bur. Stand. (U.S.)*, *Circ.* 539, **I**, 31, (1953)). In the same figure, the presence of the diffracted planes with different crystallographic orientation attests to the polycrystalline nature of the platinum top electrode.

The layer thickness as well as the diameter of the platinum top electrode were determined using a profilometer (Bruker, Dektak XT). As shown in Figure B1(b), the profile of the platinum top electrode depicts a layer thickness of 30 nm and a diameter of 300 µm.

X-ray diffraction pattern of Figure B1(c) shows the diffracted planes that correspond to the platinum bottom electrode which presents random crystallographic orientation.

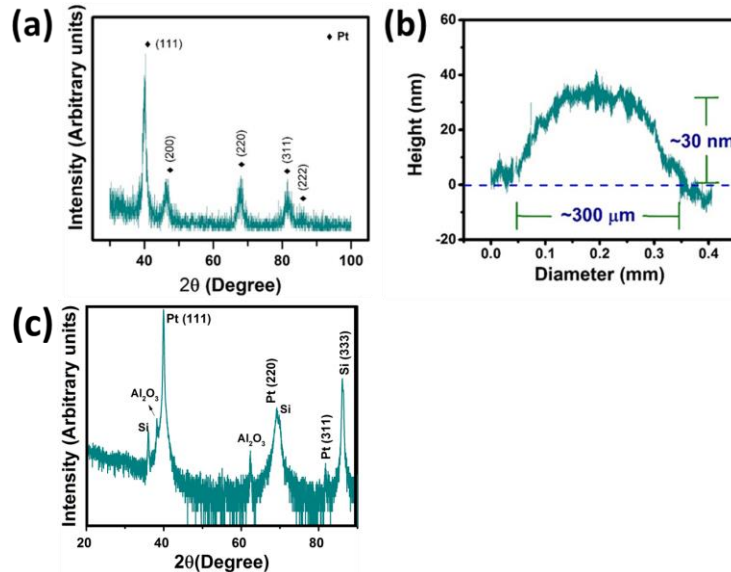


Figure B1. (a) Glancing incidence angle XRD spectrum of a Pt layer deposited on a Si substrate, (b) Line scan profile on the Pt top electrode in the TiN/Hf_{0.5}Zr_{0.5}O₂/Pt device and (c) x-ray diffraction pattern of the Pt bottom electrode.

Appendix C

FERROELECTRIC RETENTION OF HAFNIUM ZIRCONIUM OXIDE ULTRATHIN LAYER

The ferroelectric retention of the $\text{Hf}_{0.5}\text{Zr}_{0.5}\text{O}_2$ ultrathin layer was studied by imaging a poled pattern as a function of time (Figure C1). The antiparallel ferroelectric domains do not demonstrate relaxation within 40 hours. Moreover, after 60 hours the ferroelectric patterns presented only very slight changes. These results indicate a stable and robust ferroelectric polarization of the $\text{Hf}_{0.5}\text{Zr}_{0.5}\text{O}_2$ layer.

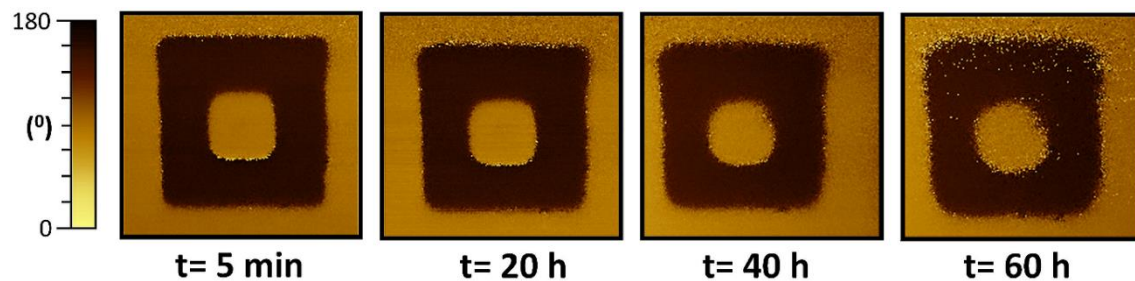


Figure C1. *Out-of-plane piezoresponse phase images indicating good ferroelectric retention on the bare surface of the $\text{Hf}_{0.5}\text{Zr}_{0.5}\text{O}_2$ layer on a TiN bottom electrode.*

Appendix D

BAND ALIGNMENT DETERMINATION

First interface (TiN/Hf_{0.5}Zr_{0.5}O₂)

The valence band offset (VBO) in the TiN/Hf_{0.5}Zr_{0.5}O₂ heterojunction is calculated according to the formula

$$VBO = (BE_{Ti2p} - E_F)_{TiN} - (BE_{Hf4f} - VBM)_{HZO} - (BE_{Ti2p} - BE_{Hf4f})_{HZO/TiN} \quad (D1)$$

As can be seen from [Figure D1](#), the TiN reference sample presents the Ti2p signal which consist of two peaks Ti2p_{3/2} (455.4 ± 0.05 eV) and Ti2p_{1/2} (461 ± 0.05 eV) due to the Ti-N bonds. The energy difference was obtained from the clean surface of a TiN reference sample and it was found $(BE_{Ti2p} - E_F)_{TiN} = 455.4 \pm 0.05$ eV.

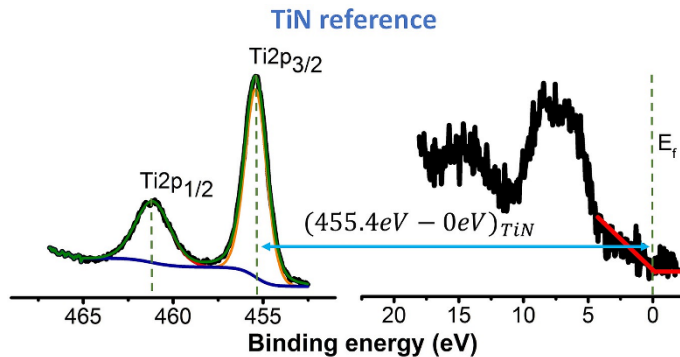


Figure D1. Separation between Ti2p_{3/2} core level line and Fermi energy level (E_F) measured on a reference bulk metallic TiN sample

In [Figure D2](#), the two peaks observed at 17.1 ± 0.05 eV and 18.6 ± 0.05 eV, are due to Hf4f_{7/2} and Hf4f_{5/2}, respectively, and correspond to Hf–O bonds. In the same figure the Hf4f_{7/2} line separation with respect to the valence band maximum for a pure Hf_{0.5}Zr_{0.5}O₂ reference film is $(BE_{Hf4f} - VBM) = 14.1 \pm 0.05$ eV

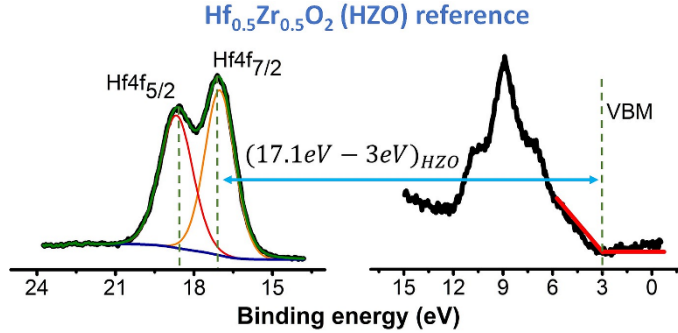


Figure D2. Separation between $\text{Hf}4\text{f}_{7/2}$ core level line and valence band maximum (VBM) measured on a reference bulk $\text{Hf}_{0.5}\text{Zr}_{0.5}\text{O}_2$ sample

The line separation $(BE_{\text{Ti}2p} - BE_{\text{Hf}4f}) = 438.1 \pm 0.05\text{eV}$ is obtained from the spectra measured on the $\text{Hf}_{0.5}\text{Zr}_{0.5}\text{O}_2(2.8\text{nm})/\text{TiN}$ heterostructure (Figure D3)

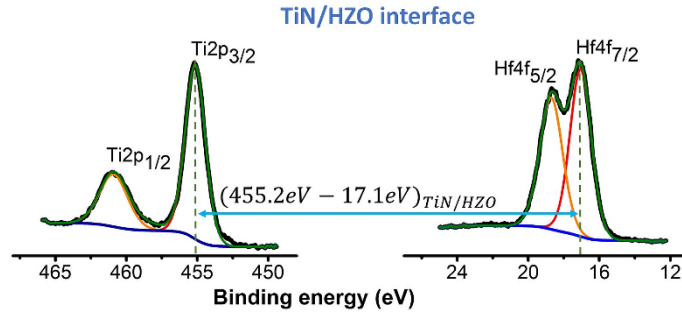


Figure D3. Separation between $\text{Ti}2\text{p}_{3/2}$ and $\text{Hf}4\text{f}_{7/2}$ core-level line measured on the 2.8 nm thick $\text{Hf}_{0.5}\text{Zr}_{0.5}\text{O}_2$ layer grown on the top of the TiN sample.

Substituting these values in Eq. D1, we determined the VBO to be 3.2 ± 0.05 eV at the $\text{TiN}/\text{Hf}_{0.5}\text{Zr}_{0.5}\text{O}_2$ interface.

Second interface ($\text{Hf}_{0.5}\text{Zr}_{0.5}\text{O}_2/\text{Pt}$)

The valence band offset (VBO) in the $\text{Hf}_{0.5}\text{Zr}_{0.5}\text{O}_2/\text{Pt}$ heterojunction is calculated according to the formula

$$VBO = (BE_{\text{Pt}4f} - E_F)_{\text{Pt}} - (BE_{\text{Hf}4f} - VBM)_{\text{HZO}} - (BE_{\text{Pt}4f} - BE_{\text{Hf}4f})_{\text{HZO/Pt}} \quad (\text{D2})$$

For the reference bulk metallic Pt sample we obtain an energy difference $(BE_{\text{Pt}4f} - E_F) = 70.5 \pm 0.05\text{eV}$, Figure D4.

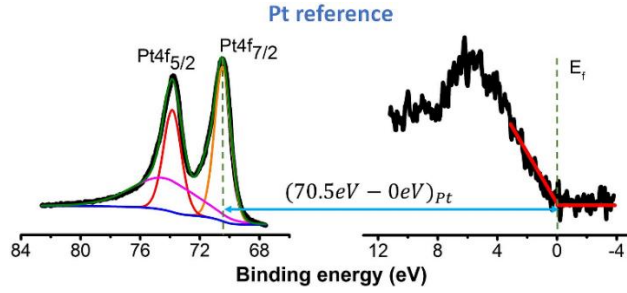


Figure D4. Separation between $\text{Pt4f}_{7/2}$ core level line and Fermi energy level (E_F) measured on a reference bulk metallic Pt sample

Figure D5 shows the core level line separation on the $\text{Hf}_{0.5}\text{Zr}_{0.5}\text{O}_2/\text{Pt}$ sample is found($BE_{\text{Pt}4f} - BE_{\text{Hf}4f} = 53.7 \pm 0.05\text{eV}$). Substituting these values in Eq. D2, we determined the VBO to be 2.70 ± 0.05 eV at the $\text{Hf}_{0.5}\text{Zr}_{0.5}\text{O}_2/\text{Pt}$ interface.

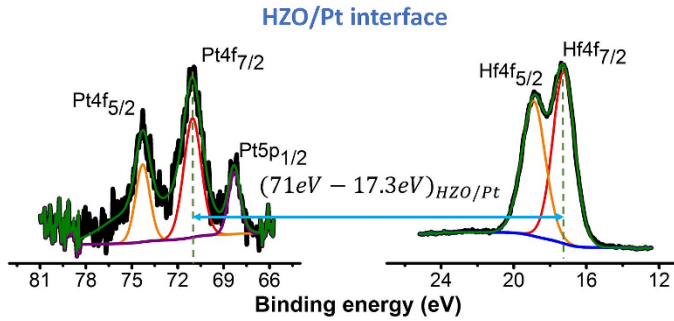


Figure D5. Separation between $\text{Pt4f}_{7/2}$ and $\text{Hf4f}_{7/2}$ core-level line measured on the 2.8nm thick $\text{Hf}_{0.5}\text{Zr}_{0.5}\text{O}_2$ layer grown on the top of a Pt sample.

Appendix E

SIMMONS MODEL

The Simmons' model,¹⁰⁸ is based on Fermi-Dirac statistics and WKB approximation, assuming a low voltage (V) and a barrier width (s). The tunneling current density (J) through a barrier at low voltage range, is given by

$$J = \left[\frac{3(2m\varphi)^{\frac{1}{2}}}{2s} \right] \left(\frac{e}{h} \right)^2 V \times \exp \left[-\frac{(4\pi s)}{h} (2m\varphi)^{\frac{1}{2}} \right] \quad (\text{E1})$$

The parameter used to fit the experimental data are enlisted in [table E1](#)

Table E1. *Input parameters used in eq. E1 of the manuscript to fit the downward and upward state of the current-voltage curve.*

	ON state	OFF state
Barrier height 1 (φ_1) ¹	2.67 eV	2.36 eV
Barrier height 2 (φ_2) ¹	2.67 eV	2.36 eV
Layer thickness (d)		2.8 nm
Electron mass (m)		$9.1094 \times 10^{-31} \text{ Kg}$
Electron charge (e)		$1.60217662 \times 10^{-19} \text{ C}$
Planck constant (\hbar)		$1.054571800 \times 10^{-34} \text{ J} \cdot \text{s}$

¹eV units of both potential barriers were converted to Joules (J)

BRINKMAN MODEL

The Brinkman model determines the tunneling current density (J) as a function of voltage (V), using the potential barrier steps at both ferroelectric-electrode interfaces (φ_1 and φ_2), layer thickness (d), electron charge (e) and the effective electron mass (m) as described by the Brinkman model.^{43, 111}

$$J = - \left(\frac{4em}{9\pi^2\hbar^3} \right) \left(\frac{\exp(\alpha(V)[(\varphi_2 - \frac{eV}{2})^{\frac{3}{2}} - (\varphi_1 + \frac{eV}{2})^{\frac{3}{2}}])}{\alpha^2(V)[(\varphi_2 - \frac{eV}{2})^{\frac{1}{2}} - (\varphi_1 + \frac{eV}{2})^{\frac{1}{2}}]^2} \right) \times \sinh\left(\frac{3}{2}\alpha(V)[(\varphi_2 - \frac{eV}{2})^{\frac{1}{2}} - (\varphi_1 + \frac{eV}{2})^{\frac{1}{2}}]\frac{eV}{2}\right) \quad (\text{E2})$$

Where $\propto(v) = [4d(2m)^{1/2}]/[3\hbar(\varphi_1 + eV - \varphi_2)]$ and \hbar is the reduced Planck constant. The parameter values used to fit the downward and upward states are listed in [table E2](#).

Table E2. Input parameters used in eq. E2 of the manuscript to fit the downward and upward state of the current-voltage curve.

	ON state	OFF state
Barrier height 1 (φ_1) ¹	1.86 eV	2.75 eV
Barrier height 2 (φ_2) ¹	2.36 eV	2.20 eV
Layer thickness (d)	2.8 nm	
Electron mass (m)	$9.1094 \times 10^{-31} \text{Kg}$	
Electron charge (e)	$1.60217662 \times 10^{-19} \text{C}$	
Planck constant (\hbar)	$1.054571800 \times 10^{-34} \text{J} \cdot \text{s}$	

¹eV units of both potential barriers were converted to Joules (J)

References

- [1] F. Ambriz-Vargas, R. Thomas & A. Ruediger; Ferroelectric $(\text{Hf}, \text{Zr})\text{O}_2$ Thin Films for High-Density Nonvolatile Memories. *Springer Nature Singapore Pte Ltd.* **2018**, 124-133.
- [2] Fabian Ambriz-Vargas , G. Kolhatkar, M. Broyer, A. Hadj-Youssef, R. Nouar, A. Sarkissian, R. Thomas, C. Gomez-Yáñez, M. A. Gauthier & A. Ruediger, A Complementary Metal Oxide Semiconductor Process-Compatible Ferroelectric Tunnel Junction. *ACS Appl. Mater. Interfaces* **2017**, 9 (15), 13262–13268.
- [3] F. Ambriz-Vargas, G. Kolhatkar, R. Thomas, R. Nouar, A. Sarkissian, C. Gomez-Yáñez, M. A. Gauthier, & A. Ruediger, Tunneling electroresistance effect in a Pt/ $\text{Hf}_{0.5}\text{Zr}_{0.5}\text{O}_2$ /Pt structure. *Applied Physics Letters* **2017**, 110, 093106
- [4] F. Ambriz-Vargas, R. Nouar, G. Kolhatkar, A. Sarkissian, R. Thomas, C. Gomez-Yáñez, M.A. Gauthier, & A. Ruediger; RF-magnetron Sputtering Deposition of Ultra-thin $\text{Hf}_{0.5}\text{Zr}_{0.5}\text{O}_2$ films for non-volatile memory applications. *Materials Today: Proceedings* **2017**, 4 (7), 7000-7010.
- [5] F. Ambriz-Vargas, I. Velasco-Davalos, R. Thomas, & A. Ruediger; Nucleation and Growth of Ultrathin BaTiO_3 Films on Single Terminated $\text{Nb}:\text{SrTiO}_3$ (100) Substrates for Ferroelectric Tunnel Junction. *Journal of Vacuum Science & Technology B, Nanotechnology and Microelectronics: Materials, Processing, Measurement, and Phenomena* **2016**, 34 (2), 02M101.
- [6] F. Ambriz-Vargas, R. Nouar, B. Said, B. Higuera, R. Porter, A. Sarkissian, R. Thomas, & A. Ruediger; On-axis Radio Frequency Magnetron Sputtering of Stoichiometric BaTiO_3 Target: Localized Re-sputtering and Substrate Etching During Thin Film Growth. *Thin Solid Films* **2015**, 596, 77-82.
- [7] D. S. Jeong, R. Thomas, R. S. Katiyar, J. F. Scott, H. Kohlstedt, A. Petraru, & C.S. Hwang; Emerging Memories: Resistive Switching Mechanisms and Current Status. *Reports on Progress in Physics* **2012**, 75 (7), 076502.
- [8] A. I. Kingon, J.-P. Maria, & S. K. Streiffer; Alternative Dielectrics to Silicon Dioxide for Memory and Logic Devices. *Nature* **2000**, 406, 1032-1038.
- [9] A. Gruverman, D. Wu, H. Lu, Y. Wang, H. Jang, C. M. Folkman, M. Y. Zhuravlev, D. Felker, M. Rzchowski, C.-B. Eom, & E. Y. Tsymbal; Tunneling Electroresistance Effect in Ferroelectric Tunnel Junctions at the Nanoscale. *Nano letters* **2009**, 9 (10), 3539-3543.
- [10] A. Makarov, V. Sverdlov, & S. Selberherr; Emerging Memory Technologies: Trends, Challenges, and Modeling Methods. *Microelectronics Reliability* **2012**, 52 (4), 628-634.
- [11] P.J. Nair, C.-C. Chou, & M. K. Qureshi; Refresh Pausing in DRAM Memory Systems. *ACM Transactions on Architecture and Code Optimization* **2014**, 11 (1), 1-26.
- [12] L. Baldi, R. Bez, & G. Sandhu; Emerging Memories. *Solid-State Electronics* **2014**, 102, 2-11.
-

Reference

- [13] M. Joodaki; Selected Advances in Nanoelectronic Devices. *Springer Heidelberg New York Dordrecht London* **2013**, 5-24.
- [14] V. Garcia, & M. Bibes; Ferroelectric Tunnel Junctions for Information Storage and Processing. *Nature Communication* **2014**, 5, 4289.
- [15] E. Y. Tsymbal, & A. Gruverman; Ferroelectric Tunnel Junctions: Beyond the Barrier. *Nature Materials* **2013**, 12, 602-604.
- [16] E. Y. Tsymbal, & H. Kohlstedt; Applied Physics. Tunneling Across a Ferroelectric. *Science* **2006**, 313 (5784), 181-183.
- [17] V. Garcia, S. Fusil, K. Bouzehouane, S. Enouz-Vedrenne, N. D. Mathur, A. Barthelemy, & M. Bibes; Giant Tunnel Electroresistance for Non-destructive Readout of Ferroelectric States. *Nature* **2009**, 460 (7251), 81-84.
- [18] S. Boyn, S. Girod, V. Garcia, S. Fusil, S. Xavier, C. Deranlot, H. Yamada, C. Carrétéro, E. Jacquet, M. Bibes, A. Barthélémy, & J. Grollier; High-performance Ferroelectric Memory Based on Fully Patterned Tunnel Junctions. *Applied Physics Letters* **2014**, 104 (5), 10.1063.
- [19] H. Yamada, V. Garcia, S. Fusil, S. Boyn, M. Marinova, A. Gloter, S. Xavier, J. Grollier, E. Jacquet, C. Carretero, C. Deranlot, M. Bibes, & A. Barthelemy; Giant Electroresistance of Super-tetragonal BiFeO₃-Based Ferroelectric Tunnel Junctions. *American Chemical Society NANO* **2013**, 7, 5385-5390.
- [20] A. Chanthbouala, A. Crassous, V. Garcia, K. Bouzehouane, S. Fusil, X. Moya, J. Allibe, B. Dlbak, J. Grollier, S. Xavier, C. Deranlot, A. Moshar, R. Proksch, N. D. Mathur, M. Bibes, & A. Barthelemy; Solid-state Memories Based on Ferroelectric Tunnel Junctions. *Nature Nanotechnology* **2012**, 7 (2), 101-104.
- [21] H. J. Kim, M. H. Park, Y. J. Kim, Y. H. Lee, W. Jeon, T. Gwon, T. Moon, K.D. Kim, & C.S. Hwang; Grain Size Engineering for Ferroelectric Hf_{0.5}Zr_{0.5}O₂ Films by an Insertion of Al₂O₃ Interlayer. *Applied Physics Letters* **2014**, 105 (19), 192903.
- [22] M. H. Park, H. J. Kim, Y. J. Kim, W. Lee, T. Moon, & C. S. Hwang; Evolution of Phases and Ferroelectric Properties of Thin Hf_{0.5}Zr_{0.5}O₂ Films According to the Thickness and Annealing Temperature. *Applied Physics Letters* **2013**, 102 (24), 242905.
- [23] T. Shimizu, T. Yokouchi, T. Oikawa, T. Shiraishi, T. Kiguchi, A. Akama, T. J. Konno, & A. Gruverman; Funakubo, H., Contribution of Oxygen Vacancies to the Ferroelectric Behavior of Hf_{0.5}Zr_{0.5}O₂ Thin Films. *Applied Physics Letters* **2015**, 106 (11), 112904.
- [24] M. H. Park, H. J. Kim, Y. J. Kim, T. Moon, & C. S. Hwang; The Effects of Crystallographic Orientation and Strain of Thin Hf_{0.5}Zr_{0.5}O₂ Film on its Ferroelectricity. *Applied Physics Letters* **2014**, 104 (7), 072901.
- [25] A. Chernikova, M. Kozodaev, A. Markeev, D. Negrov, M. Spiridonov, S. Zarubin, O. Bak, P. Buragohain, H. Lu, E. Suvorova, A. Gruverman, & A. Zenkevich; Ultrathin Hf_{0.5}Zr_{0.5}O₂ Ferroelectric Films on Si. *ACS-Applied Material and Interfaces* **2016**, 8 (11), 7232-7237.

Reference

- [26] J. Muller, T. S. Boscke, U. Schroder, S. Mueller, D. Brauhaus, U. Bottger, L. Frey, & T. Mikolajick; Ferroelectricity in Simple Binary ZrO_2 and HfO_2 . *Nano Letters* **2012**, *12* (8), 4318-4323.
- [27] J. Müller, T. S. Böscke, U. Schröder, M. Reinicke, L. Oberbeck, D. Zhou, W. Weinreich, P. Kücher, M. Lemberger, & L. Frey; Improved Manufacturability of ZrO_2 MIM Capacitors by Process Stabilizing HfO_2 Addition. *Microelectronic Engineering* **2009**, *86* (7-9), 1818-1821.
- [28] X. Zhao, & D. Vanderbilt; First-principles Study of Structural, Vibrational, and Lattice Dielectric Properties of Hafnium Oxide. *Physical Review B* **2002**, *65* (23).
- [29] D.-Y. Cho, H.-S. Jung, & C. S. Hwang; Structural Properties and Electronic Structure of HfO_2 - ZrO_2 Composite Films. *Physical Review B* **2010**, *82* (9).
- [30] D. Pantel, & M. Alexe; Electroresistance Effects in Ferroelectric Tunnel Barriers. *Physical Review B* **2010**, *82* (13).
- [31] D. Pantel, H. Lu, S. Goetze, P. Werner, D. J. Kim, A. Gruverman, D. Hesse, & M. Alexe; Tunnel Electroresistance in Junctions with Ultrathin Ferroelectric $Pb(Zr_{0.2}Ti_{0.8})O_3$ Barriers. *Applied Physics Letters* **2012**, *100* (23), 232902.
- [32] T. Mikolajick, W. Hartner, I. Kasko, M.J. Kastner, N. Nagel, M. Moert, & C. Mazure; FeRAM Technology for High Density Applications. *Microelectronics Reliability* **2001**, *41*, 947-950.
- [33] H. Kohlstedt, Y. Mustafa, A. Gerber, A. Petraru, M. Fitsilis, R. Meyer, U. Böttger, & R. Waser; Current Status and Challenges of Ferroelectric Memory Devices. *Microelectronic Engineering* **2005**, *80*, 296-304.
- [34] Y. Noguchi, M. Miyayama, A. Hoshikawa, & T. Kamiyama; Ferroelectric Distortion and Electronic Structure in $Bi_4Ti_3O_{12}$. *Journal of Electroceramic* **2008**, *21*, 49-54.
- [35] N. Setter, D. Damjanovic, L. Eng, G. Fox, S. Gevorgian, S. Hong, A. Kingon, H. Kohlstedt, N.Y. Park, G. B. Stephenson, I. Stolitchnov, A. K. Taganstev, D. V. Taylor, T. Yamada, & S. Streiffer; Ferroelectric Thin Films: Review of Materials, Properties, and Applications. *Journal of Applied Physics* **2006**, *100* (5), 051606.
- [36] T. L. Qu, Y. G. Zhao, D. Xie, J.P. Shi, Q. P. Chen, & T. L. Ren; Resistance Switching and White-light Photovoltaic Effects in $BiFeO_3/Nb-SrTiO_3$ Heterojunctions. *Applied Physics Letters* **2011**, *98* (17), 173507.
- [37] D. H. Kwon, K. M. Kim, J. H. Jang, J. M. Jeon, M. H. Lee, G. H. Kim, X. S. Li, G. S. Park, B. Lee, S. Han, M. Kim, & C. S. Hwang; Atomic Structure of Conducting Nanofilaments in TiO_2 Resistive Switching Memory. *Nature Nanotechnology* **2010**, *5* (2), 148-53.
- [38] A. Sawa; Resistive Switching in Transition Metal Oxides. *Materials Today* **2008**, *11* (6), 28-36.
- [39] The International Technology Roadmap for Semiconductors 2.0, 2015 edition (Beyond CMOS). Emerging Research Devices, **2015** 14-15.
-

Reference

- [40] X. Liu; Ferroelectric Polarization Dependent Interface Effects (doctoral diseration). University of Nebraska (*Nebraska, United States of America, 3667012*) **2014**, 1-12.
- [41] X. Lu, H. Li, & W. Cao; Current-voltage Characteristics and ON/OFF Ratio in Ferroelectric Tunnel Junctions. *Journal of Applied Physics* **2012**, *112* (5), 054102.
- [42] I. D. Bilc, J. Iniguez, P. Ordejon, & P. Ghosez; Electroresistance Effect in Ferroelectric Tunnel Junctions with Symmetric Electrodes. *American Chemical Society NANO* **2012**, *6*, 1473–1478.
- [43] L. Wang, M. R. Cho, Y. J. Shin, J. R. Kim, S. Das, J.-G. Yoon, J.-S. Chung, & T. W. Noh; Overcoming the Fundamental Barrier Thickness Limits of Ferroelectric Tunnel Junctions Through BaTiO₃/SrTiO₃ Composite Barriers. *Nano letters* **2016**, *16*, 3911-3918.
- [44] A. Crassous, V. Garcia, K. Bouzehouane, S. Fusil, A. H. G. Vlooswijk, G. Rispens, B. Noheda, M. Bibes, & A. Barthélémy; Giant Tunnel Electroresistance with PbTiO₃ Ferroelectric Tunnel Barriers. *Applied Physics Letters* **2010**, *96* (4), 042901.
- [45] I. Velasco-Davalos, F. Ambriz-Vargas, C. Gómez-Yáñez, R. Thomas, & A. Ruediger; Polarization Reversal in BaTiO₃ Nanostructures Synthesized by Microwave-assisted Hydrothermal Method. *Journal of Alloys and Compounds* **2016**, *667*, 268-274.
- [46] I. A. Velasco-Davalos, A. Ruediger, J. J. Cruz-Rivera, & C. Gomez-Yanez; Mechanical Niobium Doping in Barium Titanate Electroceramics. *Journal of Alloys and Compounds* **2013**, *581*, 56-58.
- [47] I. Velasco-Davalos, F. Ambriz-Vargas, G. Kolhatkar, R. Thomas, & A. Ruediger; Synthesis of BiFeO₃ Thin Films on Single-terminated Nb:SrTiO₃ (111) Substrates by Intermittent Microwave Assisted Hydrothermal Method. *AIP-Advances* **2016**, *6* (6), 065117.
- [48] I. A. Velasco-Davalos, M. Moretti, M. Nicklaus, C. Nauenheim, S. Li, R. Nechache, C. Gomez-Yanez, & A. Ruediger; Polar Properties of Hydrothermally Synthesized BiFeO₃ Thin Films. *Applied Physics A* **2013**, *115* (3), 1081-1085.
- [49] K. J. Choi, M. Biegalski, Y. L. Li, A. Sharan, J. Schubert, R. Uecker, P. Reiche, Y. Chen, W. Q. Pan, V. Gopalan, L.-Q. Chen, D. G. Schlom, & C. B. Eom; Enhancement of Ferroelectricity in Strained BaTiO₃ Thin Films. *Science* **2004**, *306*, 1005-1008.
- [50] H. Lu, A. Lipatov, S. Ryu, D. J. Kim, H. Lee, M. Y. Zhuravlev, C. B. Eom, E. Y. Tsymbal, A. Sinitskii, & A. Gruverman; Ferroelectric Tunnel Junctions with Graphene Electrodes. *Nature Communications* **2014**, *5*, 5518.
- [51] R. Soni, A. Petraru, P. Meuffels, O. Vavra, M. Ziegler, S. K. Kim, D. S. Jeong, N. A. Pertsev, & H. Kohlstedt; Giant Electrode Effect on Tunnelling Electroresistance in Ferroelectric Tunnel Junctions. *Nature Communications* **2014**, *5*, 5414.
- [52] H. Kohlstedt, N. A. Pertsev, J. Rodríguez Contreras, & R. Waser; Theoretical Current-voltage Characteristics of Ferroelectric Tunnel Junctions. *Physical Review B* **2005**, *72* (12).

Reference

- [53] R. Materlik, C. Künneth, & A. Kersch; The Origin of Ferroelectricity in $\text{Hf}_{1-x}\text{Zr}_x\text{O}_2$: A Computational Investigation and a Surface Energy Model. *Journal of Applied Physics* **2015**, *117* (13), 134109.
- [54] L. W. Martin, Y. H. Chu, & R. Ramesh; Advances in the Growth and Characterization of Magnetic, Ferroelectric, and Multiferroic Oxide Thin Films. *Materials Science and Engineering: R: Reports* **2010**, *68* (4-6), 89-133.
- [55] Q. Li; Nucleation and Growth of Metastable Phases in Thin Films (doctoral diseration). *Northwestern univerversity (Illinois-United States of America, 3033521)* **2001**, 9-26.
- [56] H. Lu; Polarization-coupled Transport Behavior in Ultrathin Ferroelectric Heterostructuers (doctoral diseration). *University of Nebraska (Nebraska-United States of America, 3604645)* **2013**, 21-45.
- [57] D. Wu; Nanoscale Studies of Switching Behavior of Ferroelectric Thin Films by Using Piezoresponse Force Microscopy. *Raleigh, North Carolina* **2009**, 44-50.
- [58] F. Peter; Piezoresponse Force Microscopy and Surface Effects of Perovskite Ferroelectric Nanostructures. *Forschungszentrum Jülich GmbH* **2006**, 5-42.
- [59] L. Ramirez; Nucleation and Growth of Thin Film Zirconia using Pulsed Pressure Metal-Organic Chemical Vapor Deposition (doctoral diseration). *University of california (California-United States of America, 3296275)* **2008**, 1-13.
- [60] H. Kim; Nano-scale Zirconia and Hafnia Dielectrics Grown by Atomic Layer Deposition: Crystallinity, Interface Structures and Electrical Properties (doctoral diseration). *Stanford university (California-United States of America, 3128661)* **2004**, 13-15.
- [61] Y.-S. Lin; Synthesis, Integration, and Characterization of Metal Oxide Films as Alternative Gate Dielectric Materials (doctoral diseration). *University of California (California-United States of America, 3121260)* **2003**, 12-19.
- [62] M. N. U. Bhuyian; Reliability Study of Zr and Al Incorporated Hf Based High-k Dielectric Deposited by Advanced Processing (doctoral diseration). *New Jersey Institute of Technology (New Jersey-United States of America, 10170455)* **2015**, 39-43.
- [63] Y. W. Lu, J. Shieh, & F. Y. Tsai; Induction of Ferroelectricity in Nanoscale $\text{ZrO}_2/\text{HfO}_2$ Bilayer Thin Films on Pt/Ti/SiO₂/Si Substrates. *Acta Materialia* **2016**, *115*, 68-75.
- [64] M. H. Park, Y. H. Lee, H. J. Kim, Y. J. Kim, T. Moon, K. D. Kim, J. Muller, A. Kersch, U. Schroeder, T. Mikolajick, & C. S. Hwang; Ferroelectricity and Antiferroelectricity of Doped Thin HfO₂-based Films. *Advanced Materials* **2015**, *27* (11), 1811-31.
- [65] J. Müller, T. S. Böscke, D. Bräuhaus, U. Schröder, U. Böttger, J. Sundqvist, P. Kücher, T. Mikolajick, & L. Frey; Ferroelectric $\text{Zr}_{0.5}\text{Hf}_{0.5}\text{O}_2$ Thin Films for Nonvolatile Memory Applications. *Applied Physics Letters* **2011**, *99* (11), 112901.
- [66] T. S. Böscke, J. Müller, D. Bräuhaus, U. Schröder, & U. Böttger; Ferroelectricity in Hafnium Oxide Thin Films. *Applied Physics Letters* **2011**, *99* (10), 102903.

Reference

- [67] W. Lu, J. X. Lu, X. Ou, X. J. Liu, Y. Q. Cao, A. D. Li, B. Xu, Y. D. Xia, J. Yin, & Z. G. Liu; Determination of the Density of the Defect States in $\text{Hf}_{0.5}\text{Zr}_{0.5}\text{O}_2$ High-k Film Deposited by Using RF-magnetron Sputtering Technique. *AIP-Advances* **2014**, *4* (8), 087114.
- [68] T. S. Böscke, P. Y. Hung, P. D. Kirsch, M. A. Quevedo-Lopez, & R. Ramírez-Bon; Increasing Permittivity in HfZrO Thin Films by Surface Manipulation. *Applied Physics Letters* **2009**, *95* (5), 052904.
- [69] M. H. Park, H. J. Kim, Y. J. Kim, W. Lee, H. K. Kim, & C. S. Hwang; Effect of Forming Gas Annealing on the Ferroelectric Properties of $\text{Hf}_{0.5}\text{Zr}_{0.5}\text{O}_2$ Thin Films with and without Pt Electrodes. *Applied Physics Letters* **2013**, *102* (11), 112914.
- [70] Y. Yan, D. Zhou, C. Guo, J. Xu, X. Yang, H. Liang, F. Zhou, S. Chu, & X. Liu; Thickness-dependent Phase Evolution and Dielectric Property of $\text{Hf}_{0.5}\text{Zr}_{0.5}\text{O}_2$ Thin Films Prepared with Aqueous Precursor. *Journal of Sol-Gel Science and Technology* **2015**, *77* (2), 430-436.
- [71] F. Fang; Band Alignment Measurements at Heterojunction Interfaces in Layered Thin Film Solar Cells & Thermoelectrics (doctoral diseration). *University of Delaware (Delaware-United States of America, 3473682)* **2011**, 6-11.
- [72] S. M. Sze, & N. K. Kwok; Physics of Semiconductor Devices (Book, 3^{er} edition). *WiLey-Intercience (A John Wiley & Sons, inc , publications, ISBN-13: 978-0471-14323-9)* **2007**, 417-466.
- [73] A. Zaman; Characterization of Tantalum Nitride Thin Films Synthesized by Magnetron Sputtering (master dissertation). *The university of texas (Texas-United States of America, 1561888)* **2014**, 13-17.
- [74] A. Mirfazli; Characterization of Piezoelectric AlN Thin Films Deposited on Si by RF reactive Magnetron Sputtering at Low Temperature For Acoustic Wave Devices (master dissertation). *Carleton University (Ontario-Canada)* **2004**, 19-32.
- [75] L. Kuerten; Observation of Natural Domain Structure in Ferroelectric Superlattices by Piezoresponse Force Microscopy (master dissertation). *Stony Brook University (New-york-United States of America, 1529594)* **2012**, 15-17.
- [76] C. Liang; X-ray Reflectivity Studies on Polystyrene Dead Layers (master dissertation). *Stony Brook University (New-york-United States of America, 1515685)* **2012**, 4-7.
- [77] F. A. Chowdhury; Analysis of Multilayer Structure of Piezoelectric Thin Film by X-ray Diffraction (master dissertation). *The university of Texas (Texas-United States of America, 1605159)* **2015**, 6-12.
- [78] J. K. Hulm; Dielectric Properties of Single Crystals of Barium Titanate. *Nature* **1947**, *160*, 127-128.
- [79] R. Thomas, D. C. Dube, M. N. Kamalasan, & S. Chandra; Optical and Electrical Properties of BaTiO_3 Thin Films Prepared by Chemical Solution Deposition. *Thin Solid Films* **1999**, *346* (1-2), 212-225.

- [80] M. Y. Zhuravlev, R. F. Sabirianov, S. S. Jaswal, & E. Y. Tsymbal; Giant Electroresistance in Ferroelectric Tunnel Junctions. *Physical Review Letters* **2005**, *94* (24), 246802.
- [81] B. B. Tian, J. L. Wang, S. Fusil, Y. Liu, X. L. Zhao, S. Sun, H. Shen, T. Lin, J. L. Sun, C. G. Duan, M. Bibes, A. Barthelemy, B. Dkhil, V. Garcia, X. J. Meng, & J. H. Chu; Tunnel Electroresistance Through Organic Ferroelectrics. *Nature Communications* **2016**, *7*, 11502.
- [82] J. Mannhart, & D. G. Schlom; Oxide Interfaces-An Opportunity for Electronics. *Science* **2010**, *327* (5973), 1607-1611.
- [83] D. G. Schlom, & L. N. Pfeiffer; Oxide Electronics Upward mobility rocks. *Nature Materials* **2010**, *9* (11), 881-883.
- [84] E. Y. Tsymbal, A. Gruverman, V. Garcia, M. Bibes, & A. Barthélémy; Ferroelectric and Multiferroic Tunnel Junctions. *Materials Research Society Bulletin* **2012**, *37*, 138-143.
- [85] S. Boyn, A. M. Douglas, C. Blouzon, P. Turner, A. Barthelemy, M. Bibes, S. Fusil, J. M. Gregg, & V. Garcia; Tunnel Electroresistance in BiFeO₃ Junctions: Size Does Matter. *Applied Physics Letters* **2016**, *109*, 232902.
- [86] C. Dubourdieu, J. Bruley, T. M. Arruda, A. Posadas, J. Jordan-Sweet, M. M. Frank, E. Cartier, D. J. Frank, S. V. Kalinin, A. A. Demkov, & V. Narayanan; Switching of Ferroelectric Polarization in Epitaxial BaTiO₃ Films on Silicon without a Conducting Bottom Electrode. *Nature Nano* **2013**, *8* (10), 748-754.
- [87] D. J. Kester, & R. Meissier; Micro-effects of Resputtering due to Negative Ion Bombardment of Growing Thin Films. *Journal of Material Research* **1993**, *8*, 1938-1957.
- [88] Rainer Waser; *Nanoelectronics and Information Technology – Advanced Electronic Materials and Novel Devices (Film Deposition Methods)*. Wiley-VCH, Weinheim **2003**, 201-221.
- [89] I. Velasco-Davalos, R. Thomas, & A. Ruediger; Realization of Single-Termination SrTiO₃ (100) Surfaces by a Microwave-induced Hydrothermal Process. *Applied Physics Letters* **2013**, *103* (20), 202905.
- [90] Y. Shintani, K. Nakanishi, T. Takawaki, & O. Tada; Behaviours of High-Energy Electrons and Neutral Atoms in the Sputtering of BaTiO₃. *Journal of applied physics*. **1975**, *14*, 1875.
- [91] K. Tominaga, S. Iwamura, & Y. Shintani; Energy Analysis of High-Energy Neutral Atoms in the Sputtering of ZnO and BaTiO₃. *Japanese Journal of Applied Physics* **1982**, *21*, 688.
- [92] C. F. A. Os, & P. W. Amersfoort; Negative Ion Formation at a Barium Surface Exposed to an Intense Positive-hydrogen Ion Beam. *Journal of applied physics*. **1988**, *64*, 3863.
- [93] K. Ohya, K. Ishida, & I. Mori; Production of Atomic Oxygen Negative Ionbeam by Positive Ion-induced Sputtering of Semiconductive BaTiO₃ Ceramic. *Japanese Journal of Applied Physics* **1984**, *23*, 1640-1646.

- [94] J. J. Cuomo, R. J. Gambino, J. M. E. Harper, J. D. Kuptsis, & J. C. Webber; Significance of Negative Ion Formation in Sputtering and SIMS Analysis. *Journal of Vacuum Science and Technology* **1978**, *15*, 281-287.
- [95] R. A. York, A. S. Nagra, P. Periaswamy, O. Auciello, S. K. Streiffer, & J. Imb; Synthesis and Characterization of $(\text{Ba}_x\text{Sr}_{1-x})\text{Ti}_{1+y}\text{O}_{3+z}$ Thin Films and Integration Into Microwave Varactors and Phase shifters. *Integrated Ferroelectrics* **2001**, *34*, 177-188.
- [96] N. Matsunami, Y. Yamamura, Y. Itikawa, N. Itoh, Y. Kazumata, S. Miyagawa, K. Morita, R. Shimizu, & H. Tawara; Energy Dependence of the Ion-induced Sputtering yields of monatomic Solids. *Atomic Data and Nuclear Data Tables* **1984**, *31* (1), 1-80.
- [97] Z. Wen, C. Li, D. Wu, A. Li, & N. Ming; Ferroelectric-field-effect-enhanced Electroresistance in Metal/Ferroelectric/Semiconductor Tunnel Junctions. *Nature Materials* **2013**, *12* (7), 617-621.
- [98] Y. S. Kim, D. H. Kim, J. D. Kim, Y. J. Chang, T. W. Noh, J. H. Kong, K. Char, Y. D. Park, S. D. Bu, & J. -S. Yoon; Critical Thickness of Ultrathin Ferroelectric BaTiO_3 films. *Applied Physics Letters* **2005**, *86* (10), 102907.
- [99] D. A. Tenne, A. Bruchhausen, N. D. Lanzillotti-Kimura, A. Fainstein, R. S. Katiyar, A. Cantarero, A. Soukiassian, V. Vaithyanathan, J. H. Haeni, W. Tian, D. G. Schlom, K. Choi, D. M. Kim, C. B. Eom, H. P. Sun, X. Pan, Y. L. Li, L. Q. Chen, Q. X. Jia, S. M. Nakmanson, K. Rabe, & X. X. Xi; Probing Nanoscale Ferroelectricity by Ultraviolet Raman Spectroscopy. *Science* **2006**, *313* (5793), 1614-6.
- [100] J. Shin, S. V. Kalinin, A. Y. Borisevich, E. W. Plummer, & A. P. Baddorf; Layer-by-layer and Pseudo-two-dimensional Growth Modes for Heteroepitaxial BaTiO_3 Films by Exploiting Kinetic Limitations. *Applied Physics Letters* **2007**, *91* (20), 202901.
- [101] S. Boyn, V. Garcia, S. Fusil, C. Carrétéro, K. Garcia, S. Xavier, S. Collin, C. Deranlot, M. Bibes, & A. Barthélémy; Engineering Ferroelectric Tunnel Junctions Through Potential Profile Shaping. *APL materials* **2015**, *3*, 061101.
- [102] J. Junquera & P. Ghosez; Critical Thickness for Ferroelectricity in Perovskite Ultrathin Films. *Nature* **2003**, *422*, 506-509.
- [103] J. Wu, & J. Wang; BiFeO_3 Thin Films of (111)-orientation Deposited on SrRuO_3 Duffered $\text{Pt}/\text{TiO}_2/\text{SiO}_2/\text{Si}(100)$ Substrates. *Acta Materialia* **2010**, *58* (5), 1688-1697.
- [104] C. S. Consiglio, G. Nakamura, R.D. Clark, S. Aoyama & G. J. Leusink; Physical an Electrical Properties of MOCVD grown HfZrO_4 High-k Thin Films Deposited in a Production-Worthy 300 mm Deposition System. *ECS transactions* **2010**, *2010* (1), 125-135.
- [105] A. Zenkevich, M. Minnekaev, Y. Matveyev, Y. Lebedinskii, K. Bulakh, A. Chouprak, A. Baturin, K. Maksimova, S. Thiess, & W. Drube; Electronic Band Alignment and Electron Transport in $\text{Cr}/\text{BaTiO}_3/\text{Pt}$ Ferroelectric Tunnel Junctions. *Applied Physics Letters* **2013**, *102* (6), 062907.

Reference

- [106] E. A. Kraut, J. R. Waldrop, & S. P. Kowalczyk; Precise Determination of the Valence-Band Edge in X-Ray Photoemission Spectra: Application to Measurement of Semiconductor Interface Potentials. *Physics review letters* **1980**, *44*, 1620.
- [107] E. A. Kraut, J. R. Waldrop, & S. P. Kowalczyk; Semiconductor Core-level to Valence-band Maximum Binding-energy Differences: Precise Determination by X-ray Photoelectron Spectroscopy. *Physic Review B* **1983**, *28*, 1965.
- [108] J. G. Simmons; Generalized Formula for the Electric Tunnel Effect between Similar Electrodes Separated by a Thin Insulating Film. *Journal of Applied Physics* **1963**, *34* (6), 1793.
- [109] S. P. Pavunny, R. Thomas, A. Kumar, E. Fachini, & R. S. Katiyar; Optical Properties of Amorphous High-k LaGdO₃ Films and its Band Alignment with Si. *Journal of Applied Physics* **2012**, *111* (4), 044106.
- [110] S. P. Pavunny, R. Thomas, A. Kumar, J. F. Scott, & R. S. Katiyar; Optical Dielectric Function Modeling and Electronic Band Lineup Estimation of Amorphous High-k LaGdO₃ Films. *ECS Journal of Solid State Science and Technology* **2012**, *1* (4), N53-N57.
- [111] W. F. Brinkman; Tunneling Conductance of Asymmetrical Barriers. *Journal of Applied Physics* **1970**, *41* (5), 1915.
- [112] A. Gruverman, B. J. Rodriguez, C. Dehoff, J. D. Waldrep, A. I. Kingon, R. J. Nemanich, & J. S. Cross; Direct Studies of Domain Switching Dynamics in Thin Film Ferroelectric Capacitors. *Applied Physics Letters* **2005**, *87* (8), 082902.
- [113] P. Hou, J. Wang, & X. Zhong; Investigation of Multilevel Data Storage in Silicon-Based Polycrystalline Ferroelectric Tunnel Junction. *Scientific reports* **2017**, *7* (1), 4525.
- [114] J. Q. Li, Y. Xiong, M. H. Tang, H. X. Guo, W. Zhao, Y. G. Xiao, Z. H. Tang, S. A. Yan, W. L. Zhang, Y. C. Zhou, F. Yang, & J. He; Simulation of Multilevel Polarization in Ferroelectric Tunnel Junctions. *Physica status solidi (B)* **2014**, *251* (2), 469-473.
- [115] C. Li, L. Huang, T. Li, W. Lu, X. Qiu, Z. Huang, Z. Liu, S. Zeng, R. Guo, Y. Zhao, K. Zeng, M. Coey, J. Chen, T. Venkatesan; Ultrathin BaTiO₃-Based Ferroelectric Tunnel Junctions Through Interface Engineering. *Nano Letters* **2015**, *15* (4), 2568-73.
- [116] ASTM standard E 2108-00, Standard Practice for Calibration of the Electron Binding-Energy Scale of an X-ray Photoelectron Spectrometer. **2000**, 1 to 16.

Abbreviations

AC	Alternating current
AFM	Atomic force microscopy
ALD	Atomic layer deposition
BE	Bottom electrode
C-AFM	Conductive-atomic force microscopy
CMOS	Complementary metal-oxide semiconductor
CPU	Central processing unit
DC	Direct current
DRAM	Dynamic random access memory
ϵ	Dielectric permittivity
EEPROM	Electrically erasable programmable read-only memory
E_c	Conduction band
E_g	Band gap
EPROM	Erasable programmable read-only memory
$I-V$	Current-voltage
F	Feature size
Fe	Ferroelectric

Abbreviations

FeRAM	Ferroelectric random access memory
FTJ	Ferroelectric tunnel junction
GIXRD	Glancing incidence X-ray diffraction
HRS	High resistance state
LRS	Low resistance state
MRAM	Magnetoresistive random access memory
MRD	Materials research diffractometer
MOCVD	Metal-organic chemical vapor deposition
OES	Optical emission spectroscopy
OTPROM	One time programmable read only memory
PCRAM	Phase change random access memory
P-E loop	Polarization-electric field loop
PFM	Piezoresponse force microscopy
PLD	Pulsed laser deposition
<i>Po</i>	Oxygen partial pressure
<i>Pr</i>	Remanent polarization
PZT	Lead zirconate titanate
RAM	Random access memory

Abbreviations

ReRAM	Resistive random access memory
rms	Root mean square
RF	Radio frequency
ROM	Read only memory
sccm	Standard cubic centimeter per minute
SRAM	Static random access memory
TER	Tunneling electrosistance effect
TM	Melting temperature
U	Barrier height energy
u.c.	Unit cell
VBM	Valence band maximum
VBO	Valence band offset
WKB	Wentzel-Kramer-Brillouin
XRD	X-ray diffraction
XRR	X-ray reflectivity
XPS	X-ray photoelectron spectroscopy

Résumé en Français

UN DISPOSITIF MÉMOIRE FERROÉLECTRIQUE À JONCTION TUNNEL COMPATIBLE AVEC LA TECHNOLOGIE CMOS

1 INTRODUCTION	112
1.1 Objectifs de recherche.....	115
1.2 Objectifs spécifiques.....	115
2 MÉTHODOLOGIE	117
2.1 Fabrication des heterostructures Nb:SrTiO ₃ /BaTiO ₃	117
2.2 Fabrication des dispositifs mémoires ferroélectrique à jonction tunnel nominalement symétriques.....	118
2.3 Fabrication des dispositifs mémoires ferroélectrique à jonction tunnel asymétriques.....	119
3 ANALYSE ET RESULTATS	122
3.1 Mécanisme de croissance du BaTiO ₃ sur un substrat de Nb:SrTiO ₃	122
3.2 Caractérisation de la ferroélectricité des couches ultraminces de BaTiO ₃	124
3.3 Caractérisation de la ferroélectricité des couches ultraminces de Hf _{0.5} Zr _{0.5} O ₂	125
3.4 Propriétés électroniques des dispositifs mémoires FTJ asymétriques et nominalement symétriques.....	127
3.5 Électroresistance à effet tunnel dans les mémoires FTJ nominalement symétriques.....	128
3.6 Électroresistance à effet tunnel dans les mémoires FTJ nominalement asymétriques.....	131
4 CONCLUSION	134

1. INTRODUCTION

Les récents progrès technologiques dans les techniques de la nano- et la micro- fabrication ont permis de mettre sur le marché une nouvelle génération d'appareils électroniques tels que des ordinateurs, cellulaires, caméras, tablettes, etc.⁷⁻⁹ En plus d'être de plus en plus fin et légers, ces appareils possèdent davantage de mémoire de stockage, sont plus rapide, et sont équipés de capteurs optique et d'écrans ayant une résolution supérieure à la génération précédente. Comme prédict par la loi de Moore, une nouvelle génération de dispositifs électroniques est mise sur le marché tous les deux ans depuis quatre décennies. Cette tendance a conduit le public à s'attendre à des appareils toujours plus puissants et moins chers. Cependant, cela pourrait cesser, si l'industrie électronique continue de travailler avec la technologie actuelle de mémoire à semi-conducteurs.¹⁰

Le problème principal des dispositifs électroniques actuels est qu'ils reposent sur une combinaison de mémoires à semi-conducteurs qui ont déjà atteint leurs limites physiques.¹²⁻¹³ En général, le processeur dans l'unité centrale de traitement (CPU – *Central Processing Unit*) des ordinateurs est accompagné par une séries de mémoires technologiques (voir la hiérarchie de mémoires dans le [Tableau 1](#)).⁷ La mémoire la plus proche du CPU est appelée « mémoire cache ». Elle est composée de mémoire statique (SRAM – *Static Random Access Memory*). Elle est très rapide (temps d'écriture / d'effacement : 0,3 ns / 0,3 ns) mais est relativement volumineuse (six transistors avec des cellules de taille minimale qui correspond à $140F^2$; où F est la taille minimale que prend un transistor sur la puce). Étant donné leurs propriétés physiques, les SRAMs permettent au processeur d'accéder rapidement aux instructions et aux données.⁷ Le niveau suivant de la hiérarchie de mémoires est la « mémoire primaire » qui est composée de mémoires dynamique (DRAM – *Dynamic Random Access Memory*). Comparativement à la SRAM, cette mémoire est plus compacte (un transistor et une capacité, avec une cellule de taille $6F^2$) mais est aussi plus lente (temps d'écriture / d'effacement 10ns / 10ns).⁷ Les propriétés physiques de la DRAM, lui permettent d'atteindre une densité élevée dans une puce mémoire. La « mémoire primaire » est utilisée pour stocker temporairement les informations issues de la « mémoire secondaire » (disque dur).⁷ Dans les cas deux cas, les mémoires « cache » et « primaires » sont volatiles (les informations stockées sont perdues quand l'alimentation est coupée). La « mémoire secondaire » est de plus en plus constitué de mémoire flash, non-volatile (les informations sont conservées quand

l'alimentation est coupée). Comparativement à la « mémoire primaire », elle est très lente (temps d'écriture / d'effacement: 1ms / 10ms).^{7,10}

Comme on l'a vu, les mémoires dominantes dans les dispositifs électroniques modernes, sont les DRAM, les SRAM et les mémoires flash.^{8-9, 11-12} Ces trois types de mémoires stockent les données comme un état de charge. Pendant plusieurs décennies, ces technologies de mémoires ont été miniaturisées avec succès, ce qui a permis d'atteindre des vitesses plus élevées et d'augmenter la densité des puces mémoires à moindre coût. Cependant, ces technologies approchent de leurs limites physiques de miniaturisation.^{8,11,13} C'est pour cela que le progrès technologique de technologies de stockage nécessite la mise au point d'une mémoire universelle pouvant remplacer tous les autres types de mémoires. Cette mémoire universelle doit combiner à la fois la nature non-volatile du flash, la densité d'information de la DRAM, les vitesses élevées de la SRAM, et la haute endurance de la DRAM et de la SRAM (Tableau 1).^{7,12}

Tableau 1. Hiérarchie et propriétés. Les données sont issues de la référence [7]

HIÉRARCHIE DE MÉMOIRES		PROPRIÉTÉS DES MÉMOIRES			
Processeur (CPU)	Vitesse (temps d'écriture / d'effacement)	Scalabilité (Taille d'un bit de données)	Endurance (Cycles)	Efficacité énergétique	
Mémoire cache	✓ HAUTE (0.3ns/0.3ns)	✗ FAIBLE (140F ²)	✓ HAUTE (10 ¹⁶)	✗ VOLATILE	
Mémoire principale	✓ HAUTE (10ns/10ns)	✓ HAUTE (6F ²)	✓ HAUTE (10 ¹⁶)	✗ VOLATILE	
Mémoire principale	✗ FAIBLE (1ms/10ms)	✓ HAUTE (10F ²)	✗ FAIBLE (10 ⁵)	✓ NON-VOLATILE	
Mémoire universelle	✓ HAUTE	✓ HAUTE	✓ HAUTE	✓ NON-VOLATILE	

Récemment, l'émergence de mémoires à semi-conducteurs utilisant d'autres approches physiques pourrait permettre d'obtenir les une mémoire avec les avantages de la DRAM, de la SRAM et de la mémoire flash.^{7,12} Parmi les différents nouveaux types de mémoires, le plus sérieux candidat au titre de mémoire universelle est la mémoire ferroélectrique à jonction tunnel (FTJ – *Ferroelectric Tunnel Junction*).

Un dispositif mémoire FTJ est composé de deux électrodes métalliques séparées par une couche mince ferroélectrique nanométrique (1 à 3 nm d'épaisseur).¹⁴⁻¹⁶ Le concept physique de ces mémoires est basé sur l'électrorésistance à effet tunnel (TER – *Tunneling ElectroResistance*). Ce phénomène permet de moduler l'état de la résistance électrique d'une mémoire FTJ à l'aide d'un champ électrique de manière réversible.¹⁴⁻¹⁶ Cette modulation est à l'origine de l'apparition de deux états stables (un état de haute résistance (HRS – *High Resistance State*) et un état de basse résistance (LSR – *Low Resistance State*)) qui peuvent être codés en états binaires "1" et "0".¹⁴⁻¹⁶

L'effet TER a été mis en évidence pour la première fois en 2009 par M. Bibes (*Nature Letters*)¹⁷ et A. Gruverman (*Nanoletters*).⁹ Dans les deux cas, des couches ultraminces de titanate de baryum (BaTiO_3) ont été utilisées comme couche ferroélectrique. Ces travaux ont déclenché d'intenses recherches sur les propriétés des mémoires FTJ. Ceci a permis de démontrer que ces mémoires peuvent posséder plusieurs avantages, tels qu'une haute endurance ($\sim 10^6$ cycles),¹⁸⁻¹⁹ une grande vitesse de fonctionnement (les états "ON/OFF" peuvent être écrits par des impulsions électriques de durée inférieure à 10 ns),²⁰ une importante densité de données¹⁵ et simple architecture.¹⁴

Malgré les excellentes propriétés des mémoires FTJ, leur introduction dans le marché des semi-conducteurs reste restreinte car l'intégration de ces mémoires composées d'une couche ultramine ferroélectrique (ayant une structure pérovskite) dans la technologie du silicium reste un défi pour de nombreuses raisons. Par exemple, la mauvaise qualité des interfaces avec le silicium ou la haute température de cristallisation de la couche ferroélectrique provoquant une dégradation des performances des autres structures fabriquées en utilisant les procédés standards (CMOS – *Complementary Metal-Oxide Semiconductor*).²¹⁻²⁴

En 2012, J. Müller *et al.*²⁵ ont découvert les propriétés ferroélectriques des couches ultraminces d'oxyde d'hafnium-zirconium ($\text{Hf}_{0.5}\text{Zr}_{0.5}\text{O}_2$; ~7,5 nm d'épaisseur). Cela fut une surprise car les oxydes d'hafnium (HfO_2) et de zirconium (ZrO_2) macroscopiques sont étudiés depuis plus d'un siècle.²⁶ Ces résultats ont permis de considérer que la ferroélectricité des couches ultraminces de $\text{Hf}_{0.5}\text{Zr}_{0.5}\text{O}_2$ permettra de résoudre les problèmes de compatibilité des mémoires FTJ avec le procédé CMOS. En effet, le $\text{Hf}_{0.5}\text{Zr}_{0.5}\text{O}_2$ est la combinaison du HfO_2 et du ZrO_2 , tous deux déjà utilisés par l'industrie des semi-conducteurs comme matériau diélectrique dans les

transistors et les capacités de la DRAM.²⁶⁻²⁹ Par conséquent, une mémoire FTJ utilisant le Hf_{0.5}Zr_{0.5}O₂ pourraient être compatibles avec le procédé CMOS.

Pour introduire les mémoires FTJ dans le marché des semi-conducteurs, il est nécessaire d'étudier en premier le mécanisme de transport de charges électroniques dans ce type de dispositifs.¹⁴ Plus spécifiquement, une étude approfondie des relations entre les propriétés de l'interface ferroélectrique/métal et le transport de charges doit être effectuée, afin d'optimiser les performances des dispositifs mémoires FTJ.¹⁴

Par conséquent, une étude des interfaces ferroélectrique/métal avec des techniques de caractérisations telles que la spectroscopie UV-Visible et la spectrométrie de photoélectrons induits par rayons X (XPS – *X-ray photoelectron spectrometry*) associées à des modèles théoriques peuvent apporter de nouvelles informations pour mieux comprendre les dispositifs FTJ.¹⁴

1.1 OBJECTIFS DE RECHERCHE

L'objectif principal de cette thèse est d'étudier la faisabilité d'une jonction tunnel ferroélectrique à base de Hf_{0.5}Zr_{0.5}O₂ compatible avec la technologie CMOS

1.2 OBJECTIFS SPECIFIQUES

Pour accomplir l'objectif décrit ci-dessus, ce travail est divisé en trois objectifs spécifiques :

1. L'optimisation des paramètres de dépôt de l'électrode inférieure (nitrate de titane – TiN), de la couche ferroélectrique ultramince (Hf_{0.5}Zr_{0.5}O₂), ainsi que de l'électrode supérieure (platine) par pulvérisation cathodique magnétron. Les paramètres de cette optimisation comprennent l'épaisseur, la stoechiométrie et la cristallinité en fonction de la température de dépôt.
2. La démonstration expérimentale de l'électrorésistance à effet tunnel, incluant une étude détaillée des propriétés des interfaces ferroélectrique/métal d'un dispositif mémoire ferroélectrique à jonction tunnel.
3. La quantification des propriétés des mémoires ferroélectrique à jonction tunnel : rapport ON/OFF, endurance, rétention de l'information et reproductibilité.

2. MÉTHODOLOGIE

Cette section traite de la fabrication des mémoires ferroélectrique à jonction tunnel utilisant une couche BaTiO₃ de 4 nm d'épaisseur ou une couche de Hf_{0.5}Zr_{0.5}O₂ de 2,8 nm d'épaisseur comme barrière tunnel compatible avec le procédé CMOS.

2.1 FABRICATION DES HETEROSTRUCTURES Nb:SrTiO₃/BaTiO₃

La déposition de titanate de baryum (BaTiO₃) a été réalisée sur un substrat de titanate de strontium dopé avec du niobium (Nb:SrTiO₃), par pulvérisation cathodique magnétron conventionnelle, à différentes températures (entre 500°C et 650°C). La cible pulvérisée était une céramique de BaTiO₃ polycristalline (2.54 cm de diamètre et 0.317 cm d'épaisseur). Les dépôts ont été réalisés dans une atmosphère d'oxygène et d'argon (pression partiel d'oxygène: 50%, pression totale: 20 mTorr). Les paramètres de synthèse sont listés dans le [Tableau 2](#).

Tableau 2. Paramètres de synthèse

Couche:	BaTiO ₃
Cible:	BaTiO ₃
Substrat:	Nb:SrTiO ₃
Densité de puissance:	~2 W/cm ²
Distance cible-substrat:	11 cm
Atmosphère:	Mélange Ar and O ₂
Pression de pulvérisation:	20 mTorr
Température de substrat:	Entres 500°C et 650°C
Temps de dépôt:	15 minutes
Durée de pré-pulvérisation:	7 minutes

Avant le dépôt, les substrats de Nb:SrTiO₃ ont été gravés dans l'eau en utilisant la méthode hydrothermale, puis recuits dans une atmosphère d'oxygène pour assurer une terminaison unique de la surface ([Figure 1](#)). La caractérisation par microscopie à force atomique (AFM – *Atomic Force Microscopy*) montre une rugosité de surface moyenne autour de 0.15 nm rms. Comme on peut le voir dans l'insert de la [Figure 1](#), le profil de la surface est formé de marches de 0.4 nm de hauteur en moyenne. Cela suggère que la surface est constituée d'une seule terminaison, SrO ou TiO₂.

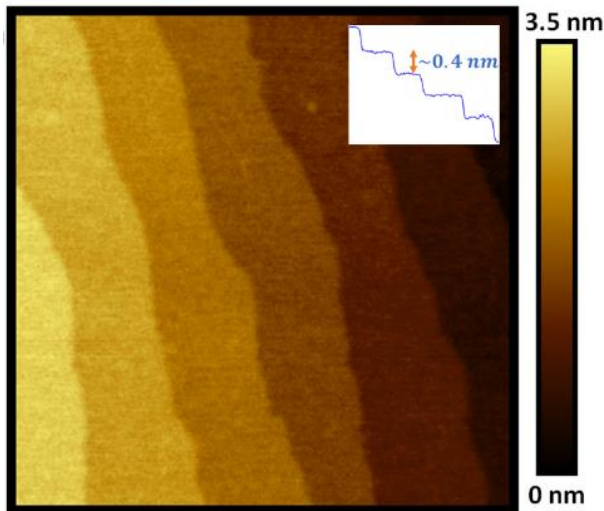


Figure 1. Topographie AFM d'un substrat de $\text{Nb}:\text{SrTiO}_3$ (100) gravé et recuit à 1000 °C. L'insert montre un profil de la surface avec des marches ayant une hauteur proche de 0.4 nm.

2.2 FABRICATION DES DISPOSITIFS MEMOIRES FERROELECTRIQUE A JONCTION TUNNEL NOMINALEMENT SYMETRIQUES

Une couche de $\text{Hf}_{0.5}\text{Zr}_{0.5}\text{O}_2$ a été déposée sur un substrat de silicium platinisé par pulvérisation cathodique magnétron. Le dépôt a été effectué sur un échantillon à une température 450°C et une pression de 5 mTorr (2 sccm d'oxygène et 2 sccm d'argon) avec une puissance de 20 W appliquée sur une cible d'un pouce. L'électrode supérieure en platine a été déposée par pulvérisation cathodique à travers un masque formé d'un réseau de trous de 300 µm de diamètre. Les paramètres de synthèse sont listés dans le [Tableau 3](#).

Tableau 3. Résumé des conditions de fabrication des mémoires FTJ nominalement symétriques.

Couche:	$\text{Hf}_{0.5}\text{Zr}_{0.5}\text{O}_2$	Pt
Cible:	$\text{Hf}_{0.5}\text{Zr}_{0.5}\text{O}_2$	Pt
Substrat:	Si/Pt	$\text{Hf}_{0.5}\text{Zr}_{0.5}\text{O}_2/\text{Pt/Si}$
Densité de puissance:	~2 W/cm ²	~5 W/cm ²
Distance cible-substrat:	11 cm	11 cm
Atmosphère:	Mélange Ar and O ₂	Ar
Pression de pulvérisation:	5 mTorr	5 mTorr
Température de substrat:	450°C	25°C
Temps de dépôt:	15 minutes	15 minutes
Durée de pré-pulvérisation:	45 minutes	3 minutes

2.3 FABRICATION DES DISPOSITIFS MÉMOIRES FERROÉLECTRIQUE À JONCTION TUNNEL ASYMÉTRIQUES

Les bicouches $\text{Hf}_{0.5}\text{Zr}_{0.5}\text{O}_2/\text{TiN}$ ont été synthétisées à l'aide de la pulvérisation cathodique magnétron (SPT310, Plasmionique Inc.) sur un substrat Si(100) dopé p ($\rho = 1 - 10 \Omega \cdot \text{cm}$). L'électrode inférieure en TiN a été déposée à 400°C dans une atmosphère d'azote et d'argon ($P_N = N_2/(Ar + N_2) = 70\%$) en utilisant une pression de pulvérisation de 10 mTorr. Ensuite, la croissance des couches $\text{Hf}_{0.5}\text{Zr}_{0.5}\text{O}_2$ a été effectuée à 425°C . Lors de cette étape, l'atmosphère de pulvérisation est formé d'un mélange d'argon et d'oxygène ($P_O = O_2/(Ar + O_2) = 50\%$) et la puissance RF sur la cible $\text{Hf}_{0.5}\text{Zr}_{0.5}\text{O}_2$ de 1 pouce de diamètre est fixée à 20 W. L'électrode supérieure en platine de 30 nm d'épaisseur est ensuite déposée sur la couche de $\text{Hf}_{0.5}\text{Zr}_{0.5}\text{O}_2$ en utilisant par pulvérisation cathodique à travers un masque formé d'un réseau de trous de 300 μm de diamètre. Les paramètres de synthèse sont listés dans le [Tableau 4](#).

Tableau 4. Résumé des conditions de fabrication des mémoires FTJ asymétriques

Couche :	TiN	$\text{Hf}_{0.5}\text{Zr}_{0.5}\text{O}_2$	Pt
Cible :	TiN	$\text{Hf}_{0.5}\text{Zr}_{0.5}\text{O}_2$	Pt
Substrat :	Si(100) type p	TiN/Si(100) type p	$\text{Hf}_{0.5}\text{Zr}_{0.5}\text{O}_2/\text{TiN/Si}$
Densité de puissance :	$\sim 4 \text{ W/cm}^2$	$\sim 4 \text{ W/cm}^2$	$\sim 5 \text{ W/cm}^2$
Distance cible-substrat :	11 cm	11 cm	11 cm
Atmosphère:	Mélange Ar et N_2	Mélange Ar et O_2	Ar
Pression de pulvérisation :	10 mTorr	5 mTorr	5 mTorr
Température de substrat :	400°C	450°C	25°C
Temps de dépôt :	120 minutes	45 minutes	3 minutes
Durée de pré pulvérisation :	15 minutes	15 minutes	15 minutes

La topographie de surface des couches $\text{Hf}_{0.5}\text{Zr}_{0.5}\text{O}_2$ après la croissance est visible sur la [Figure 2](#). Cette figure montre un tapis de grains couvrant uniformément l'électrode inférieure en TiN. La couche est suffisamment mince pour que les marches atomiques du substrat soient encore visibles. Les petits grains caractéristiques des couches de $\text{Hf}_{0.5}\text{Zr}_{0.5}\text{O}_2$ sont également visibles, et une rugosité de surface (rms – root mean square) d'environ 0.25 nm est obtenue sur une surface d'un micromètre carré, montrant la planéité de la surface des hétérostructures $\text{Hf}_{0.5}\text{Zr}_{0.5}\text{O}_2/\text{TiN}$.

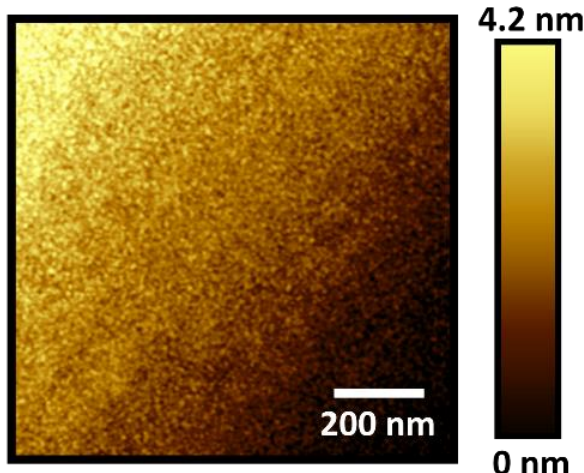


Figure 2. Topographie AFM ($1 \times 1 \mu\text{m}^2$) montrant les couches $\text{Hf}_{0.5}\text{Zr}_{0.5}\text{O}_2$ déposées sur une électrode de TiN

Comme l'effet TER est fortement dépendant de la l'épaisseur de la barrière ferroélectrique, il est important de mesurer l'épaisseur de nos couches. En utilisant la réflectivité spéculaire des rayons X (XRR – *X-Ray Reflectivity*), montré en [Figure 3](#). L'épaisseur a été estimée à environ 2.8 nm (6 mailles élémentaires de $\text{Hf}_{0.5}\text{Zr}_{0.5}\text{O}_2$) pour les couches utilisées dans la fabrication des mémoires FTJ et à environ 5.2 nm pour les couches utilisées dans l'étude structurale.

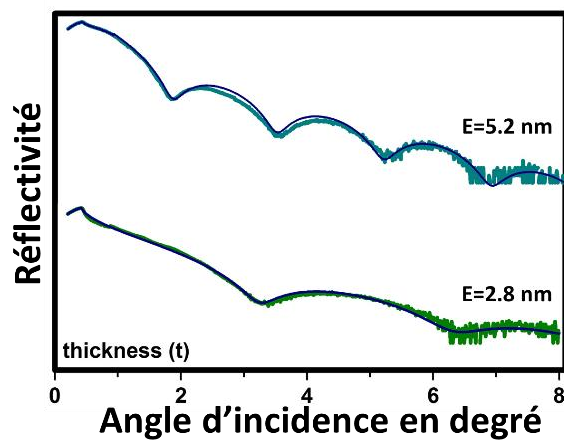


Figure 3. Spectre XRR mesuré sur des couches $\text{Hf}_{0.5}\text{Zr}_{0.5}\text{O}_2$

Afin de mieux comprendre les propriétés structurelles des couches ultraminces de $\text{Hf}_{0.5}\text{Zr}_{0.5}\text{O}_2/\text{TiN}$, l'identification des phases cristallines a été réalisée en utilisant la diffraction des rayons X en incidence rasant ([Figure 4](#)). Les pics de diffraction provenant des plans cristallins (111), (200) et (220) proviennent de la phase orthorhombique non-centrosymétrique, qui est

ferroélectriques. La phase ferroélectrique est obtenue dans les premières étapes de croissance. Elle commence par la nucléation de petits grains avec un important rapport surface sur volume, ce qui mène à la formation d'une phase tétragonale ($P4_2/nmc$). Cependant, les fortes contraintes d'elongation le long de l'axe c , induites par la coalescence des grains, permettent la formation de la phase ferroélectrique orthorhombique ($Pbc2_1$).²⁴ Le diffractogramme de rayons X présenté sur la Figure 4 (a) confirme la composition de la couche mince, sachant que le changement du rapport Hf/Zr provoque l'apparition d'autres pics de diffraction.²⁶

La cellule de la mémoire FTJ asymétrique, présentée en Figure 4 (b), à un diamètre de $300\mu\text{m}$, l'épaisseur de l'électrode inférieure en TiN est de 30 nm, celle de la couche mince ferroélectrique de $\text{Hf}_{0.5}\text{Zr}_{0.5}\text{O}_2$ est de 2.8 nm et l'électrode supérieure à une épaisseur de 30 nm.

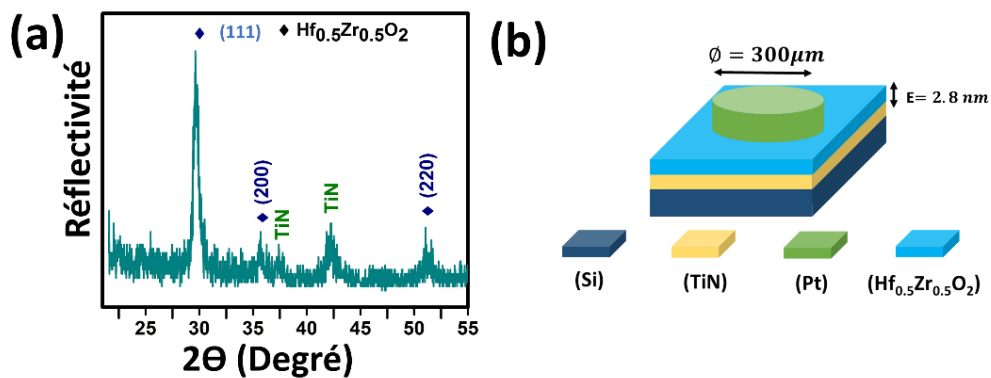


Figure 4. (a) Diffractogramme de rayons X en incidence rasante des couches minces de $\text{Hf}_{0.5}\text{Zr}_{0.5}\text{O}_2$ déposée sur l'électrode inférieure en TiN et (b) représentation schématique d'une cellule de mémoire FTJ asymétrique.

3. ANALYSE ET RESULTATS

3.1 MÉCANISME DE CROISSANCE DU BaTiO₃ SUR UN SUBSTRAT DE Nb:SrTiO₃

La cristallinité, l'épitaxie et la rugosité des couches minces dépend de leur nucléation de leur croissance, qui sont influencées par la température du substrat. Pour comprendre ce mécanisme, des couches minces de BaTiO₃ ont été déposées pendant 7 minutes sur des substrats de Nb:SrTiO₃ (100) à des températures entre 500°C et 650°C. Dans le cas des dépôts effectués à 600°C l'épaisseur de la couche est de 4.3 nm, ce qui représente 9 mailles unitaires du titanate de baryum, assez pour assurer une couverture complète de la surface du substrat. À une température de dépôt de 500°C, le substrat est entièrement recouvert d'une couche granuleuse laissant transparaître les marches issue de la gravure effectuée avant le dépôt ([Figure 5 \(a\)](#)).

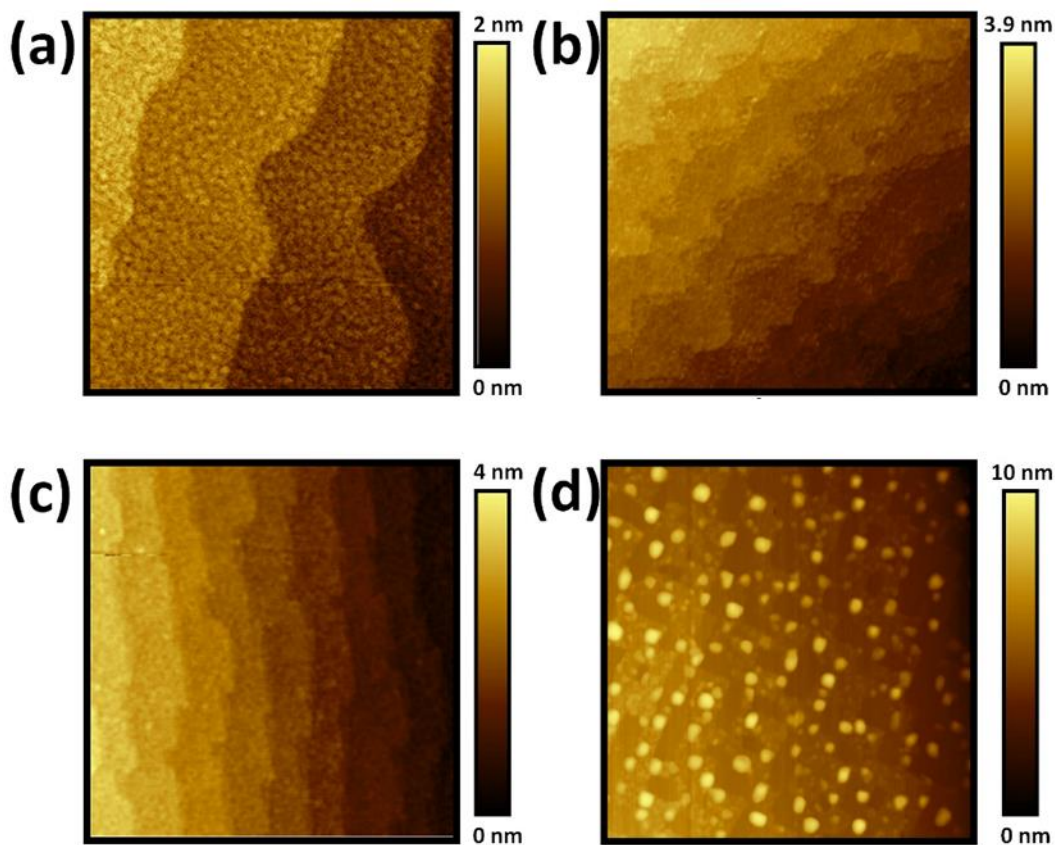


Figure 5. Topographies AFM de couches minces BaTiO₃ (surface : 1 x 1 μm²) déposées à différentes températures durant 7 minutes sur un substrat de Nb:SrTiO₃ (100); (a) 500°C, (b) 550°C, (c) 600°C, (d) 650°C.

La largeur moyenne des grains se situe autour de 6 nm, et leur hauteur est de quelques mailles unitaires (entre 0.8 nm et 1.2 nm). La hauteur des grains est sensée être un multiple entier de la hauteur de la maille unitaire du BaTiO₃ jusqu'à ce que le réseau cristallin commence à relaxer. Cette morphologie de surface ressemble à une croissance pseudo bidimensionnelle. La rugosité moyenne de la surface des couches est très proche de celle du substrat. À plus haute températures ($\geq 650^{\circ}\text{C}$), la topographie de la surface ([Figure 5](#) (d)) montre des grains irréguliers et une rugosité de la couche autour de 1 nm rms, qui est significativement supérieure à celle du substrat. Dans ce cas, la rugosité augmente avec l'épaisseur et les marches du substrat ne sont plus visibles, ce qui suggère une croissance mixte (Stranski-Krastanov). Cependant, dans la gamme de températures intermédiaires (550°C et 600°C , [Figure 5](#) (b) and (c)), la morphologie de la surface montre une couche complète de BaTiO₃ très fine, qui recouvre uniformément la surface du substrat, laissant transparaître les marches de ce dernier et ayant une faible rugosité. De telles caractéristiques sont plus prononcées dans le cas de la couche déposée à 600°C ([Figure 5](#) (c)) et nous estimons que cela est dû à un mode de croissance couche par couche.

3.2 CARACTÉRISATION DE LA FERROÉLECTRICITÉ DES COUCHES ULTRAMINCES DE BaTiO₃

L'existence de la ferroélectricité dans les couches ultra minces a été vérifiée expérimentalement pour des épaisseurs très faibles et dépend de la qualité cristalline des couches.^{101, 102} L'inversion de la polarisation de couches ultra minces de BaTiO₃ (4.3 nm) déposées sur un substrat de Nb:SrTiO₃ à 600°C a été mesurée par microscopie à force piézoélectrique (PFM – *Piezoresponse force microscopy*). La réponse piézoélectrique a été obtenue en appliquant, à une pointe AFM conductrice (Pt-Ir), une tension alternative additionnée à une tension continue (le substrat étant mis à la terre). Comme cela est visible sur la Figure 6, une couche de BaTiO₃ de 4 nm d'épaisseur, déposé à une température de 600°C, montre une courbe d'hystérésis typique des matériaux ferroélectriques.

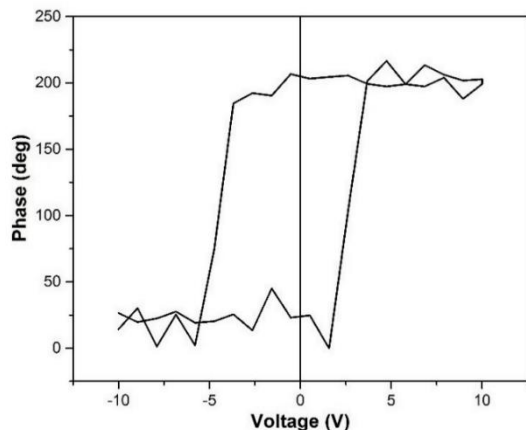


Figure 6. L'hystérésis de phase des couches ultra minces BaTiO₃ déposé sur un substrat de Nb:SrTiO₃ montre une rotation réversible de la polarisation de 180°.

3.3 CARACTÉRISATION DE LA FERROÉLECTRICITÉ DES COUCHES ULTRAMINCES DE $\text{Hf}_{0.5}\text{Zr}_{0.5}\text{O}_2$

Les propriétés ferroélectriques des couches de $\text{Hf}_{0.5}\text{Zr}_{0.5}\text{O}_2$ de 6 mailles élémentaires d'épaisseur, avec et sans électrode supérieure, ont été étudiées à température ambiante. Commençons avec les mesures obtenues par microscopie à force piézoélectrique (PFM – *Piezoresponse force microscopy*) des couches sans électrode supérieure (Figure 7).

La Figure 7 (a) montre clairement une hystérésis dans le signal de phase (variation de 180° du signal) et dans le signal d'amplitude, mesurés en fonction de la tension électrique appliquée et loin de la fréquence de résonance du cantilever. Les tensions à appliquer pour inverser la polarisation des domaines ferroélectrique est de +1.9 V pour obtenir un domaine ayant une polarisation orientée vers le bas (vers l'électrode inférieure) et de -1.9 V pour orienter la polarisation du domaine vers le haut. Ces résultats confirment le comportement ferroélectrique des couches ultramince de $\text{Hf}_{0.5}\text{Zr}_{0.5}\text{O}_2$.

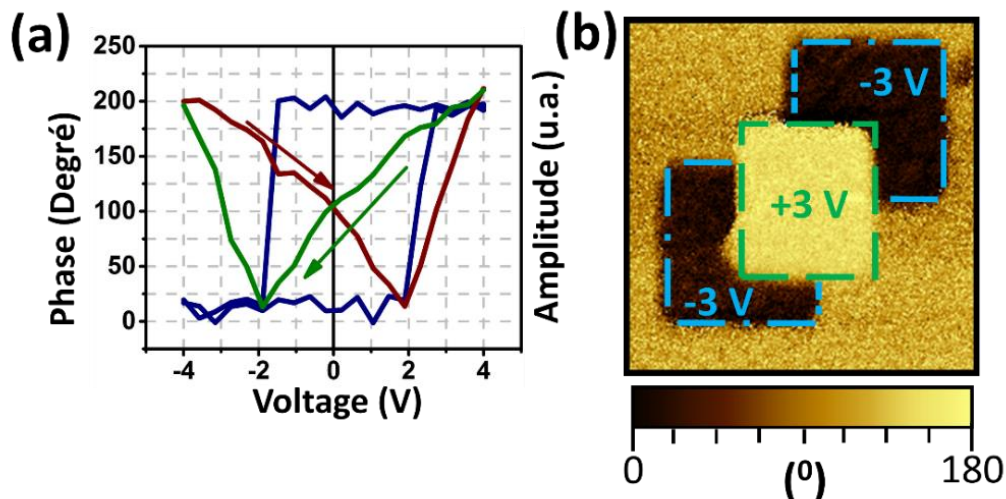


Figure 7. (a) Cycles d'hystérésis de la phase (courbe bleu) et de l'amplitude (courbes verte et rouge) de la réponse piézoélectrique obtenue en PFM et (b) image de contraste de phase ($3 \times 3 \mu\text{m}^2$) des zones écrites en PFM.

La Figure 7 (b) montre une image PFM de contrastes de phase contenant un motif de domaines ferroélectriques écrits intentionnellement. Ce motif est composé de trois zones carrés partiellement superposées, allant du coin en bas à gauche au coin en haut et à droite de l'image, ont été écrit respectivement en utilisant des tensions de -3 V, +3 V, et -3 V. Les domaines écrits

Résume en Français

avec une tension de -3 V ont une polarisation orientée vers le haut, tandis que celui écrit avec une tension de $+3$ V a une polarisation orientée vers le bas. La zone qui n'a pas été écrite reste dans un état vierge et a une polarisation orientée préférentiellement vers le bas. Cette polarisation spontanée est la conséquence des contraintes induites dans la couche de $\text{Hf}_{0.5}\text{Zr}_{0.5}\text{O}_2$ par le substrat, tandis que les zones écrites montrent que le matériau est capable d'endurer un cycle complet d'inversion de sa polarisation. Les zones écrites sont stables pendant plus de 60 heures, ce qui suggère que la polarisation de la couche de $\text{Hf}_{0.5}\text{Zr}_{0.5}\text{O}_2$ est stable et robuste. Cette analyse PFM est en accord avec les résultats obtenus par XRD, ce qui confirme la présence de la phase ferroélectrique orthorhombique.

3.4 PROPRIETES ELECTRONIQUES DES DISPOSITIFS MEMOIRES FTJ ASYMETRIQUES ET NOMINALEMENT SYMETRIQUES

Les propriétés optiques comme la largeur de la bande interdite optique (E_g) peut être estimée à l'aide des mesures de spectroscopie UV-visible en transmission, tandis que les propriétés du transport de charge au niveau de l'interface ferroélectrique/métal peuvent être étudiées en déterminant le décalage en énergie de la bande de valence ainsi que la hauteur des barrières de potentiel. Ainsi, une connaissance précise de ces paramètres optiques et électroniques est essentielle pour identifier une couche ferroélectrique appropriée pour les dispositifs mémoire FTJ.

Les hauteurs des barrières de potentiel au niveau des interfaces asymétriques TiN/Hf_{0.5}Zr_{0.5}O₂ (φ_1) et Hf_{0.5}Zr_{0.5}O₂/Pt (φ_2) ont été calculés respectivement à 1.86 ± 0.07 eV et 2.36 ± 0.07 eV. Le diagramme reconstruit des bandes d'énergies de l'hétérostructure TiN/Hf_{0.5}Zr_{0.5}O₂/Pt avec une polarisation spontanée vers le bas est visible sur la Figure 8 (a). Dans le cas des interfaces nominalement symétriques, la hauteur des deux barrières de potentiel est identique et égale à 2.36 ± 0.07 eV comme indiqué par la Figure 8 (b).

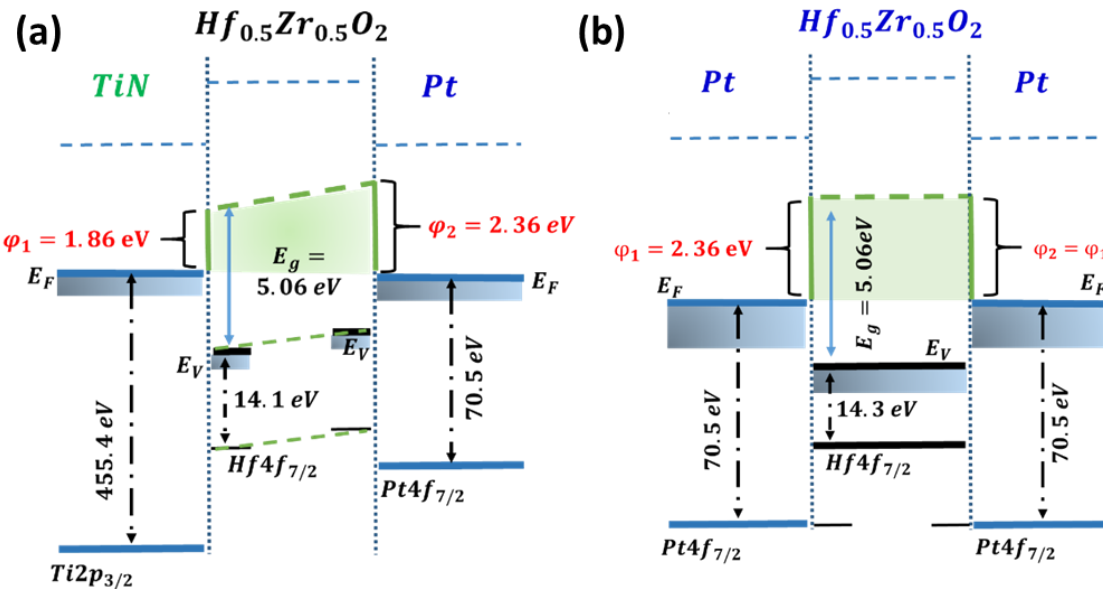


Figure 8. Représentation schématique du digramme de bandes électroniques (a) de l'hétérostructure TiN/Hf_{0.5}Zr_{0.5}O₂/Pt et (b) de l'hétérostructure Pt/Hf_{0.5}Zr_{0.5}O₂/Pt.

3.5 ÉLECTRORESISTANCE A EFFET TUNNEL DANS LES MEMOIRES FTJ NOMINALEMENT SYMETRIQUES.

Bien qu'il soit communément accepté que pour obtenir un effet TER conséquent il est obligatoire d'avoir des électrodes asymétriques,¹⁶ des études théoriques⁴² et expérimentales⁴¹ récentes ont montré qu'il est possible d'obtenir un grand effet TER avec des électrodes nominalement symétriques. En ajoutant à cela que d'autres travaux⁴² révèlent certains inconvénients des FTJ asymétriques, notamment concernant le temps de rétention de l'information, l'inversion de la polarisation. Nous avons donc centré ce travail sur la réalisation d'une mémoire FTJ consistant en une couche de $\text{Hf}_{0.5}\text{Zr}_{0.5}\text{O}_2$ de 2.8 nm d'épaisseur placée entre deux électrodes de platine (comme visible sur l'encart de la Figure 9 (b)).¹⁰⁵

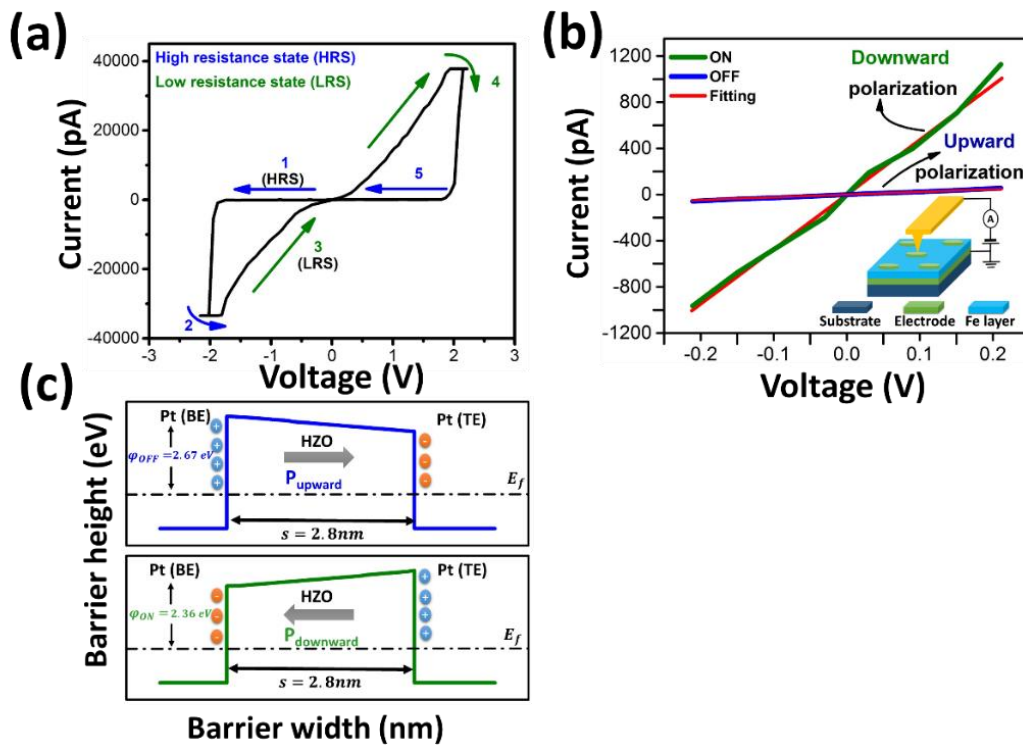


Figure 9. (a) Une courbe I - V typique d'une FTJ nominalement symétrique, (b) agrandissement dans la région des faibles tensions montrant les deux états de polarisation de la couche de $\text{Hf}_{0.5}\text{Zr}_{0.5}\text{O}_2$. Les lignes rouges sont le résultat des régressions linéaires et l'encart montre la configuration des mesures de C-AFM. (c) Schémas de la barrière de potentiel pour les deux orientations de la polarisation ($V \neq 0$).

La FTJ nominalement symétrique obtenue a été caractérisée en utilisant l'hystérésis électrique de ses courbes I - V . Un profil de tension triangulaire a été appliqué à l'électrode supérieure en utilisant une pointe AFM conductrice tandis que l'électrode inférieure a été mise à

la terre (potentiel nul). Un courant maximal de 100 nA a été fixé pendant les mesures pour éviter les claquages électriques de la FTJ. Une courbe I-V typiques est visible sur la Figure 9 (a). Elle montre une hystérésis caractérisée par deux états de résistance : un état initial ayant une résistance élevée (état « OFF ») et un état ayant une résistance faible (état « ON »). L'existence de deux états de résistance clairement distincts suggère la présence de l'effet TER.¹⁰⁵

Pour confirmer que l'hystérèse électrique observée en C-AFM est bien due à l'effet TER, et non à un autre effet de changement de résistance, nous avons corrélés les propriétés électroniques des interfaces et les propriétés de transport électrique de la FTJ nominalement symétrique en utilisant un modèle de courant de tunnel direct à travers une barrière rectangulaire. Ce modèle, appelé le modèle de Simmons¹⁰⁵ s'appuie sur la distribution de Fermi-Dirac et l'approximation BKW en considérant une faible tension (V) et une barrière de largeur s . La densité de courant tunnel (J) à travers la barrière est donné par

$$J = \left[\frac{3(2m\varphi)^{\frac{1}{2}}}{2s} \right] \left(\frac{e}{h} \right)^2 V \times \exp \left[\frac{-(4\pi s)}{h} (2m\varphi)^{\frac{1}{2}} \right] \quad (1)$$

Où m est la masse effective des électrons, φ est la hauteur de la barrière de potentiel, h est la constante de Planck et e est la charge d'un électron. La courbe I - V expérimentale de l'état « ON » a été ajustée en utilisant l'épaisseur de la couche de $\text{Hf}_{0.5}\text{Zr}_{0.5}\text{O}_2$ comme la largeur de la barrière ($s = 2.8$ nm) et la valeur de la barrière de potentiel obtenues par XPS ($\varphi = 2.36$ eV). La valeur du courant obtenue a ensuite été ajustée avec un facteur d'échelle (considéré identique pour les deux états), en accord avec la méthode décrite dans la littérature.^{43, 105} La hauteur de la barrière de potentiel de l'état « OFF » a ensuite été déterminé ($\varphi = 2.67$ eV) en utilisant les mêmes valeurs pour le facteur d'échelle et la largeur de la barrière. La variation de la hauteur de la barrière ($\Delta\varphi$) est d'environ 13%. L'effet TER dans nos FTJ a été quantifiée en utilisant le rapport TER [$(J_> - J_<)/J_<$]. Le rapport TER de ces FTJ nominalement symétriques est de 20, qui est dans la gamme typique (10>TER ratio>100).¹⁴

Dans la configuration Pt/ $\text{Hf}_{0.5}\text{Zr}_{0.5}\text{O}_2$ /Pt, la symétrie est incompatible avec le grand effet TER observé et les effets décrits par Bilc *et al.*⁴² pour une FTJ avec des électrodes nominalement symétriques ne peuvent pas être la source des valeurs observées. Nous attribuons ce comportement à l'asymétrie inhérente des interfaces attribuée, dans le cas présent, soit à la différence entre les

Résumé en Français

oxydes présents aux deux interfaces (ZrO_2 ou HfO_2), soit un état d’oxydation différent des électrodes de platine qui ont, chacune, un historique d’oxydation unique (l’électrode inférieure est recuite à 700°C tandis que l’électrode supérieure est déposée sous vide à température ambiante).

La résistance électrique des TFJ dépend de l’orientation de la polarisation.¹⁵ L’état de résistance faible correspond à une polarisation de la couche de $\text{Hf}_{0.5}\text{Zr}_{0.5}\text{O}_2$ orientée vers l’électrode inférieure. Cela crée une accumulation de charges négatives au niveau de l’interface avec l’électrode inférieure qui déforme la bande de conduction et réduit la hauteur de la barrière de potentiel (Figure 9 (c)). À l’inverse, quand la polarisation est orientée vers l’électrode supérieure, une accumulation de charges positive se produit au niveau de l’interface avec l’électrode inférieure, augmentant la hauteur de la barrière de potentiel, ce qui conduit à la création de l’état de resistance élevée du dispositif mémoire FTJ.^{14, 15, 18}

3.6 ÉLECTRORESISTANCE A EFFET TUNNEL DANS LES MEMOIRES FTJ ASYMETRIQUES.

L'effet TER dans notre système est étudié à travers des mesures électriques nanoscopiques. Une courbe I-V typique obtenue avec des dispositifs TiN/Hf_{0.5}Zr_{0.5}O₂/Pt est présentée sur la Figure 10 (a). Elle montre une hystérésis électrique caractérisée par un état initial ayant une résistance élevée (état « OFF », ligne verte), qui est transformé en un état ayant une résistance faible (état « ON », ligne bleue). L'hystérésis électrique ainsi que le changement important de la résistance électrique entre les deux états suggèrent la présence de l'électrorésistance à effet tunnel.^{43, 51, 105}

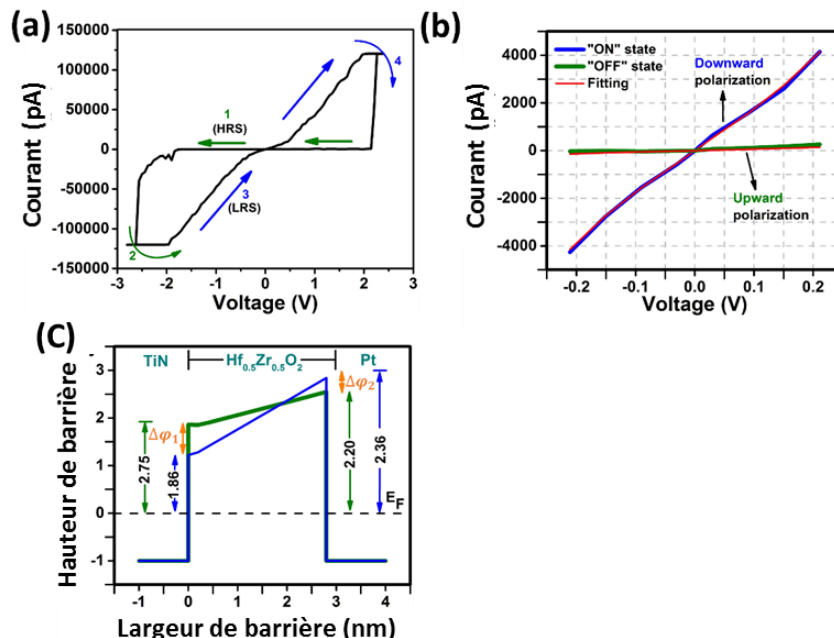


Figure 10. (a) Courbe I-V typique mesurée sur une l'hétérostructure TiN/Hf_{0.5}Zr_{0.5}O₂/Pt de 300 μm de diamètre, montrant les états de résistance faible et élevée, (b) agrandissement dans la région des faibles tensions montrant les deux états de polarisation de la couche de Hf_{0.5}Zr_{0.5}O₂, et (c) Barrière de potentiel électrostatique en fonction l'orientation de la polarisation.

Pour de confirmer que le changement de résistance observé dans la Figure 10 (a) est dû à l'effet TER plutôt qu'à un autre effet de changement de résistance, une méthode proposée par Zenkevich et al.¹⁰⁵ a été utilisée. Celle-ci corrèle les propriétés électroniques des interfaces et les propriétés de transport électrique de l'hétérostructure TiN/Hf_{0.5}Zr_{0.5}O₂/Pt en utilisant un modèle de courant de tunnel direct à travers une barrière trapézoïdale.¹¹¹ Ce modèle permet de calculer la

densité de courant de tunnel (J) en fonction de la tension appliquée (V) en utilisant les hauteurs de barrières de potentiel au niveau des deux interfaces (φ_1 and φ_2), l'épaisseur de la couche (d), la charge élémentaire (e), et la masse effective des électrons (m) tel que décrit par le modèle de Brinkman.^{43, 111}

$$J = - \left(\frac{4em}{9\pi^2\hbar^3} \right) \left(\frac{\exp(\alpha(V)[(\varphi_2 - \frac{eV}{2})^2 - (\varphi_1 + \frac{eV}{2})^2])}{\alpha^2(V)[(\varphi_2 - \frac{eV}{2})^2 - (\varphi_1 + \frac{eV}{2})^2]^2} \right) \times \sinh(\frac{3}{2}\alpha(V)[(\varphi_2 - \frac{eV}{2})^{\frac{1}{2}} - (\varphi_1 + \frac{eV}{2})^{\frac{1}{2}}] \frac{eV}{2}) \quad (2)$$

Avec $\propto(v) = [4d(2m)^{1/2}]/[3\hbar(\varphi_1 + eV - \varphi_2)]$ et \hbar est la constante de Planck réduite. La courbe I-V théorique de l'état "ON" (polarisation descendante) a été déterminée en utilisant les valeurs de la barrière de potentiel obtenues à l'aide de l'XPS ($\varphi_1 = 1.86$ eV and $\varphi_2 = 2.36$ eV), et en leurs ajoutant uniquement un facteur d'échelle qui est considéré approximativement le même pour les deux états, selon la méthode décrite dans la littérature.^{43, 105} Ensuite, en utilisant le même facteur d'échelle et l'équation 2, les courbes I-V ont été "fittées" afin d'obtenir les barrières de potentiel de chaque état. Comme le montre la Figure 10 (b), un bon accord est obtenu entre les courbes I-V et le modèle théorique donné par l'équation 2 des deux états "ON" et "OFF". Nous avons donc obtenu deux barrières de potentiel en utilisant ce modèle ($\varphi_1 = 2.75$ eV et $\varphi_2 = 2.20$ eV), qui produisent l'état "OFF" dans la courbe I-V (polarisation ascendante). Ainsi, le changement du renversement de la polarisation au niveau des interfaces TiN/Hf_{0.5}Zr_{0.5}O₂ et Hf_{0.5}Zr_{0.5}O₂/Pt sont respectivement $\Delta\varphi_1 = 0.89$ eV et $\Delta\varphi_2 = 0.16$ eV (Figure 10 (c)).

Caractérisation du dispositif mémoire FTJ asymétrique.

L'endurance des hétérostructures TiN/Hf_{0.5}Zr_{0.5}O₂/Pt a été évaluée en enregistrant 500 cycles I-V dans des conditions quasi statiques sur la même cellule-mémoire FTJ. Étant donné que l'AFM était requise pour cette opération, la vitesse d'acquisition a été limitée par les spécifications de l'AFM, faisant qu'une mesure de 500 cycles a pris une journée à être complétée. Pour chaque courbe I-V, les états de résistance « ON » et « OFF » ont été mesurés avec une tension de lecture de -0.2 V (Figure 11 (a)). Ces états restent stables sur les 500 cycles, indiquant une bonne endurance des mémoires FTJ.

Le temps de rétention de l'information de ces mémoires FTJ a été évalué, en mesurant la valeur de l'état de résistance « ON » d'une cellule mémoire dans le temps, en utilisant une tension

de lecture de -0.2 V. Comme le montre la [Figure 11](#) (b), l'état de résistance « ON » est toujours lisible après huit heures, démontrant que nos dispositifs mémoire FTJ présentent une rétention de longue durée.

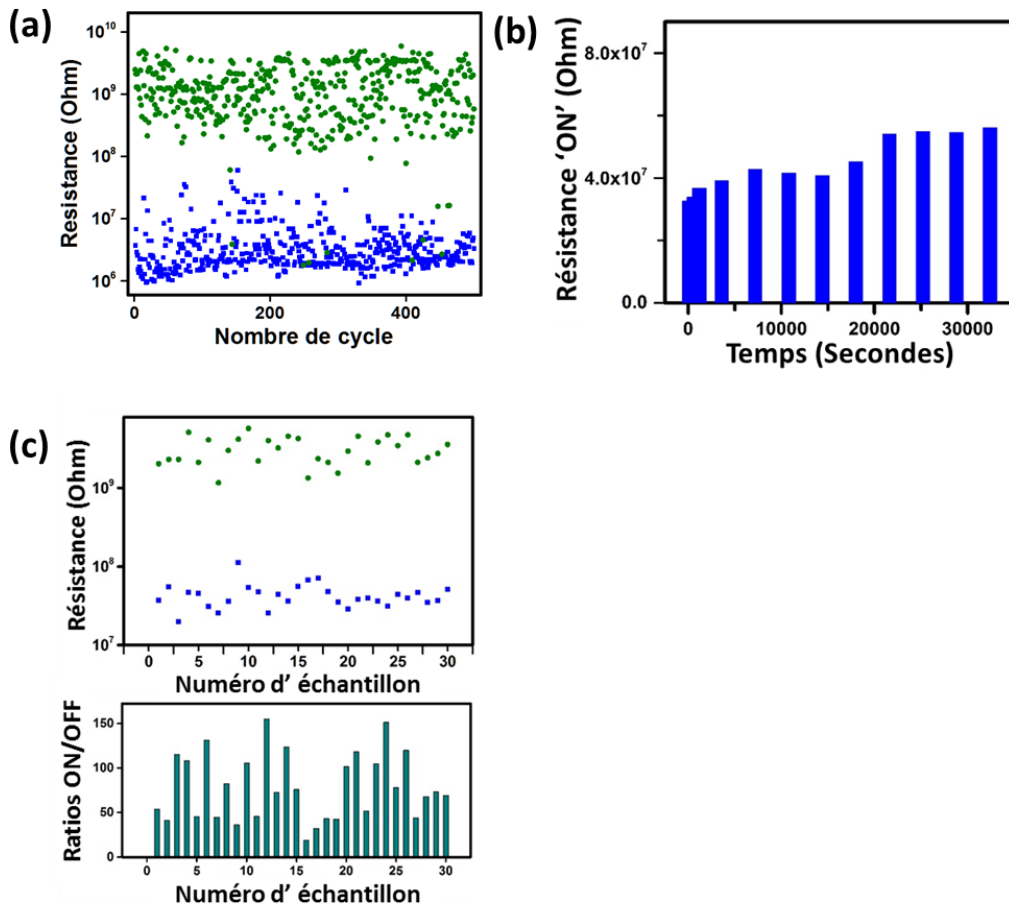


Figure 11. (a) Mesures de l'endurance de l'hétérostructure TiN/Hf_{0.5}Zr_{0.5}O₂/Pt (300 μm de diamètre), (b) Mesure du temps de rétention de l'information de l'état de résistance « ON » d'une cellule mémoire FTJ en utilisant une tension de lecture -0.2 V, et (c) États de résistance "ON" et "OFF" (panneau supérieur) et ratios ON/OFF (panneau inférieur) de 30 différentes cellules-mémoires FTJ.

La reproductibilité de l'effet TER dans nos mémoires FTJ a été vérifiée en mesurant des cycles I-V sur 30 dispositifs différents. Pour chaque cellule mémoire, les valeurs de la résistance des états « ON » et « OFF » ont été enregistrées en utilisant une tension de lecture de -0.2 V. Les 30 cellules mémoires présentent un ratio ON/OFF (ou ratio TER) de 15 ± 3 en moyenne ([Figure 11](#) (c)). Ce résultat atteste de la grande reproductibilité de l'effet TER dans nos dispositifs de mémoire TFJ.

4. CONCLUSION

Dans ce travail, le dépôt de couches minces cristallines de BaTiO₃ a été réalisé en une seule étape, à une température relativement basse de 600°C, par pulvérisation cathodique magnétron. Cependant, cette température du substrat est toujours trop élevée pour être compatible avec le procédé CMOS. Il a donc été nécessaire de rechercher de nouveau matériaux ferroélectriques pour obtenir cette compatibilité.

Les mémoires FTJ symétriques sont formées d'une couche Hf_{0.5}Zr_{0.5}O₂ d'épaisseur 2,8 nm placée entre deux électrodes en platine. Dans cette configuration, la symétrie des interfaces ne permet pas, en théorie, l'obtention de l'électrorésistance à effet tunnel. Cependant, nous avons observés un effet tunnel cohérent direct à travers le dispositif de mémoire FTJ symétrique, avec un ratio TER de 20 (comparable à ceux rapportés dans la littérature). Nous attribuons ce comportement à l'asymétrie inhérente des interfaces attribuée, dans le cas présent, soit à la différence entre les oxydes présents aux deux interfaces (ZrO₂ ou HfO₂), soit un état d'oxydation différent des électrodes de platine qui ont un historique d'oxydation différent.

Les mémoires FTJ asymétriques sont composées d'un matériau compatible avec la technologie CMOS (Hf_{0.5}Zr_{0.5}O₂) placé entre une électrode inférieure en nitre de titane et une électrode supérieure en platine, également compatibles avec la technologie CMOS. La combinaison de différentes techniques expérimentales (C-AFM, PFM, XPS, spectroscopie UV-Visible et XRD) et des modèles théoriques (modèle de courant de tunnel direct à travers une barrière trapézoïdale) a confirmé l'observation de l'électrorésistance à effet tunnel dans nos dispositifs mémoires asymétriques. De plus, la caractérisation de nos dispositifs a révélé d'excellentes propriétés telles que :

- (i) Un grand rapport TER (~15) mesuré avec une faible tension de lecture (-0.2 V) ;
 - (ii) Une bonne endurance (les deux états restent stables sur 500 cycles) ;
 - (iii) Une bonne rétention de l'information (de plus de neuf heures). Ce comportement non-volatile permet d'utiliser les dispositifs mémoire FTJ comme solution de remplacement aux mémoires flash largement utilisées dans les clés USB par exemple ;
 - (iv) Une excellente reproductibilité.
-